UNIVERSITY OF TURIN

Doctoral School in Life and Health Sciences
PhD Programme in Molecular Medicine
XXXI Cycle

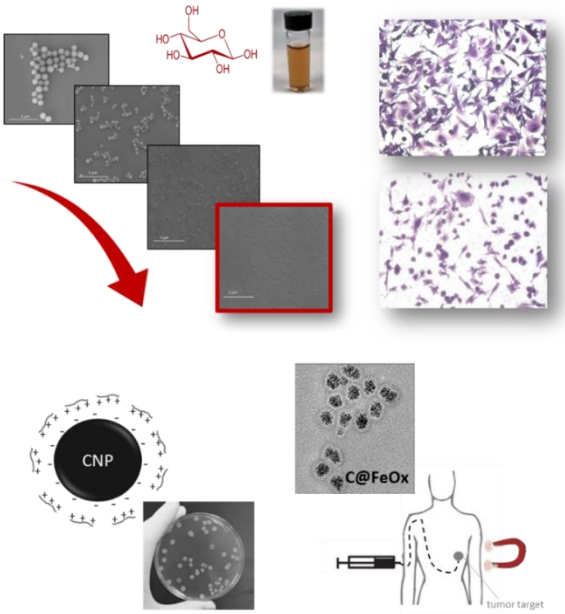

Evaluation of the safety and efficacy of carbon-based nanoparticles for biomedical applications

Ida Kokalari

UNIVERSITY OF TURIN

Phd School in life and Health Sciences
Molecular Medicine

XXXI Cycle
Academic Years: 2015-2019

Evaluation of the safety and efficacy of carbon-based nanoparticles for biomedical applications

Tutor: Prof. Ivana Fenoglio Candidate: Ida Kokalari

Coordinator: Prof. Francesco Novelli

to my family

Table of contents

Short summary

Nanomedicine, defined as the use of nanotechnology in medicine, is gaining a rapid increase in the last decades due to the novel solutions that offers in the diagnosis and treatment of diseases. It covers a wide range of research and application of nanoscale materials for biomedical use and includes drug delivery and targeting, imaging, and tissue regeneration. Carbon based nanomaterials are one of the multitude materials used in nanomedicine that have received enormous attention in particular due to their extraordinary intrinsic properties. However, their synthesis and application face several challenges particularly related to the extreme reaction conditions, complex instrumentations, high cost, environmental impact, low yield and batch-to-batch reproducibility that limit their mass production. In addition, despite promising preclinical research, toxicity related issues have been limited their translation into clinics.

The work presented in this thesis includes a series of studies involving carbon-based nanoparticles synthesized by a facile, reproducible and sustainable synthetic approach for biomedical applications, from material synthesis and extended physico-chemical characterization to the *in vitro* studies for the application in therapy. The biocompatibility and biodegradation using in vitro models was also investigated.

In chapter one, the optimization of the synthesis parameters is described in details together with the physico-chemical characterization of the CNP using numerous techniques. Moreover, the pro- and antioxidant properties were reported. We found that CNP are clearly antioxidants in a study involving LPS-activated macrophages, where CNP were internalized and were able to inhibit the production of ROS and NO in dark conditions. These findings suggest a possible use of CNP in all those pathological situations when an improper macrophage activation is undesiderable, like chronic inflammatory diseases. Oppositely, following NIR irradiation, CNP efficiently generate heat and singlet oxygen, properties that were exploited in the promotion of cell death of alveolar tumor cells, as described in chapter two. Results reported in chapter two suggest

therefore that CNP may represent a promising photothermal/photodynamic agent for the NIR-photo-therapy of tumors.

Beside efficacy, the successful translation of nanomaterials in the market is closely related to the demonstration of their safety. Indeed, in the present thesis different aspects of the *in vitro* biocompatibility of CNP are addressed. CNP were tested for their biocompatibility toward epithelial cell lines and blood cells and components exhibiting an excellent safety profile when non-activated by NIR light. CNP appear also susceptible to degradation when incubated with the immune-component enzyme hMPO. This finding was confirmed following incubation ex vivo of CNP with primary human neutrophils and suggests that CNP should not be biopersistent *in vivo.*

Overall, the reported promising results represent a first step toward the possible clinical translation of these switchable sugar-derived nanoparticles.

Additional data reported in this thesis concern the application of CNP as nanocarrier.

After in deep characterization of the pristine CNP, they were employed as a carbonaceous carrier for the investigation of the effect of Fe and Cu ions components in the airborne particulate matter, as described in chapter four, evidencing the role of copper as determinant factor in the toxicity of PM.

In chapter five, CNP are used as drug carrier for the cationic antimicrobial peptide Bac8c^{2,5Leu}. As CNP exhibit a highly negatively charged surface, the loading of the peptide by electrostatic interaction leaded to the formulation of a highly stable novel nanosystem aiming at the treatment of S.aureus infection.

Finally, the synthesis and characterization of a hybrid carbon shell-iron oxide core (C@FeOx) is reported in chapter six. The nanohybrids were obtained by a highly reproducible one-pot synthesis, capable of scavenging hydroxyl radicals, characterized by low cytotoxicity and are easily degraded by extremely low concentrated NaClO. C@FeOx may represent a combination of interesting properties of both covering material and magnetic core thus increasing the number of applications in nanomedicine.

General Introduction

Nanotecnology represents an innovative field of the modern science and deals with materials in the size range of the nanoscale, i.e. nanomaterials. Since few decades, immense attention has been focused in exploring the potentials of nanomaterials in different fields, especially in the biomedical field where they could offer unique solution in the diagnosis and treatment of diseases. The European Technology Platform for Nanomedicine (ETPN) released a first Vision Paper in 2005, which represented a document defining the purpose of Nanomedicine in Europe and consisted of "the application of Nanotechnology to Health. It exploits the improved and often novel physical, chemical, and biological properties of materials at the nanometric scale. NanoMedicine has potential impact on the prevention, early and reliable diagnosis and treatment of diseases". [1] Nanomedicine includes three main different areas of research: treatment, diagnosis and regenerative medicine.

Nanoparticles can be classified using different parameters, for example chemical nature: organic and inorganic nanoparticles. Liposomes are organic biodegradable nanoparticles (NPs) and the most extensively explored class of nanomaterials. In addition, liposomal formulations have already entered the market [2]. Inorganic NPs are also largely studied since the combination of intrinsic physical properties (e.g. opacity to radiations, thermal and optical properties) with surface functionalization allows the design of theranostic tools [3].

Nanomaterials have been already employed as nanovectors in clinical trial for gene delivery and have been proved to be a promising candidate for improving the safety and efficacy of gene-based therapies [4]. For example, nanoparticles produced by the FDA-approved polymer, poly(lactic-co-glycolic acid), have been proposed as gene vectors for the treatment of pancreatic cancer and shown to protect DNA/RNA from degradation *in vivo*.[5] Liposomic-based nanoparticles can encapsulate potent molecular anti-infectives, which exhibit poor permeability throw cell membranes, enhancing their cellular uptake in order to improve the

efficacy in combacting intracellular pathogens and offering the possibility of oral administration. [6]

Besides drug loading, nanoparticles in nanomedicine could be used as therapeutics when exhibit interesting intrinsic properties. Photothermal properties of gold nanoparticles made possible the ablation of tumor as they are able to convert the electromagnetic energy into heat sufficient for tumor cell death [7]. Superparamegnatic iron oxide nanoparticles are able to generate heat when an alternative magnetic field is applied due to their magnetothermal properties [8]. Photodynamic properties of fullerene make possible the application in cancer treatment and in infection diseases, as it generates cytotoxic reactive oxygen species (ROS) when illuminated by light of the proper wavelength. [9]

Furthermore, nanosized materials have been attracted worldwide attentions also in the diagnosis of diseases. Early detection can be particularly important especially for patients affected by cancer. For example, SPIONs functionalized with specific targeting moieties are reported to be able to accumulate at the site of tumor after recognition of specific markers expressed at cell membranes of tumor cells and enhance MRI detection of the tumor. [10]

NMs are also being investigated as scaffolds for tissue engineering and in bone regeneration. Thanks to their structure, nanostructure scaffolds may promote cell adhesion or migration, act as a synthetic extracellular matrix and enable tissue ingrowth in three-dimensional manner. [11]

However, to accelerate the development of all the areas of nanomedicine, nanomaterials, which exhibit multifunctional properties thus performing multiple actions simultaneously, are highly demanded. Among the variety of different classes of nanomaterials, carbon based nanomaterials could offer the possibility of combining multiple function in a single nanostructure. The discovery of the first member of this class of materials was achieved more than 30 years ago, and since than CNMs have been used in a wide range of applications in nanomedicine research [12]. The main biological and biomedical applications of CNMs include their use as ultra-sensitive biosensors for glucose and DNA, nanocomposites for neural and orthopedic prosthetic devices and delivery systems [13]. CNMs have

good potential to be use in photodynamic therapy [14], [15], [16] and photodynamic therapy [17], [18] thanks to their NIR light absorption and photothermal and photodynamic effects. Moreover, they exhibit antioxidant properties depending upon their structure. [19]

On the other hand, despite numerous advances, there are challenges regarding the synthesis, uniformity and reproducibility in the growth of carbon materials. Moreover, beside the many potential benefits of CNMs in the biomedical field, a major challenge for the nanomedicine industries will be to ensure that the nanodevices and nanomaterials used are safe for the human body and the environment. Extensive research is required using *in vitro* and *in vivo* models to test their biocompatibility before translation into clinical trials. Investigation regarding the safety profile toward cell lines and primary human cells could be a starting point to elucidate the toxicological profile of nanomaterials. However, it is important to evidence that in a biological fluid NPs are immediately coated by several proteins and biomolecules, such as lipids and polysaccharides. This proteins adsorption on the surface of the nanoparticles gives rise to the formation of a dynamic nanoparticle-protein corona (NP-PC) [20], which critically defines the biological identity of the particle. Therefore, it can be assumed that the interaction of NP with cellular structures is indirect and occurs mainly via the NP-PC and not via the surface of the nanoparticles. Interaction of nanoparticles with proteins is the basis of nanoparticle bio-reactivity [21], since the biophysical properties that the nanoparticles acquire with the formation of the NP-PC are different from those that had nanoparticles naked. This influence cellular uptake, inflammation, biodistribution, drug delivery, degradation and clearance of the nanoparticles throughout the body, also leading to potential unwanted biological side effects. Thus, the characterization of the protein corona should be taken in consideration when *in vitro* studies are performed.

The development of inorganic NMs has been slowed because of their possible toxicity as a consequence of the accumulation in the tissues that may lead to severe side effects. Carbon based NMs are insoluble in most organic solvents and

aqueous buffers therefore potentially biopersistent. However, recent researches demonstrated that enzyme peroxidases can cause biodegradation of carbon nanomaterials. Allen and co-workers [22] were the first showing that carboxylated SWCNTs were degraded through horseradish peroxidase (HRP), which is a plant derived enzyme. Subsequently, the same group demonstrated the degradation of oxidized SWCNTs by myeloperoxidase (MPO). MPO is a heme peroxidase enzyme most abundantly expressed in neutrophil granulocytes during first phase of inflammation that produces the strong oxidant hypochlorous acid, involved in the degradation of CNMs. In the last decade, numerous studies have evidenced the role of the enzyme and efficacy in the biodegradability of carbon nanomaterial (CNM) such as carbon nanotubes (CNTs) [23], fullerene [24] and graphene [25], findings that could help to pave the way to CNMs application as innovative nanomedicine multifunctional agents.

References

[1] European Technology Platform on Nanomedicine, Nanotechnology for Health: Vision paper and basis for a strategic research agenda for nanomedicine, September 2005, EC Publication office.

[2] Debbage P, Targeted drugs and nanomedicine: present and future, Curr Pharm Des, 15 (2009), 153-172.

[3] Y. Liu, H. Miyoshi, M. Nakamura, Nanomedicine for drug delivery and imaging: a promising avenue for cancer therapy and diagnosis using targeted functional nanoparticles, Int J Cancer, 120 (2007), 2527-2537.

[4] J. Chen, Z. Guo, H. Tian, X.Chen, Production and clinical development of nanoparticles for gene delivery, 3 (2016), 16023.

[5] S. Arora, SK Swaminathan, A. Kirtane, SK Srivastava, A. Bhardwaj, S1 Singh, J Panyam, AP Singh, Synthesis, characterization, and evaluation of poly (D,L-lactide-co-glycolide)-based nanoformulation of miRNA-150: potential implications for pancreatic cancer therapy, Int J Nanomedicine 9 (2014), 2933-42.

[6] S. Menina, J. Eisenbeis, MAM Kamal, M Koch, M. Bischoff, S. Gordon, B. Loretz, CM Lehr CM, Bioinspired Liposomes for Oral Delivery of Colistin to Combat Intracellular Infections by Salmonella enterica, Adv Healthc Mater. 8 (2019), e1900564.

[7] R. Mendes, P. Pedrosa, J. C. Lima, A. R. Fernandes, P. V. Baptista, Photothermal enhancement of chemotherapy in breast cancer by visible irradiation of Gold Nanoparticles, Sci Rep. 7 (2017) 10872.

[8] Q. A. Pankhurst, J. Connolly, S. K. Jones, J. Dobson, Applications of magnetic nanoparticles in biomedicine, Journal of Physics D: Applied Physics, 36 (2003)

[9] P. Mroz, G. P. Tegos, H. Gali, T. Wharton, T. Sarnad, M. R. Hamblin, Photodynamic therapy with fullerenes, Photochem. Photobiol. Sci. 6 (2007) 1139-1149.

[10] Z. Bakhtiary, A. A. Saei, M. J. Hajipour, M. Raoufi, O. Vermesh, M. Mahmoudi, Targeted superparamagnetic iron oxide nanoparticles for early detection of cancer: Possibilities and challenges, Nanomedicine, 12 (2016), 287-307.

[11] I. O.Smith, X. H. Liu, L. A. Smith, P. X. Ma, Nanostructured polymer scaffolds for tissue engineering and regenerative medicine, Wiley Interdiscip Rev Nanomed Nanobiotechnol, 1 (2009), 226-236.

[12] R. E. Smalley, H. Kroto, J. Heath, C60: Buckminsterfullerene. Nature, 318 (1985), 162−163.

[13] A. Bianco, K. Kostarelos, M. Prato, Making carbon nanotubes biocompatible and biodegradable, Chem Commun (Camb), 2011, 10182-10188.

[14] J. Kim, E. I. Galanzha, E. V. Shashkov, H. Moon, V. P. Zharov, Golden carbon nanotubes as multimodal photoacoustic and photothermal high-contrast molecular agents, Nat. Nanotechnol, 4 (2013), 688–694.

[15] J. T. Robinson, R. Luong, H. Dai, High Performance In VIvo NEar-IR (>1 μm) Imaging and Photothermal Cancer Therapy with Carbon Nanotubes. Nano Res. 3 (2011) 779–793.

[16] F. Zhou, Z. Ou, B. Wu, D. E. Resasco, W. R. Chen, Cancer photothermal therapy in the near-infrared region by using single-walled carbon nanotubes. J. Biomed. Opt. 14 (2018),

[17] B. Tian, C. Wang, S. Zhang, L. Feng, Z. Liu, Photothermally Enhanced Photodynamic Therapy Delivered by Nano-Graphene Oxide. ACS Nano, 5 (2011), 7000–7009.

[18] Ji, S. et al. Carbon nanotubes in cancer diagnosis and therapy. BBA - Rev. Cancer, 1806 (2010), 29–35.

[19] I. Kokalari, R. Gassino, A.M. Giovannozzi, L Croin, E. Gazzano, E. Bergamaschi, A. M. Rossi, G. Perrone, C. Riganti , J. Ponti, I. Fenoglio, Free Radic Biol Med, 134 (2019) 165-176.

[20] M. Monopoli, C. Aberg, A. Salvati, K. Dawson, Biomolecular coronas provide the biological identity of nanosized materials, Nature nanotechnology, 7 (2012), 779-786.

[21] S. R. Saptarshi, A. Duschl, A. L. Lopata, Interaction of nanoparticles with proteins: relation to bio-reactivity of the nanoparticle. J. Nanobiotechnology, 11 (2013).

[22] B. L. Allen, D. Padmakar, D. Kichambare, P. Gou, I. I. Vlasova, A. A. Kapralov, N. Konduru, V. E. Kagan, A. Star, Biodegradation of Single-Walled Carbon Nanotubes through Enzymatic Catalysis, Nano Letters, 8 (2008), 3899-3903.

[23] V. E. Kagan, N. V. Konduru, W. Feng, B. L. Allen, J. Conroy, Y. Volkov, I. I. Vlasova, N. A. Belikova, N. Yanamala, A. Kapralov, Y. Y. Tyurina, J. Shi, E. R. Kisin, A. R. Murray, J. Franks, D. Stolz, P. Gou, J. Klein-Seetharaman, B. Fadeel, A. Star, A. A. Shvedova, Carbon nanotubes degraded by neutrophil myeloperoxidase induce less pulmonary inflammation, Nat Nano 5 (2010) 354–359.

[24] E. V Litasova, V.V. Iljin, A. V. Sokolov, V. B. Vasilyev, M. A. Dumpis, L. B. Piotrovskiy, The biodegradation of fullerene C60 by myeloperoxidase, Dokl Biochem Biophys. 471 (2016), 417-420.

[25] S. P. Mukherjee, A. R. Gliga, B. Lazzaretto, B. Brandner, M. Fielden, C. Vogt, L. Newman, A. F. Rodrigues, W. Shao, P. M. Fournier, M. S. Toprak, A. Star, K. Kostarelos, K. Bhattacharyaa, B. Fadeel, Graphene oxide is degraded by

neutrophils and the degradation products are non-genotoxic, Nanoscale 10 (2018) 1180.

Aim of the thesis

Carbon nanomaterials are attractive candidate for a variety of biomedical applications since they could make possible the combination of multiple functions in a single NP. They possess antioxidant, photodynamic and photothermal properties, depending upon their structure. The possibility of surface functionalization provides interesting opportunities for drug delivery. However, the difficulties in large-scale production of particles with uniform properties and the high cost of production limits the current medical application of these nanostructures.

The overall aim of this study is to explore the unique and intrinsic properties of carbon-based nanoparticles synthetized by low cost, highly reproducible, one-step synthetic approaches and their safety and efficacy with the goal to contribute to the advancement of the knowledge of these types of nanomaterials in biomedical field.

In specific:

- To optimize the synthesis parameters in order to obtain tailored carbon-based nanoparticles
- To investigate the pro- and antioxidant properties in cell-free systems and their influence in the redox homeostasis of macrophages
- To evaluate the efficacy as photothermal and photodynamic agents in the treatment of lung cancer
- To study the biocompatibility toward different cell lines or primary human cells and the propensity to undergo biodegradation in acellular and cellular systems
- To explore the possibility to use CNP as nanovehicles for drug delivery or other applications

Chapter 1

Pro- and anti-oxidant properties of near-infrared (NIR) light responsive carbon nanoparticles

This Chapter has been published in

I. Kokalari, R. Gassino, A.M. Giovannozzi, L Croin, E. Gazzano, E. Bergamaschi, A. M. Rossi, G. Perrone, C. Riganti , J. Ponti, I. Fenoglio, Free Radic Biol Med, 134 (2019) 165-176

In this chapter, we describe the synthesis of a library of a new class of monodispersed carbon nanoparticles derived from glucose by a green chemistry fabrication method, following by an in-deep characterization of the product presenting the lowest diameter. The cell-free tests included the investigation of the physico-chemical properties of the surface and bulk structure and the pro-/antioxidant characteristics. In addition, photoactivity of the samples was also evaluated following NIR irradiation. Finally, *in vitro* cellular tests were performed using murine macrophages in order to assess the biocompatibility and the effect on the redox homeostatis of the cells.

The experiments regarding the synthesis and physico-chemical characterization were performed at the Department of Chemistry, University of Turin. Raman and SEM data were obtain at the Istituto Nazionale di Ricerca Metrologica, in collaboration with Dr. Andrea Giovannozzi and Dr. Luca Croin. *In vitro* cellular tests were conducted at the Department of Oncology, University of Turin, in collaboration with Prof. Chiara Riganti and Dr. Elena Gazzano. TEM images of cells were performed by Dr. Jessica Ponti, at the Joint Research Centre, Ispra.

1.1 Introduction

Elemental carbon nanomaterials (ECNMs), a large family of different materials, are widely studied in medicine. Among them, the most interesting are those that contain π-π conjugated frameworks, in particular carbon nanotubes [1], graphene [2] or fullerene [3].

ECNMs are characterized by a rich chemistry that enables them as carriers for various therapeutic agents [4,5]. In addition, depending upon the bulk structure, some of these materials exhibit physical properties like fluorescence, photo-thermal (PT) and photodynamic (PD) capabilities that suggest a possible use as both therapeutic and diagnostic agents themselves. Photo-nanomedicine has gain significant attention as a branch of nanomedicine focused on the treatment of tumour [6] and other diseases such as infections [7]. It consists in employing nanoparticles (NPs) switchable by light in order to obtain a therapeutic effect. In fact, some NPs are able to strongly absorb light of a particular wavelength and convert it into sufficient heat to induce cell death, which is the principle of photo-thermal therapy (PTT). Nanomaterials including ECNMs, gold and iron oxides NPs are widely studied as PT agents [8]. Alternatively, other NPs generate highly cytotoxic Reactive Oxygen Species (ROS) through different mechanisms following light exposure. This therapeutic approach is referred as photodynamic therapy (PDT) [9]. The use of NPs as PD agents instead of light alone or molecules, typically porphyrins, increases efficiency and selectivity of the treatment if a selective uptake of the NPs in the target cells is achieved by passive or active targeting. In the last decade, numerous studies have explored the PT and PD properties of ECNMs [3] like fullerene, single wall carbon nanotubes, graphene oxide, with or without functionalization with light-sensitive molecules [10]. One advantage in using ECNMs in PT or PD therapies is that they are activated by near infrared (NIR) light. In fact, compared with UV or visible light, NIR radiations exhibit reduced autofluorescence [11], lower photo toxicity and deeper tissue penetration ability [8].

Several studies report that ECNMs are redox active species [12]. Both antioxidant and pro-oxidant properties have been described on the different materials [13,14]. These properties are highly relevant in cancer therapy. Cancer cells have level of ROS higher than normal cells. This has been related to tumour initiation, promotion and progression. At the same time, the increase of ROS concentration may activate pathways detrimental for tumour cells like apoptosis, necrosis and autophagy [15]. Therefore, several substances included ECNMs able to either suppress or promote ROS, have been proposed as anticancer agents. Redox properties are also relevant for the safety of nanomaterials. In fact, an unbalance of the ROS level in healthy cells may activate inflammatory reactions or, on the contrary, may induce immunosuppression. In the case of ECNM, a comprehensive view on the effect of the various materials on cancer and healthy cells is still lacking. At the same time, while a wide number of studies suggest that the optical, thermal and redox properties of ECNMs are modulated by size, shape, surface and internal structure [16,17], the achievement of quantitative relationships between intrinsic and functional properties is still a challenge. Saccharides-derived carbon nanoparticles are an emerging class of ECNMs. Like other carbonaceous particles (soot, carbon black, etc.), they are substantially composed by amorphous carbon. However, they exhibit graphitic patches embedded in the amorphous matrix.

They have potential applications in several fields like adsorbents for heavy metals [18] or composites for energy storage [19]. Some studies suggest a possible use also in medicine as nanoplatforms for theranostic applications [20–23]. However, no data are available so far on their redox properties.

In the present study, a reproducible and high yield synthesis of CNPs derived by glucose (CNPs) of nanometric size has been achieved. The NPs have been studied for their bulk and surface properties and for their redox properties with or without photo-activation with a NIR laser beam in cell free systems. Finally, the capability of CNPs to modulate the redox homeostasis of macrophages was evaluated.

1.2 Materials and methods

Carbon black (CB1) was obtained by oxidation in H_2SO_4/H_2O_2 solution of activated charcoal (Sigma-Aldrich, Germany). Carbon black (CB2) was a kind gift of Dr. Michela Alfé (Istituto di Ricerche sulla Combustione – CNR, Naples, Italy). Fullerene powder, hydroxylated, $C_{60}(OH)_n$, used as positive control in the generation of singlet oxygen, and 2,2,6,6-tetramethyl-4-piperidone monohydrate, 99% (TMP) were purchased from Alfa Aesar (Germany). Sodium polyacrylate, D(+)-glucose, thionine acetate salt, phosphate buffered saline powder, EDTA, glutathione reduced and 5,5′-dithiobis(2-nitrobenzoic acid) were obtained from Sigma-Aldrich (Germany). 5,5-dimethyl-1-pyrroline-N-oxide (DMPO) was obtained from Cayman chemicals (USA). Ultrapure water was obtained from a Milli Q Plus system (Millipore, Bedford, MA, USA) and was always used freshly prepared. All other chemicals and solvents used were at least of analytical grade. When not otherwise specified, other reagents were purchased from Sigma-Aldrich.

1.2.1 Synthesis of glucose derived nanoparticles

Preparation of carbon nanoparticles was achieved using the hydrothermal carbonisation method. Firstly, glucose in different amounts was dissolved in 50 ml of ultrapure water by magnetic stirring and sodium polyacrylate (15 mg) was then added in order to prevent the typical cross-linking of the nanoparticles during the synthesis. The solution was transferred in a Teflon-lined stainless-steel autoclave (100 ml, Büchi AG), and placed in a preheated oven at 190 °C for 3–8 h. The different synthetic conditions are summarized in Figure 1.1. After the synthesis, the nanoparticles suspension was concentrated, purified with ultrapure water by ultrafiltration using Vivaflow 50R cassettes (Sartorius, 30 kDa cutoff) and air dried at 70 °C for

at least 48 h. The yields of the synthesis were calculated based on the mass of glucose used.

1.2.2 Morphological analysis

Morphology studies of the CNPs samples, CB1 and CB2 were performed using scanning electron microscopy (SEM, QuantaTM 3D FEG DualBeamTM). In the case of carbon black samples, the samples were sputter coated by a thin layer of conductive metal (20 nm of AuPd) to prevent charging of the surface and to promote the emission of secondary electrons. The geometric diameter for CNPs samples was measured using the software ImageJ and expressed as mean of the diameter of up to 600 particles.

The optimized formulation was also analysed by high-resolution transmission electron microscopy (HRTEM). Micrographs were achieved with a 3010 Jeol instrument operating at 300 kV. Aqueous CNP suspension (0.05 mg/ml) was dropped on a copper grid covered with a lacey carbon film.

The mean hydrodynamic diameter and polydispersity index (PDI) of nanoparticles were obtained using a Zetasizer (Nano ZS Malvern Instruments) based on the dynamic light scattering (DLS) technique. The nanoparticles were suspended (1 mg/ml) in ultrapure water, sonicated (Bandelin Sonopuls HD 3100) and then diluted 1:5 in ultrapure water.

1.2.3 Thermogravimetric analysis

Thermogravimetric analysis (TGA) was carried out in order to analyse the thermal stability of the nanoparticles and the presence of adsorbed species. The samples (ca. 3 mg) were placed in an open platinum pan which was supported by an ultra-microbalance (sensitivity 0.1 μg) and heated at a temperature range 35–700 °C at scan rate of 15 °C/min under N_2 (flow rate 35 ml/min) in a Pyris 1 TGA (PerkinElmer, MA, USA).

1.2.4 Surface area determination

The specific surface area (SSA) of the powders was measured by adsorption of N2 at 77 K, applying the BET model for the analysis of results. For CNP the geometrical specific surface area, calculated by the mean diameter of the particles (TEM) and by considering a density equal to that reported for graphite (2 g/cm3) was used.

1.2.5 UV–VIS–NIR spectroscopy

UV-Vis-NIR spectra of aqueous suspensions of the CNP and carbon black samples (0.05 mg/ml) were recorded at 1 nm intervals from 200 to 2500 nm on a CARY-5000 Varian spectrophotometer.

1.2.6 Fluorescence spectroscopy

Fluorescence spectra were obtained by a Fluorolog TCSPC Horiba Jobin Yvon Fluorescence Spectrophotometer. Aqueous suspension of CNP (0.2 mg/ml) was placed in a quartz cuvette (100 QS Hellman). In order to determine the emission wavelength of maximum intensity, the sample was excited using different wavelengths ranging from 285 nm to 515 nm. The emission spectra were recorded from 200-700 nm range. Confocal images of CNP were obtained by an Olympus Fluoview 200 laser scanning confocal system (Olympus America Inc., Melville, NY, USA). A drop of non-sonicated aqueous suspension was placed on a microscope slide. The excitation wavelength range was set at 340-360 nm.

1.2.7 Raman spectroscopy

For good sample homogeneity, CNPs were prepared as reported [24]. Briefly, 5 mg of powder were suspended in 1 ml of acetone (spectroscopic

grade NVR ≤ 5%) and homogenized for 10 min in 80 W ultra-sonic bath at 15 °C temperature (Q700 Sonicator, QSonica). The solvent was allowed to evaporate up to 25% of the initial volume and the samples were homogenized again for 5 min in the same conditions. The suspensions were then transferred in a flat vial and completely dried in air (at least 2 h) before the characterization. Raman measurements were carried out using the Thermo Scientific DXR Raman confocal microscope system equipped with an excitation laser source at 532 nm, a full range resolution grating of 3 cm^{-1} with a spectral range from 50 to 3500 cm^{-1}, a 20x long working distance microscope objective, a 50 µm pinhole aperture and an automatic x, y motorized stage. Micro-Raman mapping was performed on each sample within an area of 400 μm^2 using a step size of 5 µm and collecting 25 spectra in total. Each spectrum of the map was registered with 1 s integration time and 70 scans. A low laser power of 1 mW was used to avoid thermal heating and any possible damage of the sample. The spectra of each the map were averaged and normalized to the band at about 1600 cm^{-1}. The curve fitting was performed with the combination of Gaussian–Lorentzian line shapes that gave the minimum fitting error. The structure and Raman spectra of carbonaceous materials can be interpreted in terms of highly disordered graphitic structures. However, these systems are radically different to any disordered carbon created from graphite and cannot be perfectly modelled by the Tuinstra-Koenig correlation [25], neither after the adjustments proposed by Ferrari and Robertson [26]. Therefore, the fitting models proposed by Sadezky et al., [27] and Li et al., [28] in the analysis of the Raman spectra from burned carbon and pyrolyzed coals, respectively, were preferred to deconvolute the Raman spectra of the CNPs here proposed.

1.2.8 ζ-potential

Electrophoretic Light Scattering (ELS) technique was used to determine the zeta-potential of nanoparticles (Zetasizer Nano-ZS, Malvern Instruments,

Worcestershire, UK) in the pH range from 2 to 10. An aqueous suspension of nanoparticles (0.8 mg/ml) obtained by probe sonication was diluted 1:3 with ultrapure water. The pH values of the resulting suspension were adjusted NaOH or HCl, 0.1 M or 0.01 M. The results are mean values of three experiments.

1.2.9 Quantification surface acidic groups density

A spectrochemical titration assay, previously reported with modifications [29,30], was used for the quantification of surface acidic groups. The assay is based in the thionine acetate (THA) adsorption on the negatively charged moieties, which is responsible for the decolouration of the THA solution. CNPs (2 mg) were suspended in ultrapure water (1.875 ml) by ultrasonication and then an aqueous solution of THA (0.625 ml, 779.2 μM) was added. After 30 min of incubation under magnetic stirring in dark, the suspension was subjected to centrifugation (11.000 rpm for 30 min). The resulting supernatant was collected, filtered and its absorbance at 604 nm (Uvikon, Kontron Instruments, Inc., Everett, MA), due to the presence of the non-absorbed THA, was measured and compared with a calibration curve. The number of surface acidic functionalities was calculated assuming that THA reacts with acidic groups in stoichiometric ratio 1:1. The results are mean values of three experiments.

1.2.10 Evaluation of the photodynamic and photo-thermal properties

The ability of the nanoparticles to generate singlet oxygen upon NIR irradiation was studied by EPR/spin trapping technique. Samples were prepared by mixing equal volumes of an aqueous suspension of CNP (4 mg/ml) and spin trap 2,2,6,6-tetramethyl-4-piperidone (TMP) solution (101 mM) in a quartz cuvette and then subjected to irradiation for 10 min at room temperature. A laser diode emitting a wavelength of 945 nm (1.3 W/cm^2)

has been used as a light source. The laser light was conveyed through an optical fibre toward a lens adjusted in order to tailor the light spot dimension [30]. The potency of the laser was adjusted to a value normally used in PDT studies [31]. EPR spectra were measured on the suspension (Miniscope MS100, Magnettech, Berlin, Germany). The negative control consisted of a TMP solution, while fullerenol $C_{60}(OH)_n$ was used as positive control for $^1O_2$ generation. In order to confirm the generation of singlet oxygen, the experiments were repeated after fluxing the suspension for 5 min with nitrogen (N_2) to remove dissolved oxygen and in the presence of 0.3 M NaN_3. During NIR exposure, it was also investigated the capability of the samples to convert the absorbed energy in heat by monitoring the temperature of the suspension by means of a glass optic fibre sensor, a Fibre Bragg Grating (FBG) [32], inscribed in a different fibre with respect to the delivery one. This was in real-time interrogated with a homemade system that provides the sample temperature every 0.5 s. This solution provides more accurate temperature estimation: since the fibre optic sensor does not absorb the laser light, the temperature is exactly the one of the solution.

1.2.11 Scavenging activity toward hydroxyl radicals

The scavenging activity of CNP towards hydroxyl radicals was evaluated using electronic paramagnetic resonance (EPR)/spin trapping technique. 0.6 ml of a suspension of nanoparticles (5 mg/ml in phosphate buffer 0.5 M, pH 7.4) was transferred in a cuvette and stirred in the dark. 0.5 ml of a solution 0.15 M of 5,5-dimethyl-1-pyrroline N-oxide (DMPO) in water and 0.2 ml of a solution 13 mM of $FeSO_4$ were added. The reaction was started by adding 0.25 ml of a solution 0.2 M of H_2O_2. EPR spectra were measured on the suspension (Miniscope MS100, Magnettech, Berlin, Germany). The reaction was repeated in the absence of nanoparticles (control).

1.2.12 Reactivity toward glutathione

The interaction of the samples with reduced glutathione was evaluated by a modified Ellman's assay [33]. The method is based on the reaction between 5 and 5′-dithiobis[2-nitrobenzoic acid] (DTNB, Ellman's Reagent) and GSH which lead to the formation of 412 nm chromophore, 5-thionitrobenzoic acid (TNB) and GS-TNB.

Samples were prepared mixing equal volumes of aqueous nanoparticles suspension (1 mg/ml) with a solution of reduced glutathione (GSH) (4 mM in EDTA 1 mM/PBS 0.1 M) and incubated for 2 h under shaking at 37 °C. The suspension was then subjected to centrifugation for 30 min at 11.000 rpm. The supernatant was collected and filtered. For the quantification of the residual GSH, 100 µl of DTNB (4.3 mM in PBS 0.1 M/EDTA 1 mM) were added to the same volume of supernatant and the mixture was incubated for 5 min in the dark. The resulting solution was then diluted, and the UV–Vis spectra were recorded in the range from 200 to 600 nm (Uvikon, Kontron Instruments, Inc., Everett, MA). The concentration of residual GSH was calculated from a calibration curve. UV–vis spectra of the supernatant without Ellman's reagent were also acquired.

1.2.13 Cells

RAW 264.7 murine macrophages were kindly supplied by Diana Boraschi (CNR). Cells were cultured in Petri dishes in DMEM (Invitrogen Life Technologies, Carlsbad, CA) supplemented with 10% foetal bovine serum and 1% penicillin-streptomycin, then incubated in the same culture medium for 24 h, in the absence or presence of CNPs before the assays. A pyrogenic amorphous nanometric silica (Aerosil OX 50, Degussa Frankfurt A.M., Germany) was used as positive control. The protein content of cell monolayers was assessed with the bicinchoninic acid assay.

1.2.14 Particles dispersion in cell medium

Nanoparticles stock suspension with a concentration of 1 mg/ml was sonicated for 30 min in a bath sonicator followed by vortexing in order to obtain a homogeneous dispersion. Aliquots of 1 ml were taken and sonicated with a probe sonicator (Bandelin Sonopuls HD 3100, Ti probe diameter 3 mm, power 400 W, frequency 20 kHz) for 2 min using the pulsation mode at 40% of power. The final suspension was then diluted in cell culture media at the desired concentrations. The stability of the suspensions was evaluated by Dynamic Light Scattering (DLS, Zetasizer Nano ZS, Malvern Instruments).

1.2.15 Measurement of lactate dehydrogenase leakage

The cytotoxic effect of the nanoparticles was measured as the leakage of lactate dehydrogenase (LDH) activity into the extracellular medium, using a Synergy HT microplate reader (Bio-Tek Instruments, Winooski, VT), as previously described [34]. Both intracellular and extracellular LDH were measured and then extracellular LDH activity (LDH out) was calculated as a percentage of the total (intracellular + extracellular) LDH activity (LDH tot) in the dish.

Purified LDH (from bovine muscle, purity > 99.5%) was used to rule out the interference of CNPs on the enzyme activity [35]. Briefly, cell culture medium in the absence (control) or presence of nanoparticles (10–320 µg/ml) was incubated with 0.3 U/ml of LDH at 37 °C. After 24 h, the medium was centrifuged, and enzyme activity was measured spectrophotometrically in the supernatants. Incubations up to 80 µg/ml of CNPs did not reveal any interference in agreement with what previously found on carbon nanotubes [35] (data not shown). A negligible effect was observed above the concentration of 160 µg/ml.

1.2.16 Uptake and Intracellular distribution

The cellular uptake and distribution of CNPs was qualitatively evaluated by TEM analysis. RAW 264.7 murine macrophages were incubated for 24 h with 40 µg/ml and for 48 h with 160 µg/ml of CNPs. At the end of exposure, cells were washed, detached and re-suspended in 2% Karnovsky solution. Before analysis, Karnovsky solution was removed and cells re-suspended in osmium tetroxide solution in 0.1 M cacodilate pH 7.3 for 1 h. After three washes in cacodilate, 0.05 M of 10 min each, cells were dehydrated in a series of ethanol solutions in MilliQ water (30%; 50%; 75%; 95% for 15 min each, and 100% for 30 min), incubated in absolute propylene oxide for 20 min and embedded in a solution of 1: 1 epoxy resin -propylene oxide for 90 min. This mixture was renewed with pure epoxy resin over night at room temperature and later polymerized at 60 °C for 48 h. Ultrathin sections (50–70 nm) were obtained using Leica UCT ultramicrotome (Leica, Italy) and stained for 25 min with uranyl acetate and lead citrate for 20 min, washed and dried. Ultrathin sections were collected on Formvar Carbon coated 200 mesh copper grids (Agar Scientific, USA) and imaged by JEOL JEM-2100 h-transmission electron microscope at 120 kV (JEOL, Italy).

1.2.17 Measurement of Reactive Oxygen Species

RAW 264.7 cells were incubated for 24 h in the absence or presence of CNPs, then cells were incubated for 30 min with 10 µM 2 ′ ,7 ′ -dichlorodihydrofluorescein diacetate (DCFH-DA), as previously described [36]. DCF fluorescence was determined using a Synergy HT microplate reader at an excitation wavelength of 504 nm and an emission wavelength of 529 nm. The fluorescence value was normalized to protein concentration and expressed as units of arbitrary fluorescence.

The experiments were repeated by adding 1 µg/ml of lipopolysaccharide (E. Coli 055:B5, Sigma-Aldrich) (LPS).

1.2.18 Measurement of nitrite

RAW 264.7 cells were cultured for 24 h in the absence or presence of CNPs. The amount of extracellular nitrite (the stable derivative of nitric oxide) was measured spectrophotometrically, by adding 0.15 ml of cell culture medium to 0.15 ml of Griess reagent in a 96-well plate. After 10 min of incubation at 37 °C in the dark, the absorbance was detected at 540 nm with a Synergy HT microplate reader. For each experiment, a blank was prepared in the absence of cells, and its absorbance was subtracted from that measured in the presence of cells. Nitrite concentration was expressed as nmol nitrite/mg cell proteins.

1.2.19 Measurement of intracellular glutathione

Intracellular reduced glutathione (GSH) was measured as previously described [34]. The kinetics of reaction was followed at 415 nm for 10 min using a Synergy HT microplate reader.

Each measurement was made in triplicate, and results were expressed as nmolGSH/ milligram cellular proteins.

1.2.20 Cytokine measurement

Tumour necrosis factor-α (TNF-α) and interleukin-10 (IL-10) were measured in the supernatants of RAW 264.7 cells using the Mouse TNFalpha DuoSet ELISA (R&D Suystems, Mineeapolis, MN) and the murine IL-10 ELISA kit (PeroTech Inc., Rocky Hill, NJ), as per manufacturer's instructions. The results were expressed as pg cytokine/mg cellular proteins.

The experiments were repeated by adding 1 µg/ml of LPS.

1.2.21 Statistical analysis

All data in the text and figures are provided as means ± SD. The results were analysed by a one-way analysis of variance (ANOVA) and Tukey's test. $p < 0.05$ was considered significant.

1.3 Results and discussion

1.3.1 Synthesis and characterization carbon nanoparticles (CNP)

Since the first study reporting the identification of carbon NPs as product of hydrothermal carbonisation of saccharides [37], different attempts have been made to exploit this process in order to develop CNPs with specific morphological characteristics. Spherical CNPs were previously obtained by glucose [38]. However, cross-linking among particles during the synthesis may occur [39]. To overcome this drawback, Gong et al. proposed the addition in the reaction mixture of the polymer sodium polyacrylate [40].

To establish the optimal synthesis conditions for the preparation of NPs with the desired size range, here we modified the original parameters of the protocol proposed by Gong et al. in order to prepare NPs having diameter lower than 100 nm. The effects of the explored synthetic parameters are summarized in Figure 1.1a.

A comparison between the mean hydrodynamic diameter (in number distribution) measured by dynamic light scattering and geometric diameter derived from SEM images is shown in Figure 1.1b. The data confirmed that all the particles obtained were in nanosize ranges with a mean diameter that varies from 100 to 700 nm depending on the synthetic parameters. The higher standard deviation in the mean geometric diameter of CNP1, in comparison with the DLS data, is related to the presence of a very small population of NP having a diameter around 100 nm that can be observed in the SEM images but not during the DLS measurement, as the latter overestimates the larger particles. The morphology of NPs was evaluated by scanning electron microscopy. Figure 1.1c shows typical SEM images of the different CNP. The NPs were all smooth and almost perfectly spherical in shape with a narrow size distribution. The yields of the synthesis after purification were 5, 22, 20% and 3% for CNP1, CNP2, CNP3 and CNP4, respectively, correspondent to 60–900 mg of product per

synthesis. The polydispersity index for all the samples was below 0.15 (data not shown), further confirming that in all cases narrowly dispersed NPs were obtained [41]. The sample having the lowest diameter (CNP4) was chosen for further characterization being the more promising candidate in therapy. In fact, different studies concerning spherical particles, confirm that a diameter of 50 nm seems to be the most favorable size in order to reach the highest cellular uptake of nanoparticles in tumour cells [42].

a)

sample	precursor (g) in 50 ml H_2O	surfactant (mg)	time (h)	temp (°C)
CNP1	8	15	8	190
CNP2	4	15	8	190
CNP3	2	15	8	190
CNP4	2	15	3	190

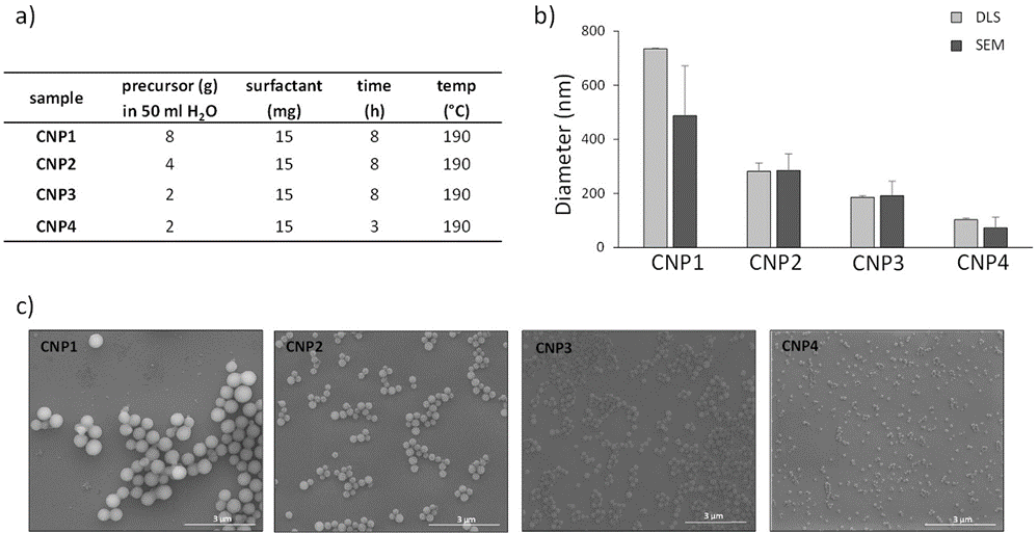

Figure 1.1. a) Summary of the parameters used in the synthesis of the CNPs; b) Comparison between hydrothermal diameter obtained by Dynamic light scattering (number distribution) and geometric diameter obtained by SEM imaging of the CNPs suspended in water. c) SEM images of different preparations of CNPs.

The synthesis was repeated several times to investigate the reproducibility. The hydrodynamic diameters and polydispersion indexes of the different batches are reported in Figure 1.2.

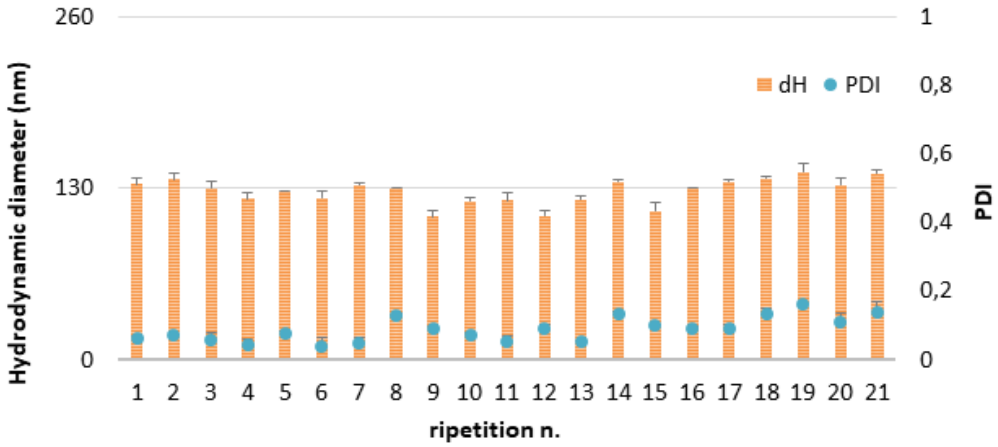

Figure 1.2. Hydrodynamic diameter (from intensity distribution) and polydispersion index of 21 different batches of CNP4.

Figure 1.3. Diluted CNP4 suspension (0.05 mg/ml).

A representative image of the purified suspension of CNP4 is reported in Figure 1.3. The particles appeared composed by carbon (83.51%) and oxygen (16.49%), as revealed by EDS analysis (data not shown). The bulk structure of CNP4 was investigated by high resolution TEM. A typical TEM image of CNP4 is shown in Figure 1.4. The nanoparticles appear spherical in shape confirming what observed by SEM, and with a low contrast, in agreement with a structure mainly composed by amorphous carbon. However, by high magnification, crystalline domains embedded in the amorphous structure of the nanoparticles were observed (inset). In the

crystalline domains, the measured interlayer spacing was equal to 0.344 nm, a value that suggests the presence of turbostratic graphite.

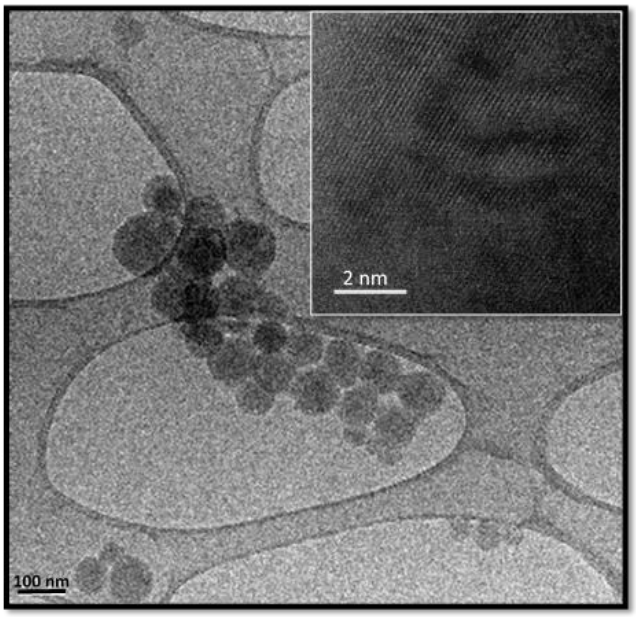

Figure 1.4. HRTEM image from sample CNP4. The top right inset shows crystalline configuration.

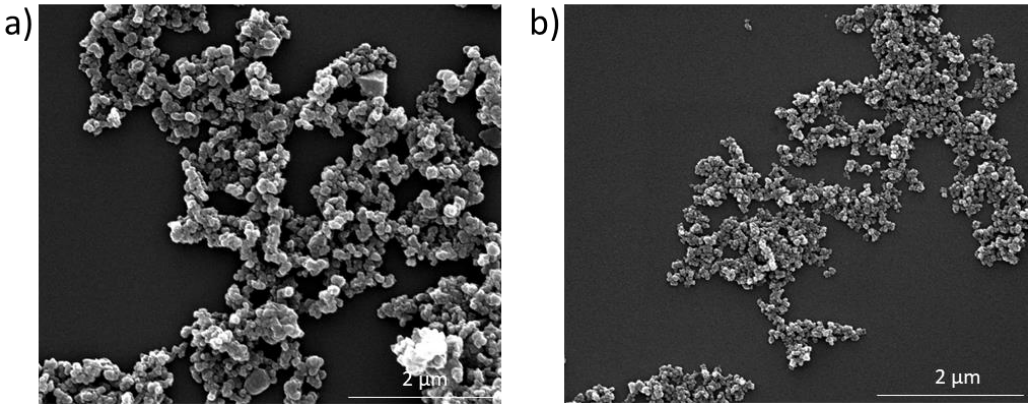

Figure 1.5. Representative SEM micrographs of carbon black samples: (a) CB1 and (b) CB2.

The bulk structure of CNP4 was further investigated by Raman spectroscopy, a technique largely used [43–45] to provide information on the degree of ordering and crystallinity of carbonaceous materials [26–28]. In a high order single crystal graphite, Raman spectrum shows one band at around 1585 cm^{-1}, i.e. the G (‘‘Graphite’’) band, only, corresponding to an

ideal graphitic lattice vibration mode with E2g symmetry. In case of polycrystalline graphite and disordered graphite systems, Raman spectrum exhibits additional first-order bands (D or ‘‘Defect’’ bands), whose most intensive is the D1 band, which appears at around 1360 cm^{-1} and corresponds to a graphitic lattice vibration mode with A1g symmetry. The D peak is due to the breathing modes of sp^2 atoms in rings and it grows in intensity relative to the G band with increasing degree of disorder in the graphitic structure. Few other second order modulations may be present in the range from 2300 cm^{-1} to 3300 cm^{-1} [46,47].

The analysis was performed in comparison with two samples of carbon black (CB1, CB2) having different degree of crystallinity, both composed by nanoaggregates, as shown in the SEM images in Figure 1.5, and with a specific surface area equal to 58 m^2/g, for CB1, and 196 m^2/g, for CB2. The Raman spectra of CB1, CB2 and CNP4 and the deconvolution patterns are shown in Figure 1.6a. A full list of the picks of each spectrum is reported in table 1.1.

The D and G bands dominate the first-order spectrum of CB1. The peak at ~1585 cm^{-1} comprises not only the G but also the D2 band known from disordered graphitic lattices.

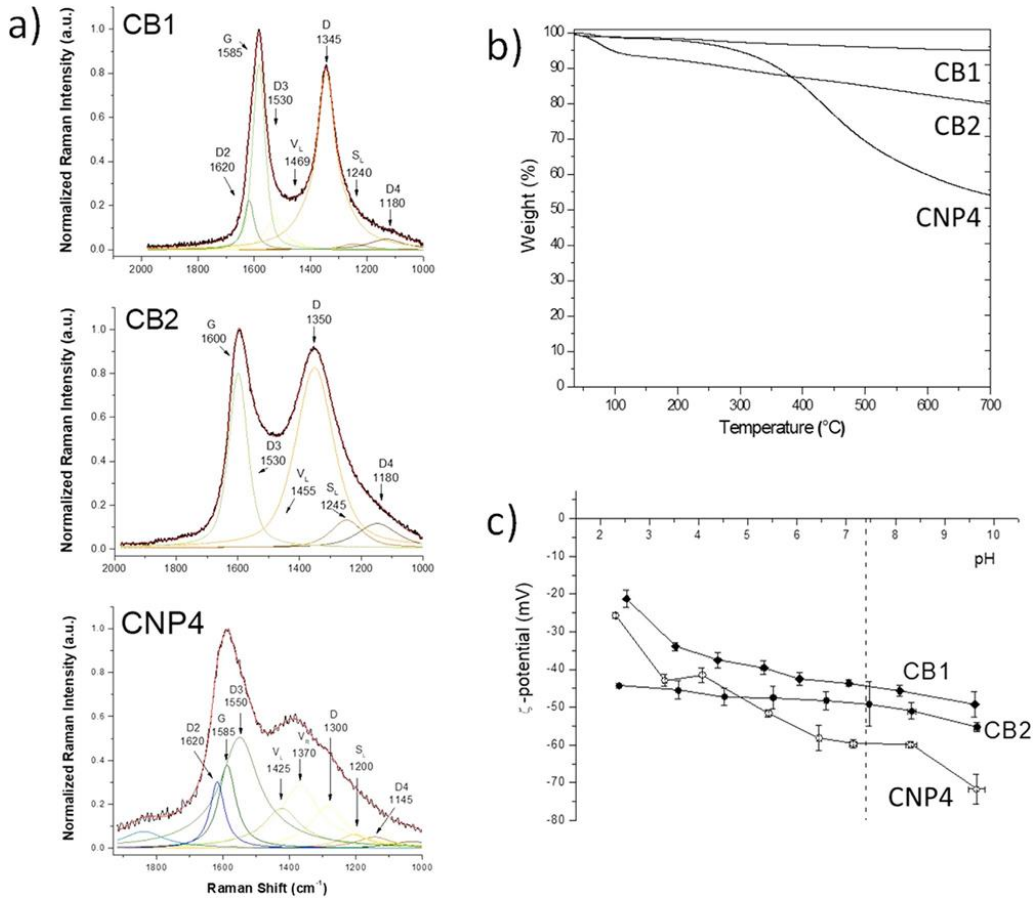

Figure 1.6. a) Raman spectra and deconvolution patterns of CNP4 and carbon black samples. b) TGA thermograms. % of weight loss recorded under N_2 (TGA heating ramp 15 °C/min, N_2 flow rate 35 ml/min); c) Zeta potential versus pH curves for CNP4 and reference samples suspended in water. The curves are relative to CNP4 (open circles), CB1 (squares) and CB2 (circles).

Table 1.1. Raman shift and vibration modes.

	Raman shift (cm^{-1})	**Vibration modes**
CB1	~1620	D2 (disordered graphitic lattice)
	~1585	G (graphitic lattice vibration mode with E_{2g} symmetry, alkene C=C)
	~1530	
	~1460	D3 (aromatics with 3−5 rings, amorphous)
		V_L (methylene or methyl, semicircle breathing of aromatic rings, amorphous)
	~1345	
	~1240	D (Disordered graphitic lattice with A_{1g} symmetry)
	~1180	S_L (aryl−alkyl ether, para-aromatics)
		D4 (C–C and C=C stretching vibrations of polyene-like structures)
CB1 2D Region	~3220	(2*D2) overtone
	~2920	(G + D) combination
	~2690	(2*D) overtone
	~2460	(2*D4) overtone
CB2	~1600	G (graphitic lattice vibration mode with E_{2g} symmetry, alkene C=C)
	~1530	
	~1455	D3 (aromatics with 3−5 rings, amorphous)
		V_L (methylene or methyl, semicircle breathing of aromatic rings, amorphous)
	~1350	
	~1245	D (Disordered graphitic lattice with A_{1g} symmetry)
	~1180	S_L (aryl−alkyl ether, para-aromatics)
		D4 (C–C and C=C stretching vibrations of polyene-like structures)
CNP4	~1840	oxygen-related functional group
	~1620	D2 (disordered graphitic lattice)
	~1585	G (graphitic lattice vibration mode with E_{2g} symmetry, alkene C=C)
	~1550	
	~1425	D3 (aromatics with 3−5 rings, amorphous)
		V_L (methylene or methyl, semicircle breathing of aromatic rings, amorphous)
	~1370	
	~1300	V_R (methyl, semicircle breathing of aromatic rings, amorphous)
	~1200	
	~1145	D (Disordered graphitic lattice with A_{1g} symmetry)
	~1030	S_L (aryl−alkyl ether, para-aromatics)
		D4 (C–C and C=C stretching vibrations of polyene-like structures)
		C−H on aromatic rings, benzene (ortho-disubstituted) ring or oxygen-related functional groups
CNP4 700°C	~1600	G (graphitic lattice vibration mode with E_{2g} symmetry, alkene C=C)
	~1530	
	~1450	D3 (aromatics with 3−5 rings, amorphous)
		V_L (methylene or methyl, semicircle breathing of aromatic rings, amorphous)
	~1340	
	~1260	D (Disordered graphitic lattice with A_{1g} symmetry)
	~1180	S_L (aryl−alkyl ether, para-aromatics)
		D4 (C–C and C=C stretching vibrations of polyene-like structures)

The valley between the two peak maxima can be attributed to another band at ~1530 cm^{-1}, which has been designated as D3 or A band in several studies [27,48,49], that originates from the amorphous carbon fraction of soot and aromatics with 3–5 rings. Two peaks due to overtones were also observed in the 2000–3000 cm^{-1} region further supporting the high degree of graphitization of this sample Figure 1.7.

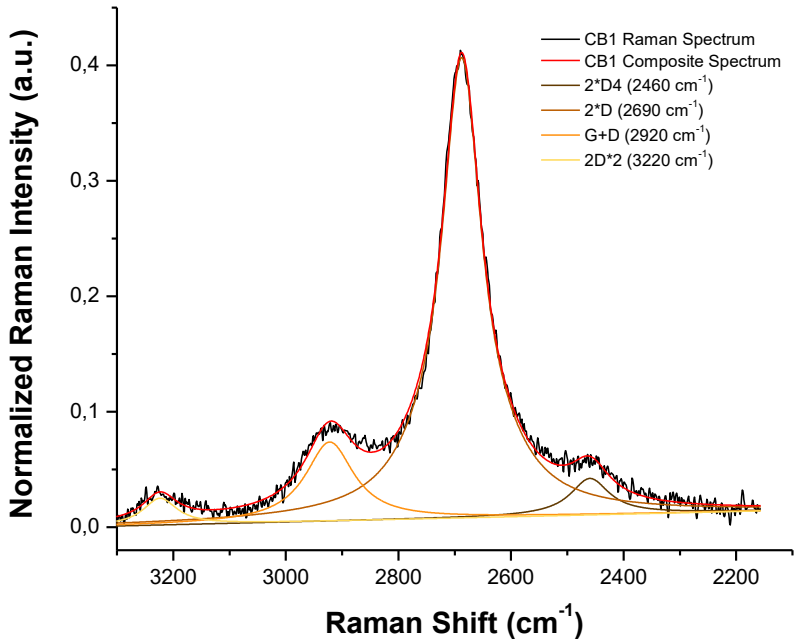

Figure 1.7. Raman spectra of CB1 in the 2000-3000cm^{-1} region**.**

G and D bands were also observed in the Raman spectrum of the CB2 sample. However, a broadening of the G and D bands with respect to the ones of the CB1 together with an increase of the intensities of the signals related to amorphous carbon bands (1530 cm^{-1}, 1455 cm^{-1}, and at 1245 cm^{-1}) was observed [50]. All these features reveal a lower degree of graphitization and the related increase in structural disorder in the CB2 with respect to CB1. Moreover, it is important to note that the G band moved away from the position typical of the graphite at 1585 cm^{-1} and shifted towards ~1600 cm^{-1}. This shift was previously observed in other studies

[49,51]. No significant signals were observed in the second order region of the Raman spectrum.

Raman spectrum of CNP4 shows a higher level of noise and a different background slope compared to the spectra of the other samples. We infer that this behaviour was mainly due to the photoluminescence of the CNP, as confirmed by fluorescence measurement (see hereafter).

The amorphous carbon content in this sample was indicated by the broad and overlapping bands across the spectrum. The G band does not only comprise the peak at ~1585 cm^{-1} but also the D2 band known from disordered graphitic lattices at ~1620 cm^{-1}. D band, not very well defined, seems to be centred at 1300 cm^{-1}. This suggests that it mainly arises from larger aromatic features with six or more fused rings [27]. The overlap between D and G bands was deconvoluted into three bands at ~1550 cm^{-1}, at 1425 cm^{-1} and 1370 cm^{-1} which represent typical structures in amorphous carbons (especially smaller aromatic ring systems) as well as the semicircle "breathing" of aromatic rings [49]. Few other bands were observed in the present spectrum: the D4 band at 1145 cm^{-1} and the peak at ~1200 cm^{-1}, that were previously assigned to sp^2-sp^3 bonds with C–C and C=C stretching vibrations of polyene-like structures and to the aryl-alkyl ether respectively, and the bands at 1030 and 1840 cm^{-1}, previously attributed to oxygen-related functional groups [37].

In order to confirm the assignment of the Raman shifts observed for CNP4, thermal annealing at 700 °C was performed. As expected, the Raman analysis (Figure 1.8) revealed, together with a reduction of the spectral noise due to photoluminescence, a decrease of the intensity of the D3 band, while G and D bands rise thus confirming a partial graphitization of the sample. In fact, despite the well-established association of the D band with defects and disorder, the appearance of this signal requires ordered graphene-like domains to be present [26].

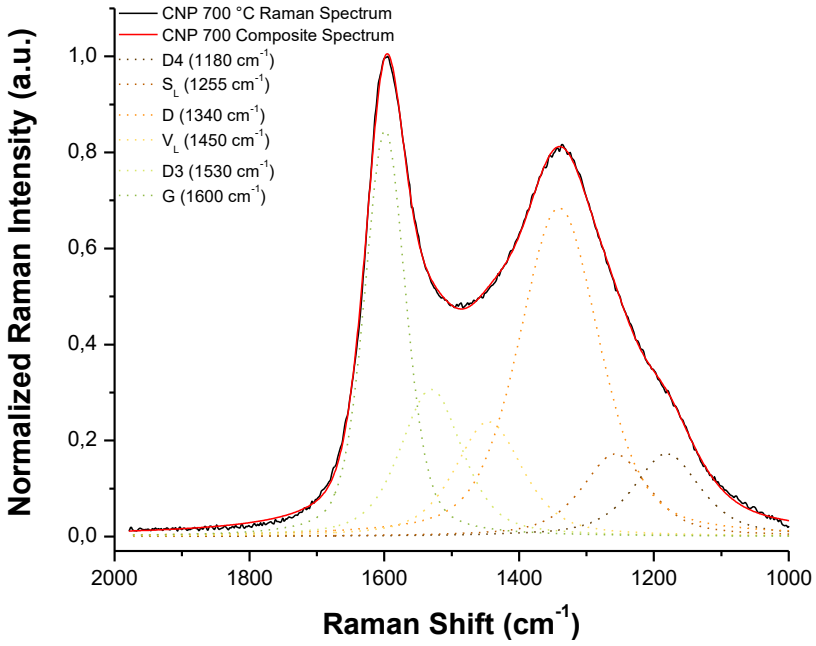

Figure 1.8. Raman spectra of CNP4 after thermal annealing.

Thermogravimetric analysis (TGA, Figure 1.6b) was performed in inert atmosphere (N_2) on CNP4 in comparison with CB1 and CB2. CNP4 resulted stable up to 250 °C, indicating that the nanoparticles do not have significant amount of adsorbed species. Subsequently a continuous 40% loss of weight in the 250–700 °C range was detected. This event may be attributed to both loss of oxygenated functional groups and/or to the partial graphitization of the sample [52].

The CB2 sample showed a 15% of loss of weight, with a first loss around 150 °C likely due to the desorption of water, while CB1 owns a high stability in all range of temperatures considered, in agreement with the high degree of crystallinity.

ECNMs are intrinsically hydrophobic. However, oxygenated functionalities (-OH, -COOH, =O) may be present after synthesis or purposely inserted to increase the hydrophilicity. In fact, NPs that are intended for systemic use need to form stable aqueous suspensions. Electrostatic repulsion among

particles, and consequently high ζ -potential values, either positive or negative, should be achieved in order to ensure stability and avoid agglomeration of the particles [53]. Furthermore, oxygenated functionalities provide a suitable linkage for a wide range of moieties.

Figure 1.6c reports the ζ -potential values of CNP4 and reference samples suspended in ultrapure water at 25 °C as function of pH. All samples exhibit a negative zeta potential in the pH range from 2 to 10 that gradually increases with increasing of the pH of the suspension. These values indicate that the nanoparticles are surrounded by hydrophilic negatively-charged groups, likely acidic carboxylic or phenolic groups formed during the synthesis.

The presence of acidic groups was confirmed and quantified by titration using the dye thionine acetate [29,30]. It was found that a single particle of CNP4 is decorated by 4×10^4 acidic groups having a density of 3 groups/nm^2. CB1 exhibited a density of 0.96 groups/nm^2, in agreement with the ζ -potential values less negative than CNP4.

1.3.2 Optical properties

The absorption spectra of CNP4 and reference spectra suspended in water were recorded in the UV–vis–NIR range (Figure 1.9). As expected, the carbon black samples were opaque in the whole range. CNP4 also absorb light in the whole range, however, the absorbance in the NIR region was much lower than the carbon black samples. This was expected due to the less extended sp^2 carbon framework, as shown by Raman analysis [54].

Previous studies indicate that some ECNM exhibit fluorescence [21,55,56]. In the present case, the fluorescence spectra (Figure 1.10) revealed obvious excitation-dependent emission spectra, which present maximum of emission in the wavelength range of 345–375 nm.

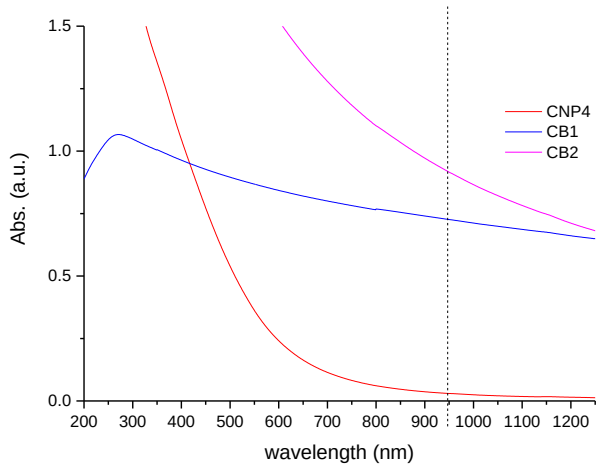

Figure 1.9. UV-Vis-NIR absorption spectra of CNP4 suspension (0.05 mg/ml) and reference samples.

The confocal microscopy analysis of the CNP4 suspension in water was also performed in order to confirm the fluorescence properties of the NPs. The nanoparticles emit in the blue light range after excitation in the 340–360 nm range (Figure 1.10, inset).

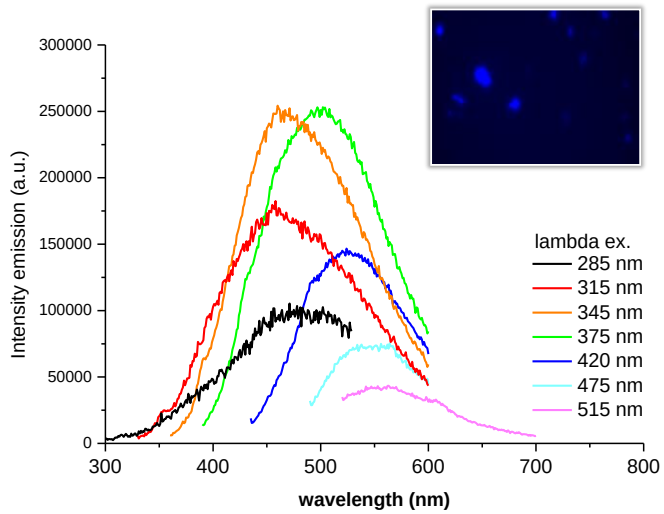

Figure 1.10. Excitation-dependent emission spectra of CNP4. Inset shows a confocal laser scanning image of the carbon sphere obtained by using a drop of an aqueous suspension of CNP4, excitation wavelength range 340-360 nm.

1.3.3 Photo-thermal and photodynamic properties

PT activity under NIR laser beam irradiation was investigated in comparison with the two reference samples CB1 and CB2 by monitoring the temperature of the suspension during exposure to NIR radiation for 10 min. As shown in Figure 1.11a, all the NPs produced intense heat release. Irradiation of the CNP4 suspension induced an increase of the temperature of 40 °C by respect to water in less than 3 min. The thermal effect was lower to those observed with CB1 sample, in agreement with the lower optical absorbance in the NIR region (Figure 1.9), but still enough to reach a temperature enough for cell death induction. Unexpectedly, a lower thermal capacity was found for CB2 by respect to CB1. Since the optical absorbance in the NIR region of CB2 was higher than CB1 (Figure 1.9) this result suggests that heat dissipation capacity increases with the graphitic degree of the material, thus confirming what found previously on carbon nanotubes [57].

PD properties rely on the ability of the NPs to undergo energy or electron transfer reactions to oxygen once activated by light. Two different mechanisms are known. In the first (type I reactions) superoxide radicals ($O2^{\cdot -}$) are generated while in the second mechanism (type II) reactions singlet oxygen ($^1O_2$) is generated [58]. Superoxide radicals undergo a series of well-known reactions that lead to the generation of the highly cytotoxic hydroxyl radicals ($OH^{\cdot}$) [59].

The ability of the carbon samples to generate ROS upon NIR radiation was studied using the EPR spectroscopy coupled with the spintrapping technique. The generation of reduced species of oxygen (hydroxyl or superoxide radicals) was monitored by using the spin trap DMPO while the probe 4-oxo-TMP was used to monitor the generation of the singlet oxygen ($^1O_2$). This probe specifically reacts with singlet oxygen generating the stable free radical 4-oxo-TEMPO that exhibits a (1:1:1) three lines spectra (aN = 15.7 G) [59]. For comparison, a commercial sample of fullerene functionalized with hydroxyl groups $C_{60}(OH)_n$, was used as positive control

[60]. Following irradiation with the NIR laser beam of an aqueous suspension of CNP4, no signal was obtained using the spin trap DMPO (data not shown) while the typical spectra of 4-oxo-TEMPO was observed using the 4-oxo-TMP probe (Figure 1.11b). This indicates that the material is able to transfer the absorbed energy to the ground state triplet oxygen by a type II mechanism generating singlet oxygen, while no type I mechanism was observed.

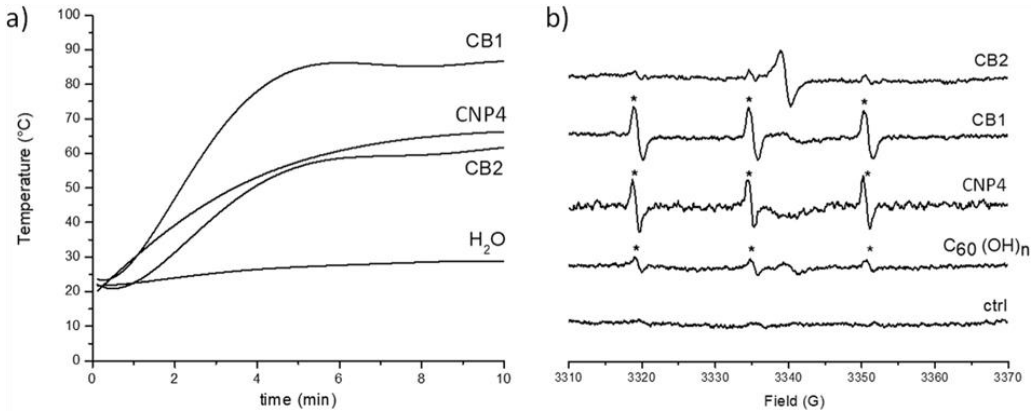

Figure 1.11. a) Photothermal activity. Temperature change curves of CNP4, CB1 and CB2 suspension during NIR laser irradiation; b) Singlet oxygen generation. EPR spectra generated after NIR laser irradiation of a suspension of the samples (2 mg/ml) in the presence of TMP (50.5 mM). The three lines signal correspondent to the 4-oxo-TEMPO species is indicated by asterisks.

The experiments were repeated i. by fluxing with nitrogen to remove oxygen or ii. in the presence of the singlet oxygen scavenger sodium azide (Figure 1.12). In both cases a significant reduction of the signal was observed further confirming the generation of singlet oxygen.

From the intensity of the EPR spectra in Figure 1.11b it is possible to observe that, similarly to CB1, CNP4 are able to generate singlet oxygen with and efficiency higher than fullerenol, while CB2 appears inert. In the latter case in fact, a single pick only was observed, not due to ROS but to the presence of isolated carbon-centred radical species confined in the internal structure of the material [61].

To the best of our knowledge, this is first study reporting the intrinsic ability of saccharides-derived nanoparticles to generate singlet oxygen. Albeit the structural heterogeneity of the particles hampers a detailed description of the photo-chemical processes leading to ROS generation, we undoubtedly confirm the presence of moieties able to be excited to a singlet state S1 that in turn undergo intersystem crossing to a T1 triplet state having halftime long enough to transfer energy to ground oxygen. On the other hand, the excited electrons and the correspondent positive holes of such moieties do not have a redox potential allowing the reduction of oxygen to superoxide. Oppositely to the release of heat, the generation of singlet oxygen does not appear to be correlated to the graphitic degree of the materials.

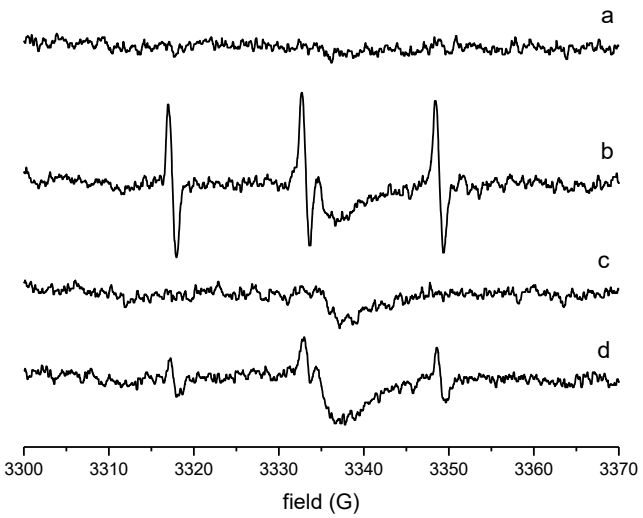

Figure 1.12. Singlet oxygen generation by CNP4. EPR spectra obtained after irradiation with NIR laser beam of a) phosphate buffer 4-oxo-TMP solution; b) phosphate buffer CNP4 suspension in the presence of 4-oxo-TMP; c) like (b) by fluxing nitrogen to remove oxygen; d) like (b) in the presence of the scavenger NaN_3.

1.3.4 Redox activity of CNP

ECNMs exhibit antioxidant properties due to their ability to scavenge ROS. This property has been early reported for fullerene [62], carbon nanotubes [13,63], and carbon soot [61].

The antioxidant efficiency appears related to the structural characteristics of ECNMs [56]. For example, diameter, length, composition, abundance of defects and chirality are known to modulate the scavenging activity of SWCNTs [64–68]. Defects are particularly effective in modulating the antioxidant activity since their abundance modifies the ratio between sp^2 and sp^3 hybridized carbon atoms that in turn modulate the electronic properties of the material. In fact, the scavenging may occur through different pathways, like electron exchange between the particle and the radical specie, addition of the radical on the carbon backbone [61] and, furthermore, by hydrogen donation to the free radical species by surface functionalities [69].

The scavenging activity of carbon nanoparticles toward the most aggressive ROS, hydroxyl radicals (HO·), was tested by means of EPR spectroscopy coupled with spin trapping technique. Hydroxyl radicals were generated by the Fenton reaction as described in the method section. The high amount of radicals generated in this condition is proved by the intense (1:2:2:1) four-line EPR signal recorded, correspondent to the DMPO/HO· adduct (aN=aH= 14.6 G) (Figure 1.13a). When the reaction was performed in the presence of the nanoparticles, the signal was completely suppressed in the case of CB1 and CB2, while for CNP4 the EPR signal decreased, suggesting a scavenging capability lower than the reference samples. The higher activity observed for the carbon black samples might be due to an abundance of crystalline patches higher by respect to CNP4. This suggests a mechanism involving the addition of free radicals to the carbon backbone or, alternatively, an electron transfer process. Conversely, a mechanism due to hydrogen donation from the functional groups exposed to the surface to

the hydroxyl radicals may be excluded since CNP4, exhibit abundance of surface functionalities higher than CB1.

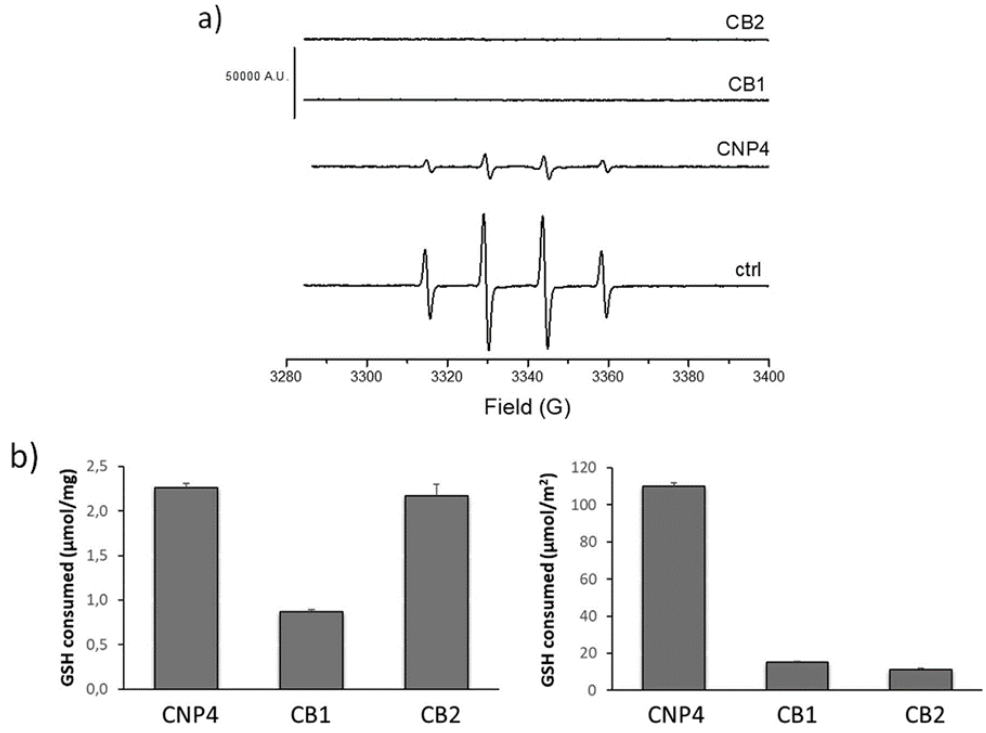

Figure 1.13. a) Scavenging activity toward hydroxyl radicals. EPR spectra obtained in a buffered solution containing 50 mM DMPO, 1.7 mM $FeSO_4$, 32 mM H_2O_2 (control) and in the same solution in the presence of 2 mg/ml of the CNP4 or reference samples; b) Amount of glutathione consumed following the interaction with CNP4, CB1, CB2 expressed as a function of mass (right) and as a function of surface area (left).

Liu et al. [14] previously reported the ability of some ECNMs to oxidize glutathione, one of the main antioxidant molecules of cells. In cells, this property may result in a pro-oxidant effect. The oxidative potency of CNP4 was tested in comparison with two reference samples by monitoring the glutathione depletion capacity. Figure 1.13b shows the degree of oxidation of GSH after 2 h of interaction with CNP4 or with the reference samples, quantified by the Ellman's reagent. The effects of CNP4 and CB2 on GSH

are comparable, while the depletion caused by CB1 was lower. According to Liu et al., [14] a correlation between the exposed surface area and the amount of GSH consumed exists. In the present case, when compared at equal surface area (Figure 1.13b), the two carbon black samples exhibit a similar specific reactivity, thus confirming the role of surface area previously reported by Liu et al. However, in the case of CNP4 a higher reactivity was observed. The UV–Vis spectra recorded on the supernatant after incubation of the samples with GSH were also recorded (Figure 1.14). A spectrum having a maximum at around 300 nm likely due to generation of an oxidized form of glutathione was observed for all samples, demonstrating that the decrease in GSH concentration was due to its oxidation and not to an adsorption of the molecules at the NP surfaces.

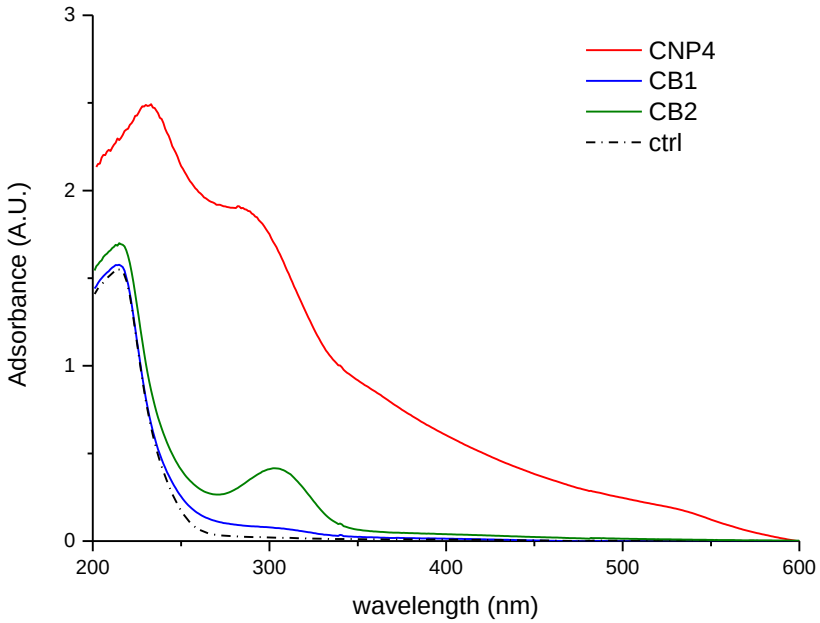

Figure 1.14. UV-Vis spectra of the GSH solution after incubation for 2 h at 37°C with the samples.

The peculiar reactivity of CNP4 might be attributed to a different abundance of active sites that Liu et al. suggested to be superoxide radicals adsorbed at

the surface. Note that the capacity of CNP4 to consume glutathione (2.26 μmol/mg) was much higher when compared with the amount of hydroxyl radicals scavenged (0.00475 μmol/mg) suggesting the prevalence of the pro-oxidant properties.

1.3.5 Characterization of nanoparticles in cell media

The size distribution and stability of CNP4 in the cell media was evaluated by DLS, at different time incubation correspondent to those used in cellular tests (0, 24 and 48 h). The analyses (Figure 1.15) showed one single population of particles having mean hydrodynamic diameter around 200 nm, compatible with the presence of monodisperse particles surrounded with a protein corona. No agglomeration or change in mean hydrodynamic diameter was observed during the 48 h of incubation.

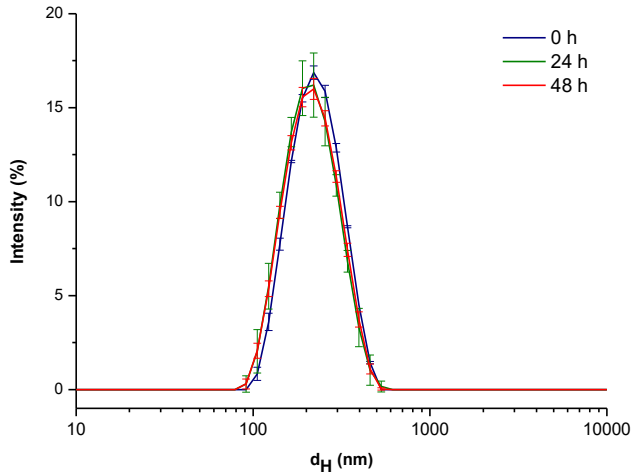

Figure 1.15. Representative DLS analysis of CNP4 incubated for 0, 24 and 48 h in DMEM at the concentration of 40μg/mL. Hydrodynamic diameter: 201.9 ± 1.4 nm for t=0h, 193.2 ± 2.4 nm for t=24h and 193.5 ± 2.0 nm for t=48h.

1.3.6 Cytotoxicity toward RAW 264.7 and uptake

CNP were firstly tested for their ability to induce cytotoxicity, measured as leakage of intracellular LDH into the extracellular medium. RAW 264.7 macrophages were incubated for 24 or 48 h with the NPs at a concentration range of 10–320 μg/ml (Figure 1.16a). A sample of pyrogenic silica was used as positive control [70]. CNP4 do not elicit any cytotoxic effect on macrophages in a wide range of concentrations. A significant cytotoxic effect was observed only after 48 h of exposure with CNPs at the very high concentrations of 160 μg/ml (Figure 1.16a). On the other hand, in these conditions, an effect due to overload is likely.

TEM analysis was performed on RAW 264.7 incubated in the presence of CNP4 (Figure 1.16b). Unexposed cells (negative control) showed normal morphology without specific ultrastructure alterations. Nuclei are well defined and all the organelles visible. Cells exposed at 40 μg/ml and 160 μg/ml of CNP4 for 24 and 48 h respectively, show groups of single particles inside endo/phagocytosis organelles (endosomes) with an increased dose and time dependent uptake. No sign of lysis of the phagolysosome membranes was observed.

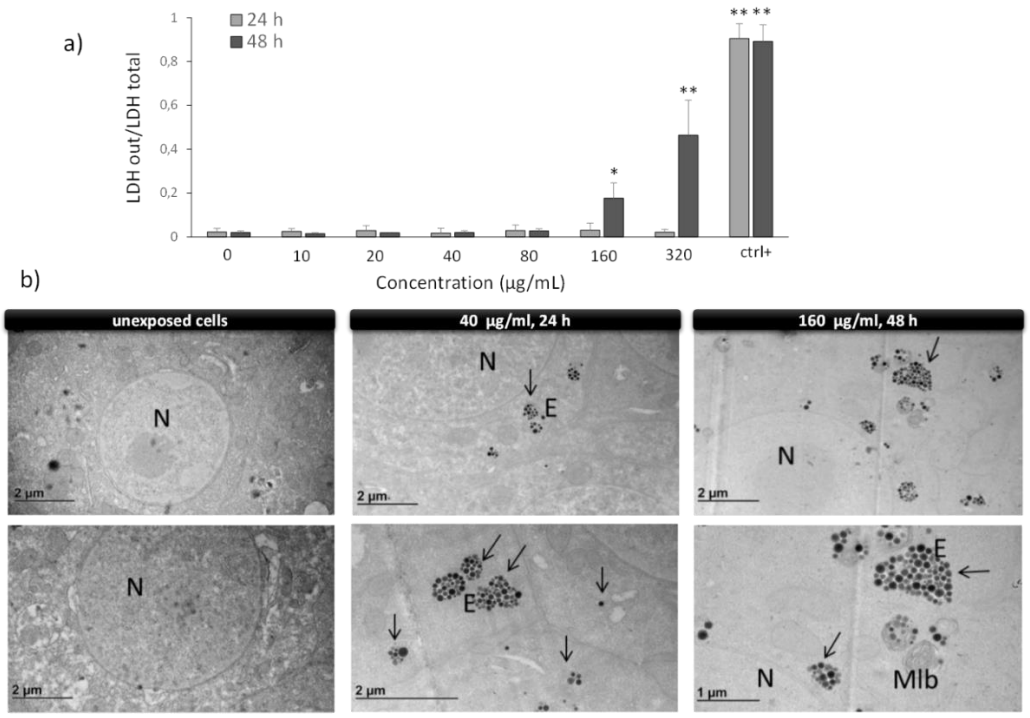

Figure 1.16. a) Cytotoxicity of CNP4 toward macrophages: LDH leakage following exposure to CNP4 for 24 or 48h at different doses. crl- is without the nanoparticles; a sample of amorphous silica has been used as positive control. Vs ctrl (0 µg/ml) *p < 0,05, ** p<0.01; b) internalization of CNP4 in macrophages. The arrows indicate the nanoparticles; (N) nucleus; (Mlb) multi lamellar bodies; (E) endosomes.

These results exclude that the observed low toxicity was a consequence of the absence of uptake of the particles by macrophages. The mechanism of uptake is known to depend upon the size and surface charge of nanoparticles [71]. In the present case, since CNP4 are not conjugated with targeting agents, an aspecific endocytosis is expected. In this case, the small size and the negative surface of CNP4 should favour their cellular uptake. In fact, although still controversial, there are evidences that anionic nanoparticles are more internalized than cationic ones due to the favourable electrostatic interactions between the surface of the particles and the cell plasma-membrane [72,73].

1.3.7 Effect of CNP4 on the redox homeostasis of macrophages

CNPs to modulate the redox homeostasis in macrophages was evaluated by measuring the generation of ROS or NO on non-activated or lipopolysaccharide-activated macrophages following incubation with the NPs at non-cytotoxic concentrations (40–80 µg/ml) (Figure 1.17).

The NPs did not induce ROS or NO production by macrophages under basal conditions. On the contrary, when cells activated with 1 µg/ml LPS were incubated with CNP4, a clear, dose dependent, inhibition of ROS and NO generation was observed, indicating that an antioxidant behaviour of NPs prevails in activated macrophages. To get insight onto the molecular mechanism of this effect, the amount of intracellular reduced glutathione was also measured (Figure 1.17): we did not observe any change in reduced intracellular GSH, suggesting that the GSH consumed by the NPs, as shown by cell-free tests, is efficiently restored by the glutathione reductase system of cells. The predominant antioxidant effect may be therefore attributed to the scavenging ability of the nanoparticles toward hydroxyl radicals.

Since ROS and NO are typical signs or macrophage activation during inflammatory diseases (e.g. atherosclerosis, vasculitis, rheumatoid arthritis) [74], our results suggest a potential use of CNPs in mitigating the damages induced by activated macrophages on neighbour cells.

Furthermore, the low toxicity and the antioxidant effect toward macrophages suggest a possible safe use of these nanoparticles in nanomedicine. On the other hand, the antioxidant capability may mitigate the oxidative burst typical of activated cells during photo-thermal or photodynamic treatments. Further studies are in progress to investigate this latter aspect.

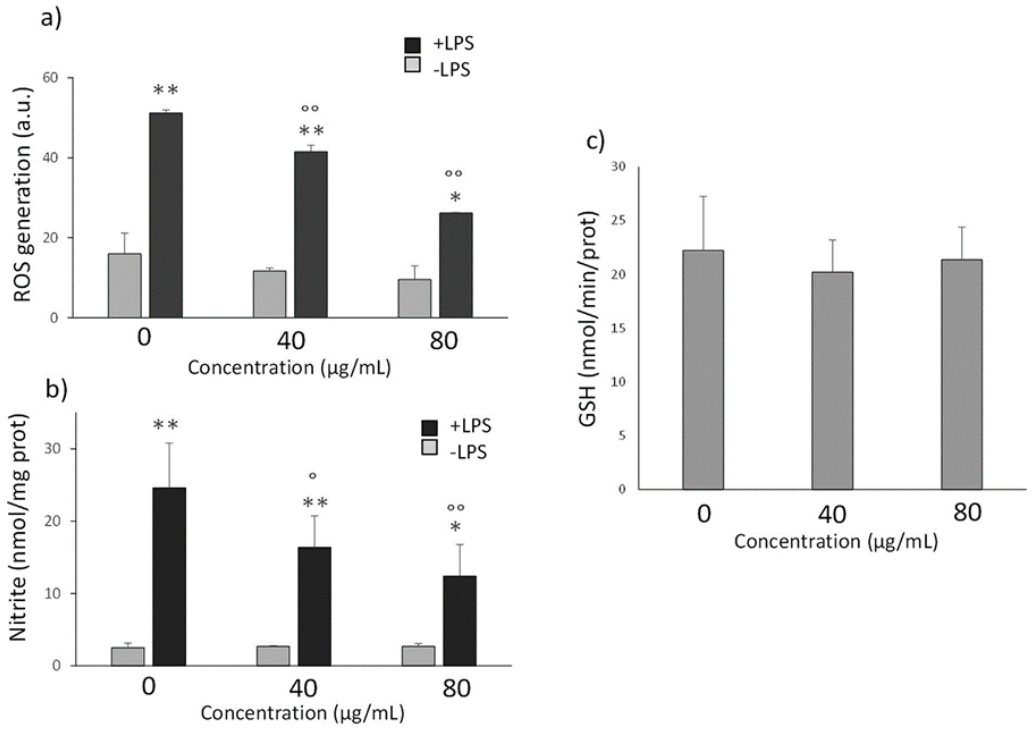

Figure 1.17. a) ROS generation by non-activated and LPS- activated macrophages exposed to CNP4 for 24 h at non-cytotoxic doses. b) NO generation by non-activated and LPS- activated macrophages exposed to CNP4 for 24 h at non-cytotoxic doses. c) intracellular reduced glutathione in macrophages exposed to CNP4 for 24 h at non-cytotoxic doses. Vs ctrl (0 µg/ml): ** $p<0.01$; * $p<0.05$; vs control + LPS: °° $p<0.01$; ° $p<0.05$.

1.3.8 Effect of CNP4 on the cytokines production of macrophages

Cytokines production is a paramount parameter of macrophages activation. To investigate how CNP4 affect this issue, we measured the levels of TNF-α, chosen as a paradigmatic pro-inflammatory cytokine, and IL-10, chosen as a paradigmatic immune-suppressive cytokine, in RAW 264.7 cells, treated with CNP4 at 40 and 80 µg/ml for 24 h, two concentrations that were not cytotoxic (figure 1.16a), did not

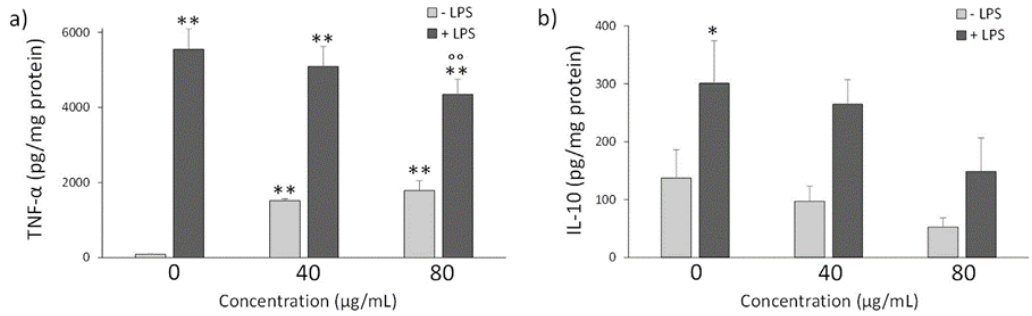

Figure 1.18. a) TNF-α production by non-activated and LPS- activated macrophages exposed to CNP4 for 24 h at non-cytotoxic doses. b) IL-10 production by non-activated and LPS- activated macrophages exposed to CNP4 for 24 h at non-cytotoxic doses. Vs ctrl (0 µg/ml): ** $p<0.01$; * $p<0.05$; vs control + LPS: °° $p<0.01$; ° $p<0.05$.

alter intracellular ROS and GSH, nor production of nitrite (Figure 1.17), either in unstimulated macrophages or in LPS-stimulated (i.e. activated) macrophages. As shown in Figure 1.18, both concentrations increased the production of TNF-α in resting macrophages. On the other hand, when LPS was added to mimic the typical macrophage activation occurring in inflammatory situations [75] (e.g. cardiovascular diseases, bacterial infections, cancers). CNP4 did not further increase TNF-α, meaning that they do not amplify the TNF-α-mediated inflammation. Moreover, CNP4 did not significantly alter IL-10 production, neither in basal conditions nor upon LPS stimulation, a strong inducer of IL-10 production in macrophages [76]. In the oncological setting, a chronic inflammation sustained by activated macrophages favours tumour progression. Such prolonged activation, however, paradoxically leads to immune-system exhaustion, inducing an immune-suppressive status that further promotes tumour growth [77]. One of the most common signs is the production of IL-10 by macrophages, that become pro-tumourigenic [77].

Overall, this experimental set suggests that CNP4 did not exacerbate the production of TNF-α nor IL-10 in activated macrophages. Since CNP4 prevent the undesired production of cytokines that amplify inflammation and/or shift the micro-environment from inflammation to immune-suppression, our data reinforce

the assumption that CNP4 are promising tools for those conditions where an excessive activation of macrophages is dangerous, such as cardiovascular and chronic inflammatory diseases potentially leading to tumourigenesis.

1.4 Conclusions

In conclusion, CNP4 exhibit both pro- and anti-oxidant capabilities in cell-free system. However, in macrophages the antioxidant effect prevails suggesting a possible protective effect from the oxidative/nitrosative damage produced by activated macrophages. Following NIR activation CNP exhibit PT and PD properties. Interestingly, all these properties appear to be modulated by the bulk structure of carbon NPs, thus suggesting a possible optimization of these functional properties. We believe that the present findings contribute to the advancement in a safe use of elemental carbon NPs in nanomedicine. Furthermore, they suggest a possible use in all those diseases where an improper macrophage activation is undesirable, such as cardiovascular and chronic inflammatory diseases.

1.5 References

[1] R.H. Baughman, A.A. Zakhidov, W.A. de Heer, Carbon nanotubes-the route toward applications, Science 297 (2002) 787–792

[2] A.K. Geim, Graphene: status and prospects, Science 324 (2009) 1530–1534

[3] K. Albert, H. Hsin-Yun, Carbon-based materials for photo-triggered theranostic applications, Molecules 21 (2016) E1585

[4] S. Banerjee, T. Hemraj-Benny, S.S. Wong, Covalent surface chemistry of single-walled carbon nanotubes, Adv. Mater. 17 (2005) 17–19

[5] D. Tasis, N. Tagmatarchis, A. Bianco, M. Prato, Chemistry of carbon nanotubes, Chem. Rev. 106 (2006) 1105–1136

[6] G. Obaid, M. Broekgaarden, A. Bulin, H. Huang, J. Kuriakose, J. Liu, H. Tayyaba, Photonanomedicine: a convergence of photodynamic therapy and nanotechnology, Nanoscale 8 (2016) 12471–12503

[7] C.M. Courtney, S.M. Goodman, J.A. McDaniel, N.E. Madinger, A. Chatterjee, P. Nagpal, Photoexcited quantum dots for killing multidrug-resistant bacteria, Nat. Mater. 15 (2016) 529–534

[8] P. Zhang, C. Hu, W. Ran, J. Meng, Q. Yin, Y. Li, Recent progress in light-triggered nanotheranostics for cancer treatment, Theranostics 6 (2016) 948–968

[9] J. Miller, Photodynamic Therapy: the sensitization of cancer cells to light, J. Chem. Educ. 76 (1999) 592–594

[10] Z. Li, C. Wang, L. Cheng, H. Gong, S. Yin, Q. Gong, Y. Li, Z. Liu, PEG-functionalized iron oxide nanoclusters loaded with chlorin e6 for targeted, NIR light induced, photodynamic therapy, Biomaterials 34 (2013) 9160–9170

[11] H. Kim, K. Chung, S. Lee, D.H. Kim, H. Lee, Near-infrared light-responsive nanomaterials for cancer theranostics, WIREs Nanomed. Nanobiotechnol. 8 (2016) 23–45.

[12] M. Ghiazza, G. Vietti, I. Fenoglio, Carbon nanotubes: properties, applications, and toxicity, in: J. Njuguna, K. Pielichowski, H. Zhu (Eds.), Composites Science and Engineering No. 49, Woodhead Publishing, U.K, 2014, pp. 147–174

[13] I. Fenoglio, M. Tomatis, D. Lison, J. Muller, A. Fonseca, J.B. Nagy, B. Fubini, Reactivity of carbon nanotubes: free radical generation or scavenging activity? Free Radic. Biol. Med. 40 (2006) 1227–1233

[14] X. Liu, S. Sen, J. Liu, I. Kulaots, D. Geohegan, A. Kane, Alex A. Puretzky, C.M. Rouleau, K.L. More, G.T.R. Palmore, R.H. Hurt, Antioxidant deactivation on graphenic nanocarbon surfaces, Small 7 (2011) 2775–2785

[15] S. Galadaria, A. Rahman, S. Pallichankandy, F. Thayyullathil, Reactive oxygen species and cancer paradox: to promote or to suppress? Free Rad. Biol. Med. 104 (2017) 144–164

[16] Z. Markovic, V. Trajcovic, Biomedical potential of the reactive oxygen species generation and quenching by fullerenes (C60), Biomaterials 29 (2008) 3561–3573

[17] C.-Y. Chen, C.T. Jafvert, The role of surface functionalization in the solar light induced production of reactive oxygen species by single-walled carbon nanotubes in water, Carbon 49 (2011) 5099–5106

[18] R. Demir-Cakan, N. Baccile, M. Antonietti, M. Titirici, Carboxylate-rich carbonaceous materials via one-step hydrothermal carbonization of glucose in the presence of acrylic acid, Chem. Mater. 21 (2009) 484–490

[19] Z. Yi, Y. Liang, X. Lei, C. Wang, J. Sun, Low-temperature synthesis of nanosized disordered carbon spheres as an anode material for lithium ion batteries, Mater. Lett. 61 (2007) 4199–4203

[20] M. Ajmal, U. Yunus, A. Matin, N.U. Haq, Synthesis, characterization and in vitro evaluation of methotrexate conjugated fluorescent carbon nanoparticles as drug delivery system for human lung cancer targeting, J. Photochem. Photobiol. B 153 (2015) 111–120

[21] N. Li, T. Li, C. Hu, X. Lei, Y. Zuo, H. Han, Targeted near-infrared fluorescent turn-on nanoprobe for activatable imaging and effective phototherapy of cancer cells, ACS Appl. Mater. Interfaces 8 (2016) 15013–15023

[22] Z. Miao, H. Wang, H. Yang, Z. Li, L. Zhen, C. Xu, Glucose-derived carbonaceous nanospheres for photoacoustic imaging and photothermal therapy, ACS Appl. Mater. Interfaces 8 (2016) 15904–15910

[23] B.R. Selvi, D. Jagadeesan, B.S. Suma, G. Nagashankar, M. Arif, K. Balasubramanyam, M. Eswaramoorthy, Tapas K. Kundu, Intrinsically fluorescent carbon nanospheres as a nuclear targeting vector: delivery of membrane-impermeable molecule to modulate gene expression in vivo, Nano Lett. 8 (2008) 3182–3188

[24] D. Wei, R. Dave, R. Pfeffer, Mixing and characterization of nanosized powders: an assessment of different techniques, J. Nanopart. Res. 4 (2002) 21–41

[25] F. Tuinstra, J.L. Koenig, Raman spectrum of graphite, J. Chem. Phys. 53 (1970) 1126–1130

[26] A.C. Ferrari, J. Robertson, Interpretation of Raman spectra of disordered and amorphous carbon, Phys. Rev. B 61 (2000) 14095–14107

[27] A. Sadezky, H. Muckenhuber, H. Grothe, R. Niessner, U. Pöschl, Raman microspectroscopy of soot and related carbonaceous materials: spectral analysis and structural information, Carbon 43 (2005) 1731–1742

[28] X. Li, J.I. Hayashi, C.Z. Li, FT-Raman spectroscopic study of the evolution of char structure during the pyrolysis of a Victorian brown coal, Fuel 85 (2006) 1700–1707

[29] A. Pietroiusti, M. Massimiani, I. Fenoglio, M. Colonna, F. Valentini, G. Palleschi,
A. Camaioni, A. Magrini, G. Siracusa, A. Bergamaschi, A. Sgambato, L. Campagnolo, Low doses of pristine and oxidized single-wall carbon nanotubes affect mammalian embryonic development, ACS Nano 5 (2011) 4624–4633

[30] S. Visentin, N. Barbero, S. Musso, V. Mussi, C. Biale, R. Ploeger, G. Viscardi, A sensitive and practical fluorimetric test for CNT acidic site determination, Chem. Commun. 46 (2010) 1443–1455

[31] B. Tian, C. Wang, S. Zhang, L. Feng, Z. Liu, Photothermally enhanced photodynamic therapy delivered by nano-graphene oxide, ACS Nano 5 (2011) 7000–7009

[32] R. Gassino, I. Kokalari, A. Vallan, I. Fenoglio, Guido Perrone, A compact diode laser based all-fiber delivery system for PDT+PTT with integrated temperature sensing capabilities, in: D.H. Kessel, T. Hasan (Eds.), Proc. SPIE No. 10047, Int. Soc. Optical Engineering, USA, 2017

[33] F. Tietze, Enzymic method for quantitative determination of nanogram amounts of total and oxidized glutathione: applications to mammalian blood and other tissues, Anal. Biochem. 27 (1969) 502–522

[34] M. Polimeni, E. Gazzano, M. Ghiazza, I. Fenoglio, A. Bosia, B. Fubini, D. Ghigo, Quartz inhibits glucose 6-phosphate dehydrogenase in murine alveolar macrophages, Chem. Res. Toxicol. 21 (2008) 888–894

[35] A. Kroll, M.H. Pillukat, D. Hahn, J. Schnekenburger, Interference of engineered nanoparticles with in vitro toxicity assays, Arch. Toxicol. 86 (2012) 1123–1236

[36] G.R. Gulino, M. Polimeni, M. Prato, E. Gazzano, J. Kopecka, S. Colombatto, D. Ghigo, E. Aldieri, Effects of chrysotile exposure in human bronchial epithelial cells: insights into the pathogenic mechanisms of asbestos-related diseases, Environ. Health Perspect. 124 (2016) 776–784

[37] Q. Wang, H. Li, L. Chen, X. Huang, Monodispersed hard carbon spherules with uniform nanopores, Carbon 39 (2001) 2211–2214

[38] Y. Gong, H. Wang, Z. Wei, L. Xie, Y. Wang, An efficient way to introduce hierarchical structure into biomass-based hydrothermal carbonaceous materials, ACS Sustain. Chem. Eng. 2 (2014) 2435–2441

[39] P. Zhang, Z. Qiao, S. Dai, Recent advances in carbon nanospheres: synthetic routes and applications, Chem. Commun. 51 (2015) 9246–9256

[40] Y. Gong, L. Xie, H. Li, Y. Wang, Sustainable and scalable production of monodisperse and highly uniform colloidal carbonaceous spheres using sodium polyacrylate as the dispersant, Chem. Commun. 50 (2014) 12633–12636

[41] F. Danhier, N. Lecouturier, B. Vroman, C. Jérôme, J. Marchand-Brynaert, O. Feron, V. Préat, Paclitaxel-loaded PEGylated PLGA-based nanoparticles: in vitro and in vivo evaluation, J. Control Release 133 (2009) 11–17

[42] J. Zhao, M.H. Stenzel, Entry of nanoparticles into cells: the importance of nanoparticle properties, Polym. Chem. 9 (2018) 259–272

[43] A. Jorio, G. Dresselhaus, M.S. Dresselhaus, Raman Spectroscopy in Nanoscience and Nanometrology: Carbon Nanotubes, Nanographite and Graphene, Wiley-VCH, Hoboken, NJ, 2010

[44] H.M. Heise, R. Kuckuk, A.K. Ojha, A. Srivastava, V. Srivastava, B.P. Asthana, Characterisation of carbonaceous materials using Raman spectroscopy: a comparison of carbon nanotube filters, single- and multi-walled nanotubes, graphitised porous carbon and graphite, J. Raman Spectrosc. 40 (2009) 344–353

[45] A. Cuesta, P. Dhamelincourt, J. Laureyns, A. Martinezalonso, J.M.D. Tascon, Raman microprobe studies on carbon materials, Carbon 32 (1994) 1523–1532

[46] A. Ferrari, Raman spectroscopy of graphene and graphite: disorder, electron–phonon coupling, doping and nonadiabatic effects, Solid State Commun. 143 (2007) 47–57

[47] J. Schwan, S. Ulrich, V. Batori, H. Ehrhardt, S.R.P. Silva, Raman spectroscopy on amorphous carbon films, J. Appl. Phys. 80 (1996) 440–447

[48] J. McDonald-Wharry, M. Manley-Harris, K. Pickering, Carbonisation of biomassderived chars and the thermal reduction of a graphene oxide sample studied using Raman spectroscopy, Carbon 59 (2013) 383–405

[49] M. Wang, D.G. Roberts, M.A. Kochanek, D.J. Harris, L. Chang, C. Li, Raman spectroscopic investigations into links between intrinsic reactivity and char chemical structure, Energy Fuels 28 (2014) 285–290

[50] M. Sevilla, A.B. Fuertes, Chemical and structural properties of carbonaceous products obtained by hydrothermal carbonization of saccharides, Chem. Eur. J. 15 (2009) 4195–4203

[51] O. Frank, G. Tsoukleri, J. Parthenios, K. Papagelis, I. Riaz, R. Jalil, K.S. Novoselov, C. Galiotis, Compression behavior of single-layer graphenes, ACS Nano 4 (2010) 3131–3138

[52] L. Yu, C. Falco, J. Weber, R.J. White, J.Y. Howe, M. Titirici, Carbohydrate-derived hydrothermal carbons: a thorough characterization study, Langmuir 28 (2012) 12373–12383

[53] I. Bala, S. Hariharan, R. Kumar, PLGA nanoparticles in drug delivery: the state of the art, Crit. Rev. Ther. Drug Carr. Syst. 21 (2004) 387–422

[54] A.M. Schrand, B.M. Stacy, S. Payne, L. Dosser, S.M. Hussain, Fundamental examination of nanoparticle heating kinetics upon near infrared (NIR) irradiation, ACS Appl. Mater. Interfaces 3 (2011) 3971–3980

[55] M. Sevilla, A.B. Fuertes, D.C. Rezan, M.M. Titirici, M.-M. Titirici (Ed.), Sustainable Carbon Materials from Hydrothermal Processes, John Wiley & Sons, Ltd, Oxford, UK, 2013, pp. 213–294

[56] Y. Sun, B. Zhou, Y. Lin, W. Wang, K.A.S. Fernando, P. Pathak, M.J. Meziani,
B.A. Harruff, X. Wang, H. Wang, P.G. Luo, H. Yang, M.E. Kose, B. Chen, L.M. Veca,
S. Xie, Quantum-sized carbon dots for bright and colorful photoluminescence, J. Am. Chem. Soc. 128 (2006) 7756–7757

[57] R. Singh, S.V. Torti, Carbon nanotubes in hyperthermia therapy, Adv. Drug Deliv.
Rev. 65 (2013) 2045–2060

[58] M. Ochsner, J. Photophysical and photobiological processes in the photodynamic therapy of tumours, J. Photochem. Photobiol. B: Biol. 39 (1997) 1–18

[59] M. Ghiazza, E. Alloa, S. Oliaro-Bosso, F. Viola, S. Livraghi, D. Rembges, R. Capomaccio, F.O. Rossi, J. Ponti, I. Fenoglio, Inhibition of

the ROS-mediated cytotoxicity and genotoxicity of nano-TiO2 toward human keratinocyte cells by iron doping, J. Nanopart. Res. 16 (2014) 2263–2280

[60] B. Vileno, P.R. Marcoux, M. Lekka, A. Sienkiewicz, T. Fehér, L. Forró, Spectroscopic and photophysical properties of a highly derivatized C60 fullerol, Adv. Funct. Mater. 16 (2006) 120–128

[61] E. Carella, M. Ghiazza, M. Alfè, E. Gazzano, D. Ghigo, V. Gargiulo, A. Ciajolo, B. Fubini, I. Fenoglio, Graphenic nanoparticles from combustion sources scavenge hydroxyl radicals depending upon their structure, BioNanoSci 3 (2013) 112–122

[62] L.L. Dugan, D.M. Turetsky, C. Du, D. Lobner, M. Wheeler, C.R. Almli, C.K.F. Shen, T. Luh, D.W. Choi, T. Lin, Carboxyfullerenes as neuroprotective agents, Proc. Natl. Acad. Sci. USA 94 (1997) 9434–9439

[63] S. Tsuruoka, H. Matsumoto, K. Koyama, E. Akiba, T. Yanagisawa, F.R. Cassee, N. Saito, Y. Usui, S. Kobayashi, D.W. Porter, V. Castranova, M. Endo, Radical scavenging reaction kinetics with multiwalled carbon nanotubes, Carbon 83 (2015) 232–239

[64] I. Fenoglio, G. Greco, M. Tomatis, J. Muller, E. Raymundo-Piñero, F. Béguin, A. Fonseca, J.B. Nagy, D. Lison, B. Fubini, Structural defects play a major role in the acute lung toxicity of multiwall carbon nanotubes: physicochemical aspects, Chem. Res. Toxicol. 21 (2008) 1690–1697

[65] A. Galano, Carbon nanotubes: promising agents against free radicals, Nanoscale 2 (2010) 373–380

[66] A. Galano, Influence of diameter, length, and chirality of single-walled carbon nanotubes on their free radical scavenging capability, J. Phys. Chem. C 113 (2009) 18487–18491

[67] A. Martinez, A. Galano, Free radical scavenging activity of ultrashort single-walled carbon nanotubes with different structures through electron transfer reactions, J. Phys. Chem. C 114 (2010) 8184–8191

[68] P.K. Shukla, P.C. Mishra, Effects of diameter, length, chirality and defects on the scavenging action of single-walled carbon nanotubes for OH radicals: a quantum computational study, Chem. Phys. 369 (2010) 101–107

[69] V. Ruiz, L. Yate, I. García, G. Cabanero, H. Grande, Tuning the antioxidant activity of graphene quantum dots: protective nanomaterials against dye decoloration, Carbon 116 (2017) 366–374

[70] E. Gazzano, M. Ghiazza, M. Polimeni, V. Bolis, I. Fenoglio, A. Attanasio, G. Mazzucco, B. Fubini, D. Ghigo, Physicochemical determinants in the cellular responses to nanostructured amorphous silicas, Toxicol. Sci. 128 (2012) 158–170

[71] P.R. Lockman, J.M. Koziara, R.J. Mumper, D.D. Allen, Nanoparticle surface charges alter blood–brain barrier integrity and permeability, J. Drug Target. 12 (2004) 635–641

[72] E. Fröhlich, The role of surface charge in cellular uptake and cytotoxicity of medical nanoparticles, Int. J. Nanomed. 7 (2012) 5577–5591

[73] V. Sokolova, D. Kozlova, T. Knuschke, J. Buer, A.M. Westendorf, M. Epple, Mechanism of the uptake of cationic and anionic calcium phosphate nanoparticles by cells, Acta Biomater. 9 (2013) 7527–7535

[74] H.Y. Tan, N. Wang, S. Li, M. Hong, X. Wang, Y. Feng, The reactive oxygen species in macrophage polarization: reflecting its dual role in progression and treatment of human diseases (Article ID 2795090), Oxid. Med. Cell. Longev. (2016) 1–16

[75] H. Kawasaki, A mechanistic review of silica-induced inhalation toxicity, Inhal.
Toxicol. 27 (2015) 363–377

[76] S.S. Iyer, A.A. Ghaffari, G. Cheng, Lipopolysaccharide-mediated IL-10 transcriptional regulation requires sequential induction of type I IFNs and IL-27 in macrophages, J. Immunol. 185 (2010) 6599–6607

[77] J. Todoric, L. Antonucci, M. Karin, Targeting inflammation in cancer prevention and therapy, Cancer Prev. Res. 9 (2016) 895–905

Chapter 2

Assessment of the NIR-induced PT/PD efficacy toward lung tumor cells and biodegradability of carbon nanoparticles

In the previous chapter, we describe the synthesis, the physicochemical properties and the pro-/antioxidant properties of a new class of carbon nanoparticles derived from the carbonization of glucose. The NIR-induced PT and PD activity was also investigated in a cell-free system. Here, the PD and PT activities towards lung epithelial tumor cells (A549) is reported. The experiments were performed at the Department of Oncology, University of Turin, in collaboration with Prof. Chiara Riganti and Dr. Elena Gazzano. The source of NIR light was a laser designed for biomedical application developed by Prof. Guido Perrone, Dr. Riccardo Gassino and Dr. Jennifer Pogliano at the Department of Electronics, Politecnico of Turin. TEM analysis to investigate the cellular uptake was conducted by Dr. Jessica Ponti, European Commission, Directorate General Joint Research Centre, Ispra, Italy within the Framework of Access to the Joint Research Centre Physical Research Infrastructure, access project CeTECaN.

The second part is focused on the evaluation of the *in vitro* degradation of carbon nanoparticles and their safety. The experiments included cell-free studies and cellular *in vitro* studies. The latter performed at Karolinska Institute, Stockholm, in collaboration with Prof. Bengt Fadeel and Dr. Sandeep Keshavan. Raman analysis was performed at the Istituto Nazionale di Ricerca Metrologica, INRiM, Torino, Italy, by Dr. Andrea Giovannozzi.

2.1 Introduction

Cancer remains an important cause of mortality in the world. Around 9.6 million people are estimated to have died from cancer in 2018, amounting to 1 out of 6 world-wide deaths. Lung cancer is the leading cause of cancer-related death in high-income countries and one of the main causes that influence a lower life expectancy in males than in females (31.3 and 14.4 for 100000 population in men and women, respectively, in 2016) [1]. By 2035, the number of lung cancer-related deaths is expected to hike up to 3 million worldwide [2]. Varieties of treatments have been employed in lung cancer therapy and mainly include surgery and chemotherapy [3]. Nonsmall cell lung cancers represent approximately 85% of lung cancers, however, only 25- 30% are suitable for surgery. In addition, lung cancer resection is followed by low survival rate, with the exception of patients with early-stage disease [4]. On the other hand, chemotherapy for lung cancers is still associated with poor outcome due to the reduced selectivity, insufficient drug concentration in the tumor tissue and frequent development of multidrug resistance (MDR). Thus, innovative therapeutic approaches for more efficacious treatment of lung cancer are urgently needed.

Phototherapies includes irradiation of a specific tissue with light and its use dates back to ancient times. However, in the last century, they have gain great attention mainly as an alternative to tradition cancer treatments. Moreover, different studies reported that phototherapies can be combined with other therapeutical modalities in order to enhance the therapeutic efficacy.[5], [6] Following phototherapies, the interesting enhancement of the antitumoral immunity is also reported, which can not only exhibit therapeutic effects toward disseminated tumors but could also lead to advanced cancer treatment based on vaccination.[6], [7], [8]

In order to improve the potency and selectivity of phototherapies, a variety of light-responsive molecular agents, like porphyrins, or photoactive nanomaterials have been developed. Nanomaterials can exhibit intrinsic photoactivity or can be properly functionalized with molecular photosensitizers. NP could be administered via direct intratumoral injection and a prolonged retention is expected due to lack of lymphatic drainage in tumor tissue and reduced blood

flow [9] in comparison with healthy ones. Furthermore, in the case of surface functionalization with targeting agents, orally or parenterally administered nanomaterials could also provide a targeted treatment, which could remarkably reduce the side effects of the therapy.

Phototherapy can be divided in two main categories: photothermal therapy (PTT) and photodynamic therapy (PDT). PTT is an attractive therapeutic modality, which involve heating cells to therapeutic levels in order to cause alteration of the structure of endogenous molecules and lead to cell death by necrosis or apoptosis. Nanomaterials having PTT properties, like gold or iron-based NM, are able of photoconversion: absorption of electromagnetic energy with intense heat release. PDT consists in the administration of molecules or nanomaterials able to generate cytotoxic reactive oxygen species (ROS) when illuminated. In this case, the photosensitizer absorbs electromagnetic energy and transfers it to the molecule of oxygen. ROS can react with cellular vital biomolecules such as proteins, unsaturated lipids and nucleic acids leading to cell death by oxidative damage [10]. PDT treatment based on molecular photosensitizers has been already approved for non-small cell lung cancer and the most commonly used is porfimer sodium (Photofrin), which was introduced in the market more than a decade ago.[11] However, thus far, the only nanoformulation for PDT treatment already present in the market is Visudyne but it is intended for age-related macular degeneration. One of the major drawbacks of the photosensitizers is photosensitivity, which in the case of Photofrin can lasts even several weeks.

In both PTT and PDT, the wavelength of the light source is critical. The use of near-infrared light is highly desirable since it is safe in comparison with light in the UV range and possesses a longer penetration depth in comparison with light in Vis region [12]. The light source can reach the tumor site by flexible endoscopy under local anesthesia in the case of superficial endobronchial lesions [11] or can be inserted intratumorally, for example throw a needle, in the case of deep-seated tumors [13]. Among the different light-responsive nanomaterials, recent studies report the ability of carbon-based nanomaterials, as carbon nanotubes [14], [15], fullerene [16] and graphene [17] to boost the efficacy of PTT or PDT. However,

their application in nanomedicine faces some challenges related to their production such as the extreme reaction conditions, complex instruments, time consuming purification procedures, high costs of production, low batch-to-batch reproducibility. Moreover, pristine CNM tend to aggregate due to strong van der Waals interactions because of their hydrophobic properties. Therefore, they must be functionalized in order to be dispersed in aqueous media and to increase their biocompatibility.[18] This further reduce the yield of final product.

As previously mentioned, hydrothermal carbonization has been proposed as a green and sustainable route for production of carbon nanomaterials. Using this technique, we recently reported the synthesis of glucose-derived carbon nanoparticles (CNP) possessing the ability to generate ROS and heat upon NIR irradiation in cell-free tests [19], as described in details in chapter one. Here, we investigated the possible use of CNPs for the therapy of lung tumors by evaluating the effects of CNPs activated by NIR laser beam on human A549 lung adenocarcinoma cells.

Besides efficacy, one of the main obstacles for the translation of nanomaterials for biomedical applications from the laboratory to the market is their biopersistency. The latter is related to a possible accumulation in the body, which could lead to short and long term harmful effects. For this purpose, the investigation of the degradation of the CNP in vitro and in vivo is a crucial aspect of their safety, which, together with previous cytotoxicity studies included in the first chapter of this thesis, could pave the way to the medical application of these relatively new nanostructures.

In the last decade, several studies have evidenced the role and efficacy in the biodegradability of carbon nanotubes (CNTs) [20], fullerene [21] and graphene [22] of an oxidative human enzyme, myeloperoxidase (MPO), abundantly expressed in neutrophils. Different mechanisms of degradation have been proposed. In particular, the enzyme is able in the presence of hydrogen peroxide, to oxidase chloride ion and form hypochlorous acid [23]. HClO is a strong oxidant compound, which contributes to the biodegradation of CNM together with the reactive radical intermediates produced by the enzyme [20]. The ability to be

degraded represents an advantage for CNM by respect to other multifunctional biopersistent inorganic nanomaterials like gold.

In addition to the peroxidase-driven degradation of carbon nanomaterials, a few studies also support an alternative peroxynitrite-dependent degradation pathway mainly observed in activated macrophages [24], and chondrocytes [25]. In both reported studies, 1,3-morpholinosydnonimine (SIN-1) was employed in acellular evaluation of the degradation of CNM. SIN-1 is a chemical peroxynitrite donor compound, highly instable in aqueous media, which decomposes simultaneously producing nitrite oxide (NO) and superoxide ($O_2^{\cdot -}$) that react together to generate peroxynitrite.

Although the degradation of previously mentioned CNM has been well documented in the recent years, no data are present in the literature regarding the degradation of hydrothermal derived-CNP by the previously described mechanisms of degradation. Thus, herein, in the second part of this chapter the susceptibility to degradation of our CNP was reported, which was investigated in both cell-free systems and in the presence of freshly isolated primary neutrophils.

2.2 Materials and methods

2.2.1 Synthesis of carbon nanoparticles

Carbon nanoparticles were obtain by hydrothermal carbonization following a protocol previously described in chapter 1 for CNP4, without modifications, named in this chapter as CNP.

2.2.2 Sterilization of carbon nanoparticles

Nanoparticles suspension were introduce in an autoclave and sterilized at 121°C, for 30 min. One aliquot of CNP suspension was stored at 4°C and used as a control for comparison with the sterilized sample in terms of hydrodynamic diameter, zeta potential and pH. Samples were also subjected to thermogravimetric analysis, as a technique to detect changes in internal structure, i.e. graphitization, or modification in the surface, i.e. decarbossilation due to the high temperature during sterilization, using the protocol described in the paragraph 1.2.3.

Sterilization was further confirmed by the absence of bacterial contamination on the agar plate test based on a protocol developed by European Nanomedicine Characterization Laboratory (EUNCL) [26]. Nanoparticle samples and controls (ultrapure water in the case of negative control and E.coli MG1655, $5x10^2$ CFU/ml, in the case of positive control), were spreaded on the surface of agar and the growth of bacterial colonies was monitored after 72 h of incubation.

2.2.3 FTIR analysis

Attenuated total reflection (ATR) FTIR measurements were performed on a ThermoFisher Nicolet iS10 Instrument. Spectra were obtained from 16 scans with a resolution of 4 cm−1 in the spectral region of 650–4000 cm−1. CNP suspension was lyophilized overnight and aliquots were analyzed without prior preparation.

2.2.4 Evaluation of the efficacy of CNP

2.3.4.1 Cells

Human lung adenocarcinoma cells A549, provided by Istituto Zooprofilattico Sperimentale "Bruno Ubertini" (Brescia, Italy), were cultured in Ham's F12 (Life Technologies, Carlsbad, CA) supplemented with 10% v/v fetal bovine serum (FBS, Invitrogen Life Technologies) and 1% v/v penicillin-streptomycin.

2.3.4.2 Measurement of lactate dehydrogenase leakage

An aliquot of the CNP suspension was collected from the stock (1 mg/ml) after sonication bath for 30 minutes and transferred into a 2 ml tube; before incubation with cells, the suspension was sonicated again with a probe sonicator (Bandelin Sonopuls HD 3100) for 2 minutes using the pulsation mode at 40% of power.
The final suspension was then incubated with A549 cells at the desired concentration for 24 h and 48 h and the cytotoxicity of the nanoparticles was measured as the leakage of lactate dehydrogenase (LDH) activity into the extracellular medium, using a Synergy HT microplate reader (Bio-Tek Instruments, Winooski, VT), as previously described [27]. Positive control consisted in a sample of pyrogenic silica.

2.3.4.3 Uptake and Intracellular distribution

The cellular uptake and distribution of CNPs was qualitatively evaluated by TEM analysis. A549 cells were incubated for 24 h with 80 μg/ml of CNPs. At the end of exposure, cells were washed, detached and re-suspended in 2% Karnovsky solution. Samples were then treated for TEM analysis, as detailed elsewhere.[19]

2.3.4.4 Exposure of A549 to CNP and NIR irradiation

The stock suspension of CNP was sonicated as described in the previous paragraph. Then, the aliquot was sterilized using UV for 15 minutes. For the evaluation of the phototoxicity of CNP following NIR exposure, A549 cells have

been plated in 24 wells plates, $5x10^4$ cells/well in 0.5 ml of Ham's F12; after 24h the medium has been replaced with 0.5 ml phenol red-free RPMI, supplemented with 10% FBS, with or without CNPs with a final concentration of 80 µg/ml. After 24h the cells have been exposed to NIR irradiation, 945 nm, 3 W/cm^2, 15 min. The temperature has been monitored using a thermal imager. Stability of CNP was evaluated after 24h and 48h of incubation in phenol red-free RPMI, supplemented with 10% FBS, before the experiment, using dynamic light scattering, Zetasizer Nano, Malvern Instruments.

2.3.4.5 Crystal violet assay

After NIR irradiation, cells were continued to cultured overnight. Afterwards, medium was discarded and the cells were washed twice with PBS and then each well was incubated with 500µl of crystal violet-methanol solution for 20 minutes. Finally, the plates were washed with water and they were left to dry before image acquisition using a Leica DC100 microscope (Leica Microsystems GmbH, Wetzlar, Germany).

2.3.4.6 Western blot

Cells were rinsed with ice-cold lysis RIPA buffer (50 mM Tris, 10 mM EDTA, 1% v/v Triton-X100; pH 7.5), supplemented with the protease inhibitor cocktail set III (80 µM aprotinin, 5 mM bestatin, 1.5 mM leupeptin, 1 mM pepstatin; Calbiochem, San Diego, CA), 2 mM phenylmethylsulfonyl fluoride and 1 mM Na_3VO_4. The cells were then sonicated (Bandelin Sonopuls HD 3100) and centrifuged at 13,000 × g for 10 min at 4 °C. 10 µg protein extracts were subjected to 4-20% gradient SDS-PAGE and probed with the following antibodies: anti-tubuline (mouse; Santa Cruz), anti-HSP70 and anti-HSP90 (abcam, USA), The membranes were then incubated with peroxidase-conjugated secondary antibody (1:3000; Bio-Rad Laboratories) and washed with PBS-Tween 0.1% v/v solutions. Protein bands were detected by enhanced chemiluminescence (Bio-Rad Laboratories).

2.3.4.7 Immunofluorescence analysis

Firstly, 2×10^4 A549 cells were seeded onto glass coverslips in 24-well plates overnight. Cells were than exposed to CNP as described in the previous paragraph: Exposure of A549 to CNP. Sample were washed thrice with PBS and fixed using 4% w/v paraformaldehyde (PFA) for 15 min at room temperature, washed with PBS, incubated for 10 min with PBS-Triton X-100-0.1% v/v and then washed thrice with PBS. Samples were stored at 4°C until incubation with anti-gamma H2AX antibody (Abcam, diluted 1:100 in 1% FBS/PBS), overnight, at 4°C. PBS was used to wash the samples five times; samples were then incubated for 1 h at room temperature with an AlexaFluor488-conjugated secondary antibody (Abcam, diluted 1:100 in 1% FBS/PBS).

Cells were incubated with 4′,6-diamidino-2-phenylindole dihydrochloride (DAPI), diluted 1:10000 in PBS for 5 min, washed thrice with PBS. The cover slips were mounted with the Mounting media and examined with a Leica DC100 fluorescence microscope (Leica Microsystems GmbH, Wetzlar, Germany). All samples were analized in duplicates, with at least of 50 cells scored per sample.

2.3.5 Evaluation of the degradation of CNP

2.3.5.1 Degradation of CNP by NaClO

CNP were suspended in PBS, 10 mM, pH 4.5 to obtain a final concentration of 40 µg/ml and subsequently NaClO was added to the suspension at a final concentration of 200 µM. The sample was incubated at 37°C for 4 days. NaClO was added daily and samples were analyzed at day 0, 2 and 4 using UV-Vis spectroscopy and Raman spectroscopy.

2.3.5.2 Degradation of CNP by human myeloperoxidase

The nanoparticles were incubated in fluids containing hMPO coincubated or not with diluted H_2O_2 and NaCl, in order to investigate the propensity of degradation

over time based on the ability of the enzyme not only to produce reactive intermediates but also HClO.

Samples with a volume of 2 ml, containing 20 µg of hMPO and 80 µg of CNP suspended in an aqueous solution of NaCl (final concentration 140 mM) were incubated at 37°C for 4 days. Furthermore, a 8 ul of a solution of H_2O_2, 20 mM, was continuously added during incubation every hour (6 times a day). Additions of fresh hMPO solution was also performed every 6h (twice a day). Control samples were also prepared as following: CNP in NaCl, CNP in NaCl + H_2O_2, CNP in H_2O + H_2O_2 + hMPO. UV-Vis spectrometry and Raman spectroscopy were used for monitoring and documenting the degradation of the samples.

2.3.5.3 Degradation of CNP by peroxynitrite

CNP (final concentration 40 µg/ml) were incubated in 10 mM phosphate buffer (pH 7.4) with peroxynitrite ($ONOO^-$), at 37 °C. Peroxynitrite was produced by addition of peroxynitrite donor SIN-1 (final concentration 300 uM), as described by Kagan et al. 2014 for SWCNTs degradation study, which decomposes and produces both nitric oxide and superoxide. Aliquots of fresh SIN-1 were added every 1.5 h (5 times a day), for 4 days. UV-Vis spectrometry and Raman spectroscopy were used for monitoring and documenting the degradation of the samples.

2.3.5.4 Raman spectroscopic analysis of acellular samples

Raman spectra of the samples were recorded at day 0, 2, 4. Two milliliter of each sample was placed in quartz cuvettes and the suspensions were analyzed using the following parameters: 532nm laser, 10mW power, 1,5 s of exp time, 120 scans, cell for liquid sample, spectrograph aperture of 50 µm slit.

2.3.5.5 UV Vis spectroscopic analysis of acellular samples

UV-Vis spectra of the samples were recorded at day 0, 2, 4. Two milliliter of each sample was placed in quartz cuvettes, 10 mm path length, and the spectra were

registered using Evolution 60s, Thermo Scientific, wavelength range from 190-900 nm.

2.3.5.6 Evaluation of the degradation of CNP by neutrophils

Prior to the investigation of the possible degradation of carbon nanoparticles by professional phagocytic cells, cytotoxicity studies were performed by incubating the CNP with neutrophils freshly isolated from human blood of different donors in order to choose a safe nanoparticle concentration. Cytotoxicity assessment was performed also using primary human monocyte-derived macrophages (HMDM).

2.3.5.7 PMN isolation

Neutrophils were obtained from buffy coat of healthy human blood donors (Karolinska University Hospital, Stockholm, Sweden) using density gradient sedimentation. Briefly, 12.5 ml of Lymphoprep (Axis Shield, Oslo, Norway) were transferred in a 50 ml Falcon tube and 25 ml of diluted blood (1:1 in PBS 1x, pH 7.4, Gibco, at room temperature) were added slowly, without mixing. The Falcon tube has been subjected to centrifugation (Thermo Scientific, Megafuge 16R, Heraeus) for 30 min, 1500 rpm.

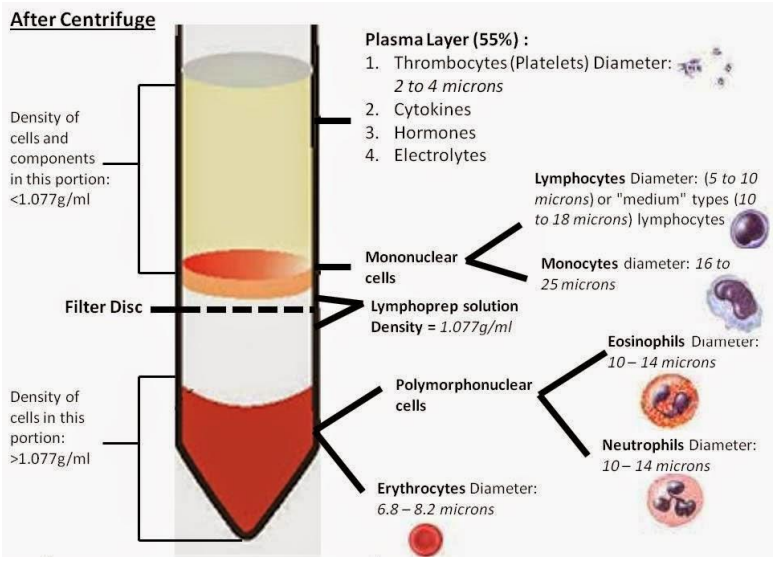

Figure 2.1. Schematic representation of density gradient sedimentation for the separation of blood components.(from http://textbookhaematology4medical-scientist.blogspot.com/2014/06/buffy-coatlayer-peripheral-blood.html)

Plasma was discarded after the centrifugation and PMN were collected in Falcon tubes. 30 ml of autoclaved 5% dextran was added to each falcon tube containing PMN phase, mixed and after 30 minutes, the upper pinkish layer was transferred into two new 50 ml Falcon tubes. 50 ml of pre-warmed PBS were added to each tube and centrifuged at 1200 rpm. After the centrifugation, the supernatant was discarded and the pellet was risuspended in 20 ml of PBS and subsequently 20 ml of H_2O. 2.7 % NaCl was than transferred in the falcon in order to obtain the hypotonic lysis of red blood cells. Centrifugation (5 min at 1200 rpm) was used to separate the PMN from the lysed red blood cells. The supernatant was discard and the pellet was resuspended in phenol red free RPMI 1640 medium + 2mM L-Glu + 100 U/ml penicillin + 100 mg/ml streptomycin (serum-free).

Isolation of primary human monocytes were also performed using the density centrifugation sedimentation as for PMN cells. The final pellet containing mononuclear blood cells was suspended in 4 ml of MACS buffer, prepared as following: 2.5 g BSA, 0.372 g EDTA, 500 ml of PBS, and filtered 0.22 µm. In order to separate the CD14+ monocytes, a suspension of CD 14BEDS (MACS

Miltenyi Biotech), 200 µl, were added to the cell suspension. The mix has been stored in the fridge for 1 h and finally it was diluted with MACS buffer and centrifuged at 1200 for 5 min. The monocytes were isolated using a magnetic column (LS column, MACS Miltenyi Biotec). After the centrifugation, the supernatant was discarded and the pellet was risuspend in 2 ml of MACS buffer. The cell suspension was transfer into the column. The total effluent is composed by unlabeled cell fraction while CD14+ monocytes are attached to the magnetic column. The magnetic part was removed and the cells were collected in a test tube. The cells were washed once by centrifugation and 10 µl of M-CSF was added for cell differentiation, in order to obtain human monocyte-derived macrophages.

2.3.5.8 CNP stability in cell media

The stability of the nanoparticles was monitored in cell media by means of dynamic light scattering and electrophoretic light scattering. Nanoparticles were suspended in RPMI +/- FBS at the desired concentrations and stability was evaluated at time 0, 3 and 6 h to mimics the conditions of the toxicity test toward neutrophils. In the case of macrophages studies, the stability was studied in RPMI supplemented with 10 % FBS after 24h of incubation.

2.3.5.9 Citotoxicity assessment

Cells were cultured in 96 well microplate in RPMI supplemented with 1% penicillin-streptomycin and with or without 10% fetal bovine serum, then incubated in the same fresh cell culture medium for the required time (3h and 6h for neutrophils and 24 h for macrophages), in the absence or presence of CNPs. In all the experiments, 50.000 cells were placed in each well.

Alamar blue assay (Invitrogen) was used to investigate cells viability after incubation with CNP. The assay is based in the reduction of the cell-permeable compound resazurin (blue and non-fluorescent reagent) to resorufin (red and

highly fluorescent) in living cell and this reaction is quantitatively related to viability. Alamar reagent was added to each well obtaining a final concentration of 10% v/v and the samples were incubated in a humidified 5%CO_2 incubator, for 3 h at 37°C. Fluorescence of the samples was recorded using 560 nm and 590 nm as excitation and emission wavelength, respectively, using a Tecan Infinite F200 plate reader.

2.3.5.10 Biodegradation of CNP by PMN

Degradation of CNP in the presence of neutrophils was assessed based on previous studies reporting the degradation of carbon-based nanomaterials [22] and preformed at Karolinska Instutute by Sandeep Keshavan. Briefly, freshly isolated polymorphonuclear neutrophils were incubated were incubated with CNP at a final concentration of 20 µg/ml in the presence of N-formylmethionine-leucyl-phenylalanine fMLP (10 nM) and cytochalasin B (5 µg/ml), to induce degranulation for 6 h, in the presence or absence of myeloperoxidase inhibitor-1 (MPO-1). The samples were then collected and stored at -80°C until subjected to Raman spectroscopic analysis.

2.3.5.11 Raman spectroscopic analysis of cellular samples

Samples from time zero and after 6h of incubation were analyzed at INRiM - Istituto Nazionale di Ricerca Metrologica, Turin, Italy, by Dr. Andrea Giovannozzi. 5 µl of each sample suspension were drop-casted into quartz supports. Raman measurements were carried out using the Thermo Scientific DXR Raman confocal microscope system equipped with an excitation laser source of 532 nm. A low laser power of 2 mW was employed in order to avoid possible damage of the samples, a 20x long working distance microscope objective, a 50 µm pinhole aperture. Each spectrum of the map was registered with 1 s integration time and 70 scans.

2.3 Results and discussion

2.3.1 Synthesis, sterilization and characterization of CNP

CNP were synthesized starting from glucose, by hydrothermal carbonization route, using the protocol described in details in chapter 1. Hydrodynamic diameter and zeta potential of the obtained batch was determined in order to confirm that they were in accordance with previously obtained nanoparticles. Bacterial contamination can interfere with the outcome of in vitro preclinical tests. For this reason, CNP were sterilizes by steam autoclaving. Sterilized CNP were compared to pristine CNP in order to reveal possible modification of their properties. In both cases, CNP resulted negatively charged, monodispersed with d_H distribution in nanosize range, as shown in figure 2.2 (a and b). No significant alterations of these characteristics were detected.

A

Sample	ζ potential (mV)	pH
ctrl	-46,4 ± 1,33	4,6
Sterilized CNP	-47,3 ± 1,41	4,5

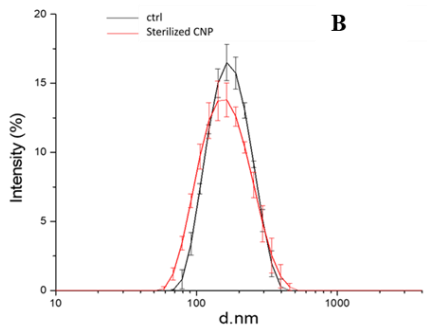

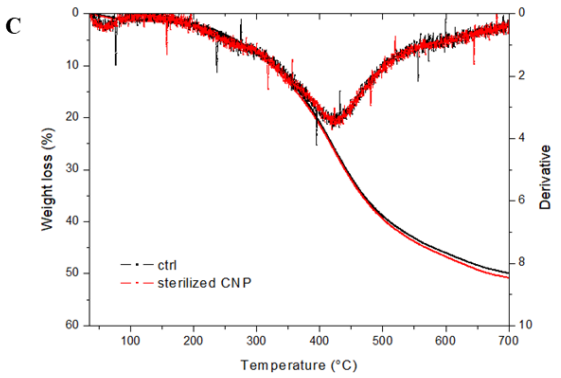

Figure 2.2. Effect of sterilization on CNP properties. A) zeta potential and pH data, B) intensity-based size distribution, c) thermogravimetric analysis: % of weight loss recorded under N_2.

Results from the thermogravimetric analysis of the samples are displayed in figure 2.2c. The thermograms are perfectly superimposable showing that the CNPs subjected to sterilization have not undergone changes to their internal structure. Agar plate test, used for the investigation of the bacterial contamination in the sterilized sample, confirm that steam autoclaving allowed obtaining of samples without bacterial contamination after 72 h of incubation, as shown in figure 2.3.

In summary, the sterilization of CNP using the cheap steam autoclaving method is a suitable procedure that ensure stability of the physicochemical characteristics of the particles.

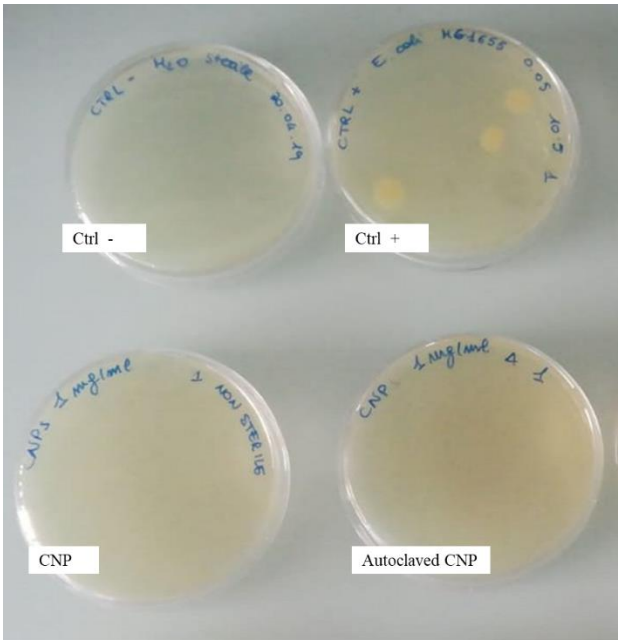

Figure 2.3. Detection of Bacterial Contamination by Agar Plate Test. Control samples consisted of: ctrl – (autoclaved water), ctrl + (E. Coli MG1655), non sterilized CNP. All the samples were incubated for 72 h, at 37°C.

FTIR analysis were performed as an additional tool for the characterization of the surface of CNP. FTIR spectrum showed in figure 2.4. Data evidenced a strong and large band at 3500-3250 cm^{-1} corresponding to O-H hydroxyl or carboxyl stretching vibration [28] and a strong band at 1700 cm^{-1} which is related to the stretching vibration of C=O carbonyl or carboxyl group [29]. Results are in

accordance with the previously reported data (paragraph 1.3.2) of the presence of abundant carboxylic groups at the surface of CNP.

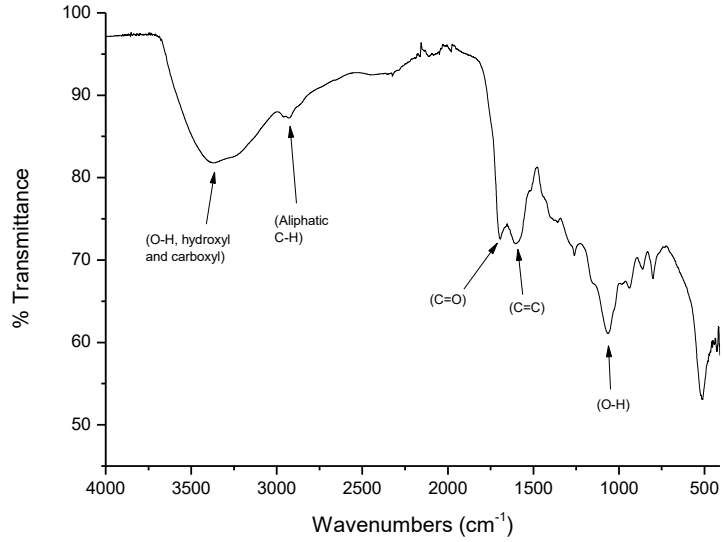

Figure 2.4. ATR-FTIR spectrum of CNP

2.3.2 Cytotoxicity in dark conditions toward lung epithelial cell (A549) and uptake

CNP were firstly tested for their toxicity in absence of NIR activation, by evaluating the cell membrane integrity of A549 after incubation with CNP, measured as leakage of intracellular LDH into the extracellular medium. A549 cells were incubated for 24 h with NPs at a concentration range of 10-320 µg/ml. A sample of pyrogenic silica was used as positive control. Results evidenced that CNP do not elicit any cytotoxic effect on tumor epithelial cells in dark condition in a wide range of concentrations, as shown in figure 2.5.

TEM analysis was performed on A549 cells incubated in the absence or presence of CNP. Two different concentrations were tested, 80 and 160 µg/ml. Cells were exposed to CNP for 24h in absence of NIR irradiation and images are shown in figure 2.6

Unexposed cells (negative control) showed normal morphology of A549 cells, without specific ultrastructure alterations. Nuclei are well defined and the organelles visible. Cells exposed to CNP show groups of single particles inside endo/phagocytosis organelles (endosomes), high in number in the case of the highest concentration of CNP. No cellular alternation are present in the case of A549 exposed to 80 or 160 µg/ml of CNP.

Based on these results, a concentration of 80 µg/ml of CNP has been chosen for the assessment of the NIR-activated PD/PT activity.

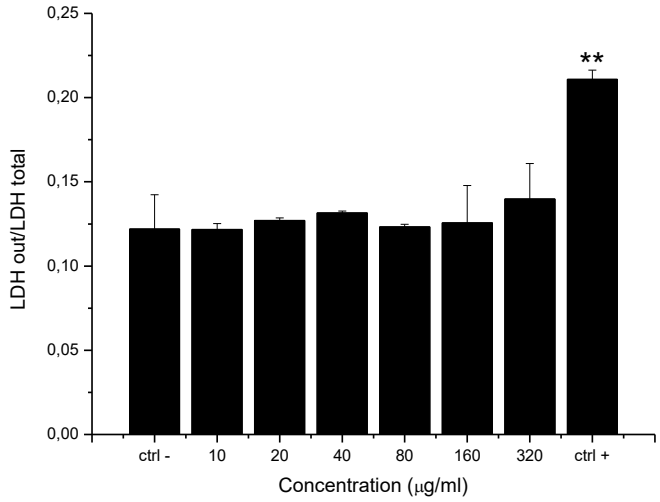

Figure 2.5. Cytotoxicity of CNP toward A549 without NIR irradiation. LDH assay results following exposure to CNP for 24h. Negative control corresponds to A549 no exposed to CNP and positive control refers to a pyrogenic silica nanoparticles. ** $p<0,01$ vs control.

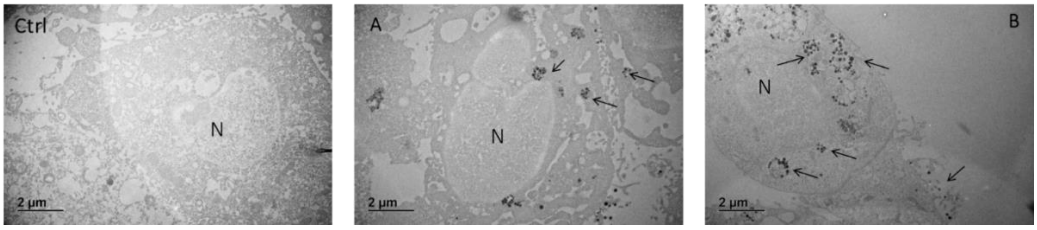

Figure 2.6. Uptake of CNP by A549 cells after 24 h of incubation. The arrow point to internalized CNP; (N) nucleus. Ctrl (unexposed cells); A (80 µg/ml); B (160 µg/ml).

2.3.3 Effect of NIR-activated CNP on cell viability of A549 cells

We previously demonstrated that CNPs are able to produce singlet oxygen and warm up when irradiated with NIR in vitro [19]. Here we investigated whether these properties can be exploited to kill tumor cells.

CNP were activated using a laser diode emitting at a wavelength of 945 nm and at a power density of $3W/cm^2$, in continuous way. These experiments were conducted on A549 cells at doses in which non-activated CNPs had no toxic effects (80 µg/ml). The effect of CNP was compared with that of the NIR radiation only, to exclude a direct toxic effect of the irradiation.

Viability was monitored by assessing the morphology of cells after crystal violet staining using optical microscopy. Moreover, during the irradiation, the temperature in each well was recorded using a thermal camera.

The exposure at the laser beam with a potency of $3W/cm^2$ did not decrease the viability of cells in the absence of CNP for up to 15 minutes of irradiation. We therefore choose this parameters to test the phototoxicity of CNP toward A549 following irradiation.

The effect of CNPs at the dose of 80µg/ml activated by $3W/cm^2$ laser beam on A549 morphology is shown in figure 2.7. In the presence CNPs, a drastic cell death was observed, as inferred by obvious changes in cell morphology: most of the cells lost their normal spindle-shape and appeared rounded and smaller.

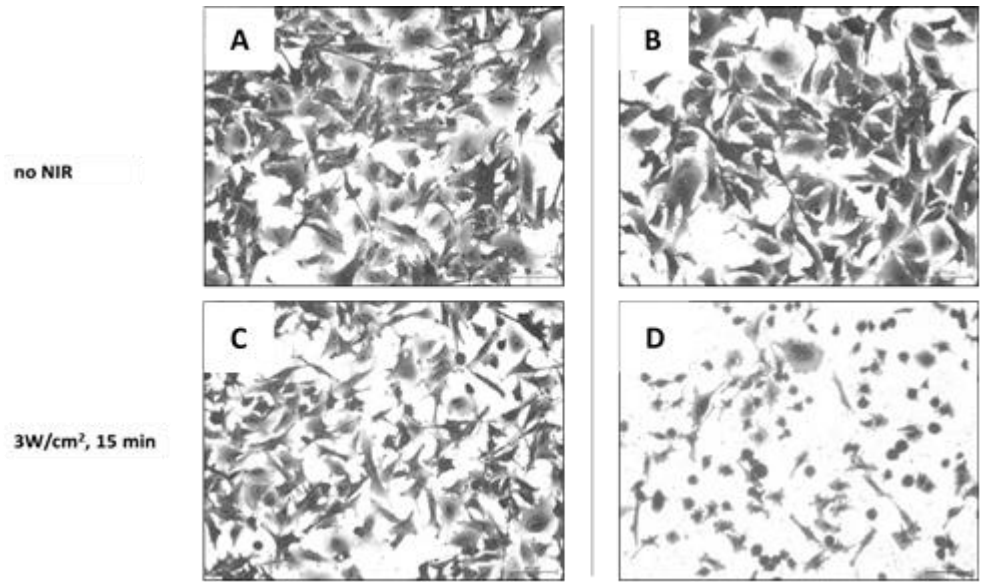

Figure 2.7. Effect of NIR-activated CNP on A549 cells morphology. Cells were not irradiated a) or irradiated with a NIR laser, irradiance 3W/cm^2, for 15 min c). Cells were exposed to CNP in absence b) or following NIR laser irradiation, irradiance 3W/cm^2, for 15min d).

A slight but significant increase of temperature was detected in NIR-irradiated cells in the presence of CNPs by respect of the laser beam only (Figure 2.8). In absence of CNP, a slight increase of temperature was observed, without effecting cellular morphology.

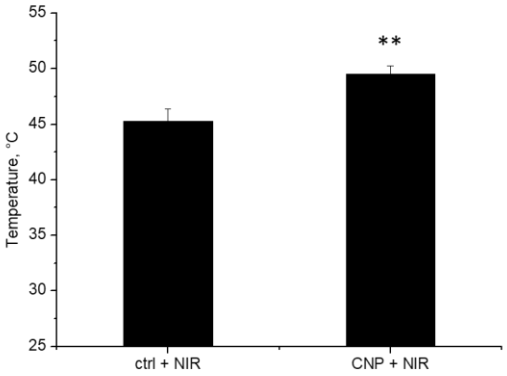

Figure 2.8. Temperature after NIR irradiation for 15 min, at 3W/cm^2 irradiance. A549 cells were irradiated in the absence (ctrl) or in the presence (CNPs) of 80μg/ml CNPs. **p<0.01

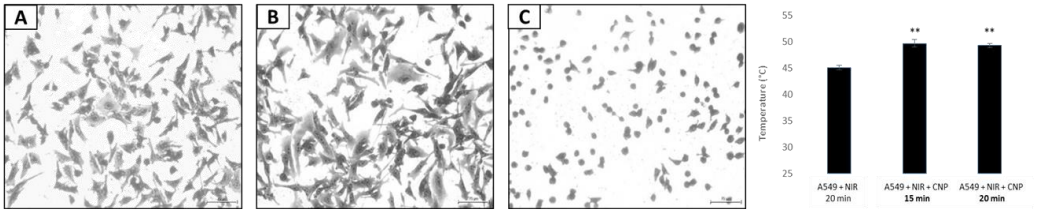

Figure 2.9 Effect of NIR-activated CNP on A549 cells morphology. Cells were irradiated with a NIR laser, irradiance 3W/cm^2, for 20 min a) or exposed to CNP and irradiated with a NIR laser, irradiance 3W/cm^2, for 10 b) or 20 min c). Temperature of the samples following irradiation. **p<0.01 vs. A549 + NIR 20 min.

Finally, we tried different exposure times in order to investigate the effect on cells, keeping constant the other parameters of CNP concentration and light source irradiance. As shown in figure 2.9b, no change in morphology of the cells were observed after 10 min of irradiation. Moreover, a substantial cell death was detected after 20 min, higher compared with what shown in figure 2.7d for cells exposed to NIR-activated CNP for 15 min. Cell death could be related to increase in temperature, but also generation of singlet oxygen, since we reported the ability

of CNP to induce both effects following NIR irradiation (paragraph 1.3.3). However, by monitoring the temperature after 10 min and after 20 min of NIR irradiation, no significant differences were found in cells exposed to CNP, suggesting that cell death probably occurs due to singlet oxygen production when cells are exposed to a CNP concentration equal to 80 μg/ml.

To further confirm that the cytotoxic effect observed was due to the PD/PT activity of carbon nanoparticles the expression of heat shock proteins and the occurrence of DNA damage monitored by activation of γ-H2AX histone were determined.

2.3.4 Heat shock proteins expression

Heat shock proteins (HSP) overproduction is a typical cell-survival mechanisms involved in response to PTT [30] and PDT [31], [32]. HSP could confer to cancer cells resistance toward physical stresses. Moreover, high HSP expression (HSP70, HSP27) not only help treated cells to handle heat and ROS damage such as unfolded or irreversibly oxidized proteins, but also promote cancer by preventing program cell death. On the other hand, when released by tumor cells or bounded at the cell membrane, HSP, especially HSP70, are able to promote anti-tumor immunity. [33]

Western blot analysis was performed to evaluate the expression of heat shock proteins in cells exposed to CNP 80 μg/ml, in absence or following NIR irradiation, for 15 min, at 3 w/cm^2 (figure 2.10). In panel B the amount of HSP70 and HSP90, normalized for all samples by using tubulin, are reported. The increase of both HSP70 and HSP90 expression were observed, albeit the values were significant only for HSP70 in cell treated with NIR-activated CNP. This trend well correlates with the observed cell morphology alterations and temperature increase following NIR/CNP co-exposure.

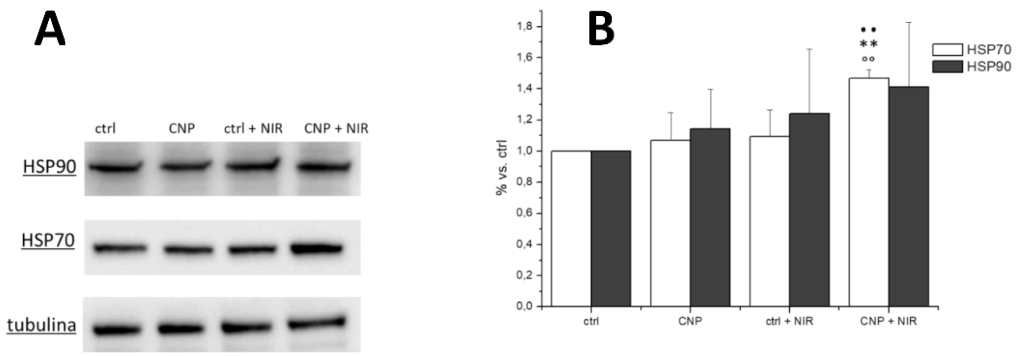

Figure 2.10. A) Western blot analysis of the heat shock proteins in A549 cells after treatment with or without CNP, following or not NIR irradiation. B) Bar graph showing quantification of HSP70 and HSP90 in all samples expressed as % vs. ctrl. Tubulin was used as a loading control.

** $p<0.01$ vs. ctrl; °° $p<0.01$ vs. CNP; $p<0.01$ vs. ctrl + NIR.

2.3.5 Activation of γ-H2AX histone as sensitive indicator of DNA damage

The formation of DNA damage marker, γ-H2AX, was detected after exposure of A549 cells to CNP following NIR irradiation in order to assess the *in vitro* therapeutic efficacy of CNP as phototoxic agents toward tumor cell. γ-H2AX histone activation occurs by phosphorylation on SER-139 residue, and it is a sensitive marker of DNA lesions, known to mark sites of double stand breaks.[34] Images of the samples are shown in figure 2.11, were cell nuclei are marked in blue and γ-H2AX foci corresponds to green spots.

Results evidence that in absence of laser irradiation, untreated cells or cells exposed to CNP exhibit no DNA damage confirming the lack of toxicity of CNP in dark conditions. In contrast, gamma-H2AX foci were observed in the NIR-treated group. However, the phosphorylation level when cells were exposed to both CNP and NIR is dramatically higher and all cells are affected, in comparison with the irradiated cells non exposed to CNP, where number of foci is drastically

lower and not all cells are involved in γ-H2AX activation. The results suggest that NIR-induced phototoxicity of CNP enhance the DNA damage, which could be correlated with ROS-induced stress.

If DNA is completely repaired, γ-H2AX foci are disassembled and H2AX is dephosphorylated.[35] Otherwise, 24h-post treatment unresolved γ-H2AX foci in tumor cells, as in this experiment, is linked with lethal DNA damage and cell death [36].

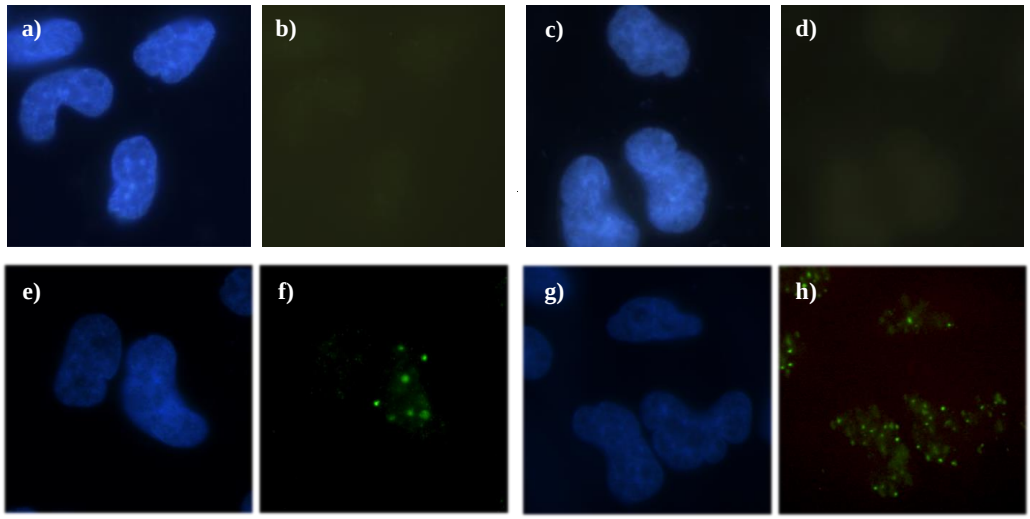

Figure 2.11. Representative microscopy images from γ-H2AX immunofluorescent staining performed 24h post-treatment. Images corrispondes to: A549 cells non irradiated a), A549 irradiated with NIR laser b), A549 cells exposed to CNP non irradiated c) and A549 cells exposed to CNP irradiated with NIR laser d). γ-H2AX staining is green, while nuclei are stained with DAPI blue.

Overall, the results demonstrate the ability of CNP to induce cell death only when activated by NIR light, making them suitable for cancer therapy. The mechanism of action appears related the PT activity, confirming what previously reported [37]. However, the pronounced cytotoxic effect observed in the absence of a significant increase of temperature (figure 2.9c) suggest that CNP act also by generating singlet oxygen, making them promising agents for dual PT/ PD therapy. One of the major limitations of PD therapy is due to the low generation

of singlet oxygen due to severe hypoxia related to oxygen consumption in the tumor mass [38]. The coexistence of a PT effect might have a synergic effect thus increasing the efficacy of the material.

2.3.6 Cell-free degradation of CNP by endogenous oxidants

Several oxidants like hydrogen peroxide,[39], hydroxyl radicals [40], peroxynitrite [24] and hypochlorous ions [41] were found able to oxidize and degrade CNMs at different extent. The present study aimed at getting insight into the biodegradability of a new class of CNMs, saccharide-derived carbon nanoparticles (CNP). In fact, no information on their biodegradability are available so far.

Firstly, we performed preliminary experiments incubating the CNP with hydrogen peroxide, commonly found in lysosomes, at physiological concentrations, and find that CNP showed resistence to degradation. Furthermore, the susceptibility toward two additional endogenous oxidants (NaClO and peroxynitrite) and of hMPO was investigated and reported in this chapter. To monitor the degradation UV-Vis spectroscopy was firstly employed. In figure 2.12 are shown the UV–Vis spectra and the aspect of the suspension for all tested conditions: degradation in NaClO, degradation due to hMPO and degradation due to SIN-1. A dramatic decrease of UV-vis adsorption was observed for CNP treated with NaClO confirming the degradation of the nanomaterial. A similar effect was also observed for hMPO and SIN-1 degradation tests, although the slight decrease in absorbance of the CNP in SIN-1 test suggest a minor degradation of CNP occurred, also in accordance this the changes of the colours of the different suspensions. In the case of hMPO test, the presence of the NaCl and H_2O_2 simultaneously was essential for the degradation of CNP, suggesting that the degradation could be a result of the hypochlorous acid catalyzed by the enzyme.

a)

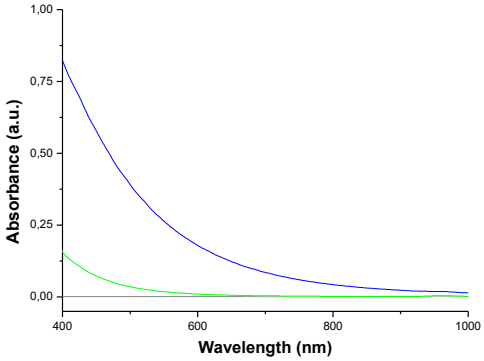

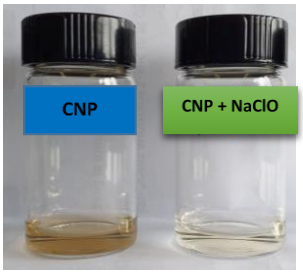

b)

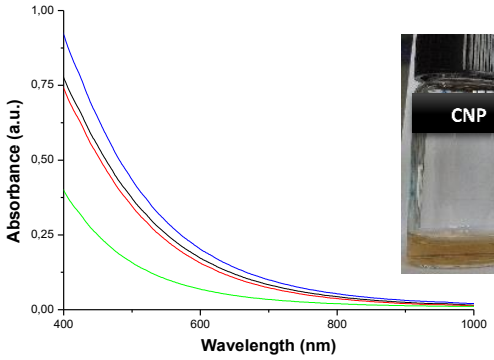

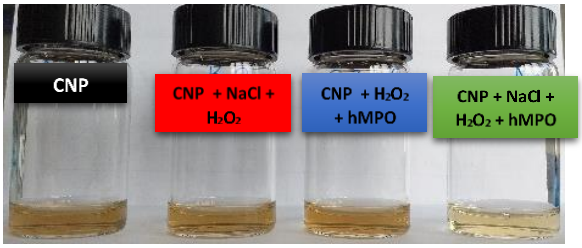

c)

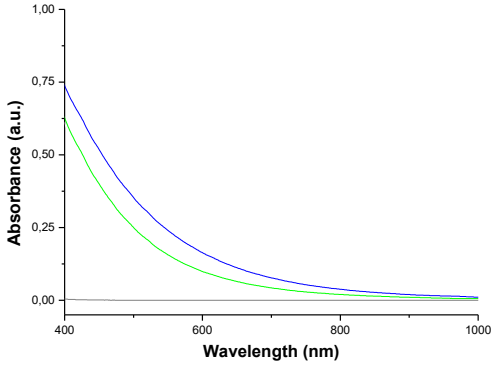

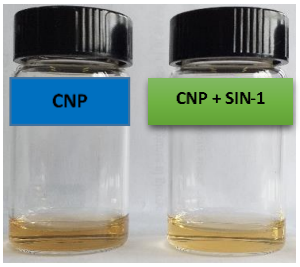

Figure 2.12. Degradation of CNP in presence of diluted NaClO (200 µM), hMPO or SIN-1.

Raman spectroscopy was used to confirm the CNP degradation. Spectra were registered at day 1, 3 and 5 and displayed in figure 2.13. An evident decrease in the intensity the two characteristics bands D and G was observed following incubation, which could be related to a partial degradation of the sample, in accordance with previously UV-Vis data. As for the latter, the NaClO system resulted to be the most efficacious.

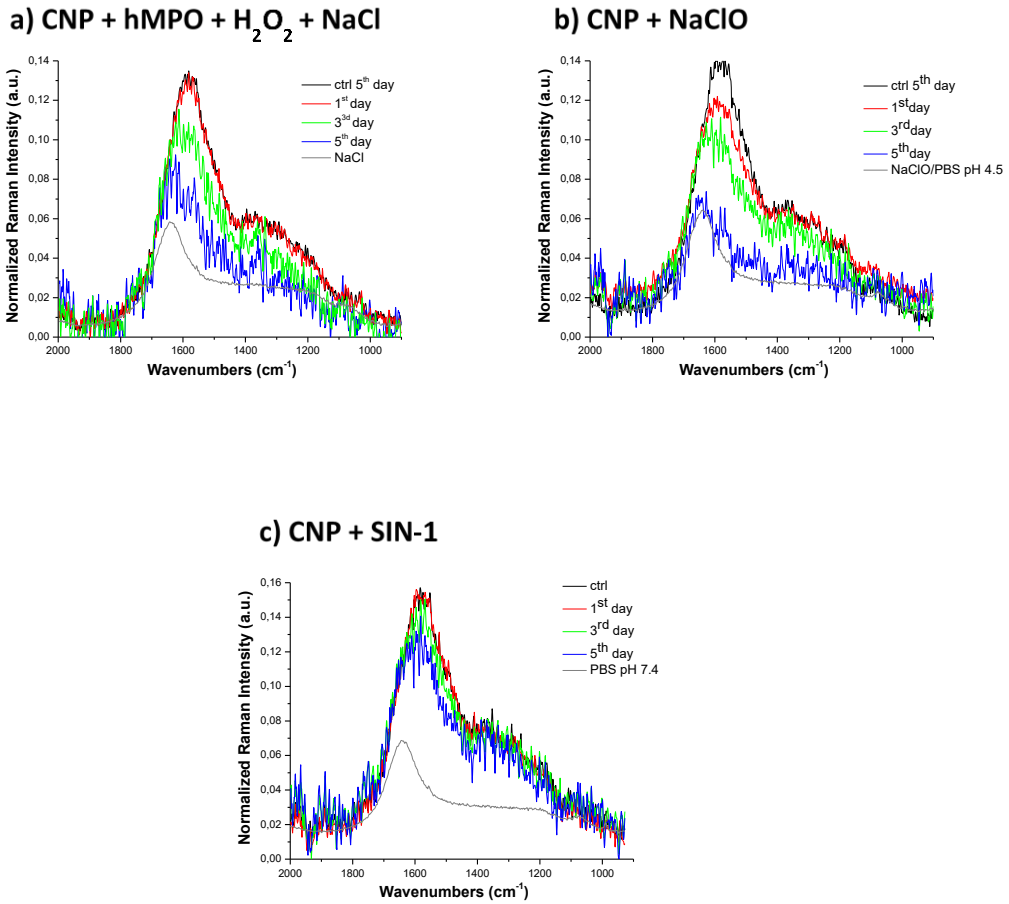

Figure 2.13. Raman spectra of the samples: a) NaClO, b) hMPO, c) SIN-1 incubated with CNP at day 1, 3 and 5. An aqueous CNP suspension was used as control (ctrl).

2.3.6 In vitro cellular degradation study

Cell-free degradation tests suggest that CNP could be possibly degraded in vitro by myeloperoxidase, the oxidative enzyme mainly secreted by neutrophils. In the following paragraphs, the cellular in vitro studies were summarized; preliminary studies of the behavior of CNP in cellular culture media and cytotoxicity toward blood were performed in order to choose safe conditions for the investigation of the degradation.

2.3.6.1 Stability of CNP in cell culture media

Evaluation of the stability in cell medium of CNP by dynamic light scattering (DLS) and electrophoretic light scattering (ELS) was performed in order to study if nanoparticles aggregate after incubation in cell medium RPMI supplemented or not with FBS. Different incubation time were applied 0h, 3h, 6h in accordance with the incubation time during cytotoxic studies toward neutrophils, and 24h for macrophages. Two CNP concentrations were tested: 10 and 80 µg/ml. DLS data (Figure 2.14) demonstrate that nanoparticles exhibit good stability over time as the mean hydrodynamic diameter do not change significantly up to 24 h.

In addition, zeta potential was also studied as an indirect measure of surface charge. The results evidenced a decrease in zeta potential in media supplemented with FBS suggesting that proteins presents in FBS may be absorbed at the surface of the CNP, which could lead to the formation of a protein corona.

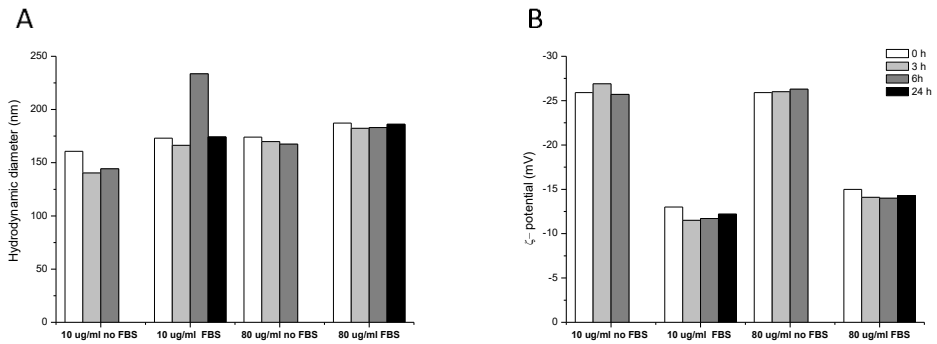

Figure 2.14. Evaluation of the stability in cell culture medium of CNP by dynamic light scattering A) and electrophoretic light scattering B). Incubation times corresponds to PMN (0, 3 and 6 h) and HMDM (24 h) cytotoxicity tests setup.

2.3.6.2 Citotoxicity toward PMN

CNP were firstly tested for their cytotoxicity toward human neutrophils derived from two different healthy donors. Cytotoxicity was monitored by the Alamar blue assay up to the concentration of 160 µg/ml. The material was dispersed in the media with or without FBS. The toxicity was investigated for two incubation time points: 3h and 6 h. CNP exhibit good toxicity profile for concentrations up to 40 µg/ml. Cell viability decreases for higher concentrations and is more pronounced in the case of cells cultured in medium without FBS, suggesting a protective effect of the protein corona.

Cytotoxicity studies involved also human-derived macrophages. In this case, CNP exhibit excellent biocompatibility for all the doses up to 160 µg/ml, following exposure for 24h. Results are summarized in figure 2.15.

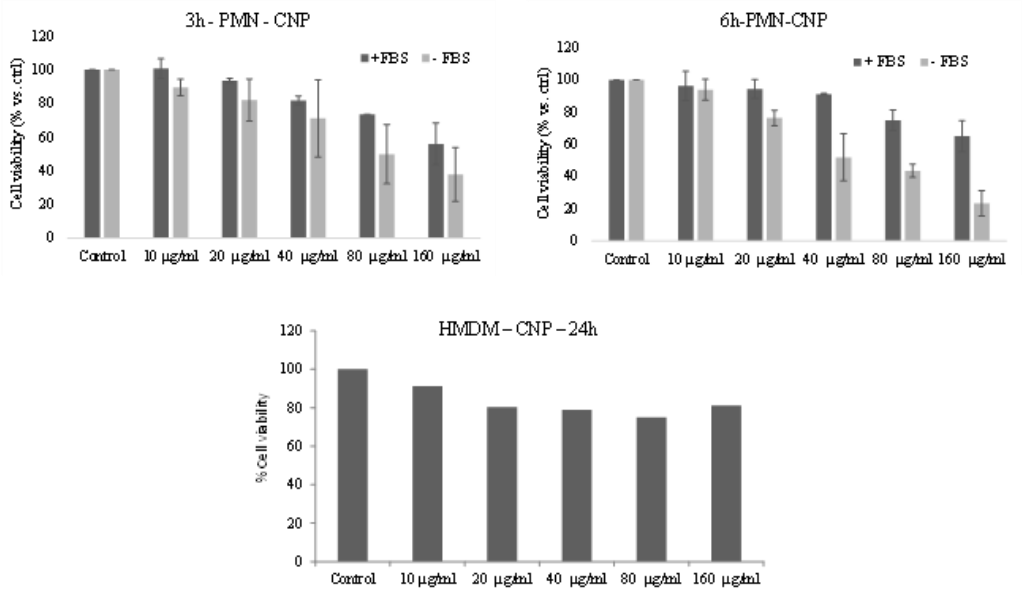

Figure 2.15. Cytotoxicity study of CNP toward primary human blood cells.

2.3.6.3 Biodegradation of CNP by PMN

Experiments regarding the degradation of CNP by neutrophils were based on what previously described for graphene oxide [22]. It is important to note that there are no studies to dato to report the of CNP by PMN. Cells cultured in RPMI with FBS and incubated with CNP at a safe concentration of 20 µg/ml for up to 6 h, in the presence of neutrophils activators, coincubated or not with MPO-1. Samples were analyzed using Raman spectroscopy. Raman spectra are collected and summarize in figure 2.16. Preliminary results shown in figure 2.16A evidence the decrease in the intensity of both G and D bands after 6 h of incubation in the absence of MPO-1, while no reduction of the intensity was observed in the samples where MPO-1 was present. These findings suggest that CNP could be degradated by PMN and the degradation is MPO-dependent, thus confirming the data obtained by cell-free experiements and in accordance with previous finding on degradability of graphene oxide [22]. However, additional test are on going involving the incubation of CNP with PMN for more extended time, up to 5 days.

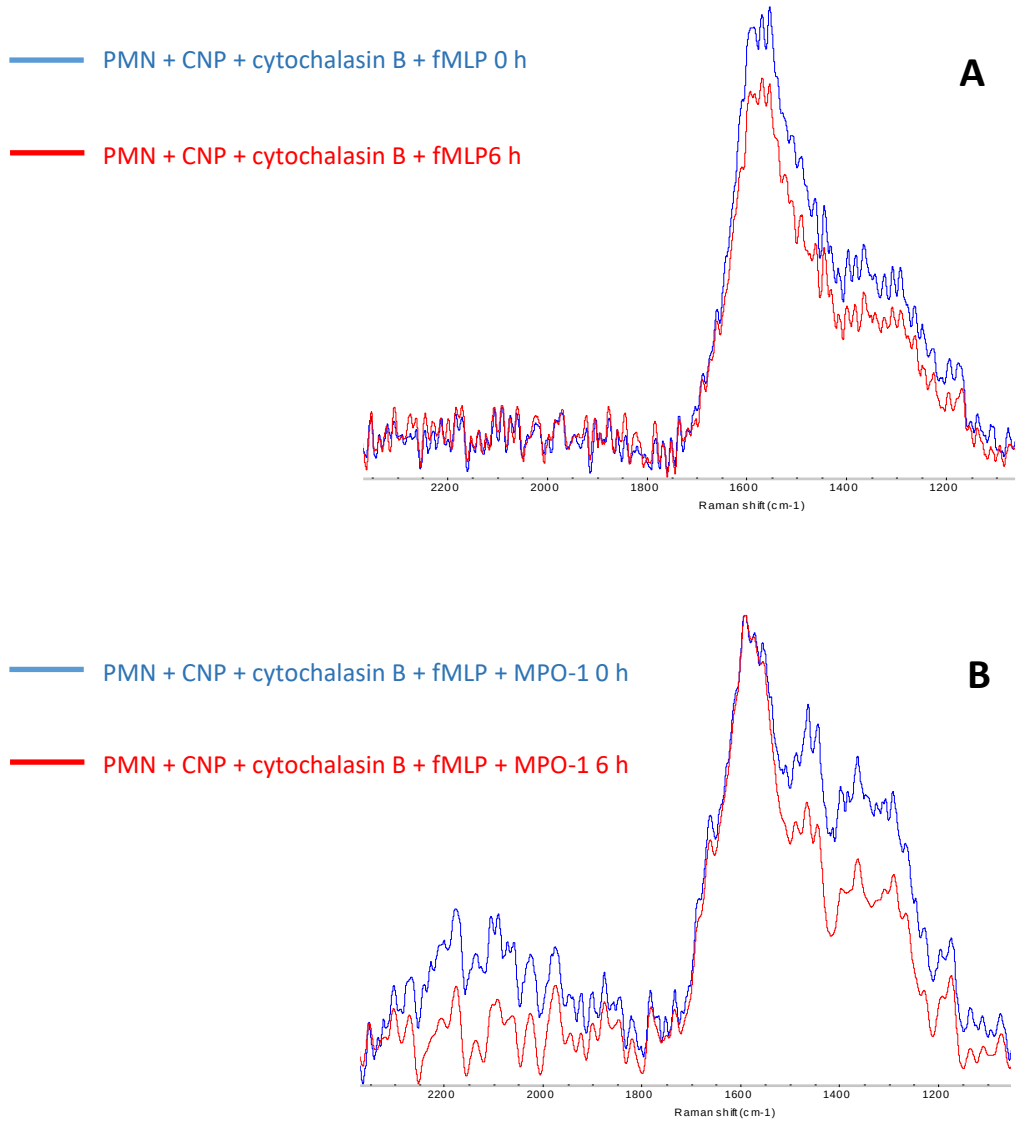

Figure 2.16. Neutrophil degradation of CNP activated by CB and fMLP, in the presence A) or absence B) of MPO-1.

2.4 Conclusions

To summarize, this study explores the efficacy against tumor cells and biodegradability of CNP. Clear NIR-induced photo-toxicity toward lung tumor cells was observed, likely related to both PT and PD activity. These results make CNP promising candidates for the design of nanoplatforms having a dual therapeutic modality, i.e. PT and PD activity. In addition, when non activated by NIR light CNP exhibit an excellent safety profile toward the lung epithelial cell line A549, and blood cells, i.e. primary neutrophils and monocyte-derived human macrophages. Finally, CNP appear susceptible to biodegradation by the immune-component enzyme hMPO, that was confirmed in ex vivo e, which might avoid bioaccumulation following parenteral administration.

These promising results represent a first step toward the possible clinical translation of these saccharose-derived nanoparticles. I*n vivo* studies are needed in order to confirm the present findings.

2.5 References

[1] WHO's annual World Health Statistics, overview, 2019, https://apps.who.int/iris/bitstream/handle/10665/311696/WHO-DAD-2019.1-eng.pdf

[2] J. Didkowska, U. Wojciechowska, M. Mańczuk, J. Łobaszewski, Lung cancer epidemiology: contemporary and future challenges worldwide, Ann Transl Med. 8 (2016) 150

[3] T. Lu, X. Yang, Y. Huang, M. Zhao, M. Li, K. Ma, J. Yin, C. Zhan, Q. Wang, Trends in the incidence, treatment, and survival of patients with lung cancer in the last four decades, Cancer Manag Res. 11 (2019) 943

[4] L. Lang-Lazdunski, Surgery for nonsmall cell lung cancer, Eur Respir Rev. 22 (2013) 382-404

[5] R. Mendes, P. Pedrosa, J. C. Lima, A. R. Fernandes, P. V. Baptista, Photothermal enhancement of chemotherapy in breast cancer by visible irradiation of Gold Nanoparticles, Sci Rep. 7 (2017) 10872

[6] J. Nam, S. Son, L. J. Ochyl, R. Kuai, A. Schwendeman, J. J. Moon, Chemo-photothermal therapy combination elicits anti-tumor immunity against advanced metastatic cancer, Nat. Commun 9 (2018) 1074

[7] D. van Straten, V. Mashayekhi, H. S. de Bruijn, S. Oliveira, D.J. Robinson, Oncologic Photodynamic Therapy: Basic Principles, Current Clinical Status and Future Directions, Cancers 2017 (9) 19

[8] D. C Doughty, A.R. Hoover, E. Layton, C. K. Murray, E. W. Howard, W.R. Chen, Nanomaterial Applications in Photothermal Therapy for Cancer, Materials, 12 (2019) 779

[9] M. O. Durymanov, A. A. Rosenkranz, A. S. Sobolev, Current Approaches for Improving Intratumoral Accumulation and Distribution of Nanomedicines, Theranostics 5 (2015) 1007-1020

[10] S. Yano, M. Naemura, A. Toshimitsu, M. Akiyama, A. Ikeda, J. Kikuchi, X. Shen, Q. Duan, A. Narumi, M. Inoue, K. Ohkubo, Sh. Fukuzumi, Efficient singlet oxygen generation from sugar pendant C60 derivatives for photodynamic therapy, Chem. Commun. 51 (2015) 16605-16608

[11] G. Shafirstein, A. Battoo, K. Harris, H. Baumann, S. O. Gollnick, J. Lindenmann, C. E. Nwogu, Photodynamic Therapy of Non–Small Cell Lung Cancer. Narrative Review and Future Directions, Ann Am Thorac Soc. 13 (2016) 265–275

[12] P. Zhang, C. Hu, W. Ran, J. Meng, Q. Yin, Y. Li, Recent progress in light-triggered nanotheranostics for cancer treatment, Theranostics 6 (2016) 948–968

[13] R. Gassino, Development of a fiber optic probe for tumor laser ablation with integrated temperature measurement capabilities, Doctoral thesis, 2019

[14] F. Zhou, Z. Ou, B. Wu, D. E. Resasco, W. R. Chen, Cancer photothermal therapy in the near-infrared region by using single-walled carbon nanotubes. J. Biomed. Opt. 14 (2018)

[15] J. T. Robinson, R. Luong, H. Dai, High Performance In Vivo Near-IR (>1 μm) Imaging and Photothermal Cancer Therapy with Carbon Nanotubes. Nano Res. 3 (2011) 779–793

[16] Y. Yamakoshi, N. Umezawa, A. Ryu, K. Arakane, N. Miyata, Y. Goda, T. Masumizu, T. Nagano, Active oxygen species generated from photoexcited fullerene (C60) as potential medicines: O2−• versus 1O2, J. Am. Chem. Soc. 125 (2003) 12803−12809

[17] K. Yang, S. A. Zhang, G. X. Zhang, X. M. Sun, S. T. Lee, Z. A. Liu, Graphene in Mice: Ultrahigh In Vivo Tumor Uptake and Efficient Photothermal Therapy. Nano Lett. 10 (2010) 3318−3323

[18] J. Bardhan, 30 years of advances in functionalization of carbon nanomaterials for biomedical applications: a practical review, Mater. Res. 32 (2017) 107-127

[19] I. Kokalari, R. Gassino, A. M. Giovannozzi, L. Croin, E. Gazzano, E. Bergamaschi, A. M. Rossi, G. Perrone, C. Riganti, J. Ponti, I. Fenoglio, Pro- and anti-oxidant properties of near-infrared (NIR) light responsive carbon nanoparticles, Free Radic Biol Med. 134 (2019) 165-176

[20] V. E. Kagan, N. V. Konduru, W. Feng, B. L. Allen, J. Conroy, Y. Volkov, I. I. Vlasova, N. A. Belikova, N. Yanamala, A. Kapralov, Y. Y. Tyurina, J. Shi, E. R. Kisin, A. R. Murray, J. Franks, D. Stolz, P. Gou, J. Klein-Seetharaman, B. Fadeel, A. Star, A. A. Shvedova, Carbon nanotubes degraded by neutrophil myeloperoxidase induce less pulmonary inflammation, Nat Nano 5 (2010) 354–359

[21] E. V Litasova, V.V. Iljin, A. V. Sokolov, V. B. Vasilyev, M. A. Dumpis, L. B. Piotrovskiy, The biodegradation of fullerene C60 by myeloperoxidase, Dokl Biochem Biophys. 471 (2016), 417-420

[22] S. P. Mukherjee, A. R. Gliga, B. Lazzaretto, B. Brandner, M. Fielden, C. Vogt, L. Newman, A. F. Rodrigues, W. Shao, P. M. Fournier, M. S. Toprak, A. Star, K. Kostarelos, K. Bhattacharyaa, B. Fadeel, Graphene oxide is degraded by neutrophils and the degradation products are non-genotoxic, Nanoscale 10 (2018) 1180

[23] M. B. Hampton, A. J. Kettle, C. C. Winterbourn, Inside the neutrophil phagosome: oxidants, myeloperoxidase, and bacterial killing, Blood 92 (1998) 3007-3017

[24] V. E. Kagan, A. A. Kapralov, C. M. St. Croix, S. C. Watkins, E. R. Kisin, G. P. Kotchey, K. Balasubramanian, I. I. Vlasova, J. Yu, K. Kim, W. Seo, R. K. Mallampalli, A. Star, A. A. Shvedova, Lung Macrophages "Digest" Carbon Nanotubes Using a Superoxide/Peroxynitrite Oxidative Pathway, ACS Nano 8 (2014) 5610-5621

[25] K. Bhattacharya, C. Sacchetti, P. M. Costa, J. Sommertune, B. D. Brandner, A. Magrini, N. Rosato, N. Bottini, M. Bottini, B. Fadeel, Nitric Oxide Dependent Degradation of Polyethylene Glycol-Modified Single-Walled Carbon Nanotubes: Implications for Intra-Articular Delivery, Adv Healthc Mater. 7 (2018)

[26] EUNCL-NCL_STE2.1 Detection of Microbial Contamination, http://www.euncl.eu/about-us/assay-cascade/PDFs/Prescreening/EUNCL-STE-002_2.pdf?m=1476164583&

[27] M. Polimeni, E. Gazzano, M. Ghiazza, I. Fenoglio, A. Bosia, B. Fubini, D. Ghigo Quartz inhibits glucose 6-phosphate dehydrogenase in murine alveolar macrophages, Chem. Res. Toxicol. 21 (2008) 888

[28] M. Li, W. Li, S. Liu, Hydrothermal synthesis, characterization, and KOH activation of carbon spheres from glucose, Carbohydr Res. 346 (2011) 999-1004

[29] Y. Qi, M. Zhang, L. Qia, Y. Qi, Mechanism for the formation and growth of carbonaceous spheres from sucrose by hydrothermal carbonization, RSC Adv. 6 (2016) 20814-20823

[30] N. S. Abadeer, C. J. Murphy, Recent Progress in Cancer Thermal Therapy Using Gold Nanoparticles, J. Phys. Chem. C 120 (2016) 4691-4716

[31] M. E. Rodríguez, I. S. Cogno, L. S. Milla Sanabria, Y. S. Morána, V. A. Rivarolaa, Heat shock proteins in the context of photodynamic therapy: autophagy, apoptosis and immunogenic cell death, Photochem. Photobiol. Sci. 15 (2016) 1090–1102

[32] C. Liu, H. Qin, L. Kang, Z. Chen, H. Wang, H. Qiu, J. Ren, X. Qu, Graphitic carbon nitride nanosheets as a multifunctional nanoplatform for photochemical internalization-enhanced photodynamic therapy, J. Mater. Chem. B 6 (2018) 7908-7915

[33] S. K. Calderwood and D. R. Ciocca, Heat shock proteins: Stress proteins with Janus-like properties in cancer, Int J Hyperthermia 24 (2008) 31-39

[34] I. Postiglione, F. Barra, S. M. Aloj, G. Palumbo, Photodynamic therapy with 5-aminolaevulinic acid and DNA damage: unravelling roles of p53 and ABCG2, Cell Prolif. 49 (2016) 523-38

[35] L. Cobler, H. Zhang, P. Suri,C. Park C, L.A. Timmerman, xCT inhibition sensitizes tumors to γ-radiation via glutathione reduction, Oncotarget. 9 (2018) 32280-32297

[36] J. P. Banáth, D. Klokov, S. H. MacPhail, C. A. Banuelos, P. L. Olive, Residual gammaH2AX foci as an indication of lethal DNA lesions, BMC Cancer. 10 (2010) 4

[37] Z. H. Miao, H. Wang, H. Yang, Z. Li, L. Zhen, C. Y. Xu, Glucose-Derived Carbonaceous Nanospheres for Photoacoustic Imaging and Photothermal Therapy, ACS Appl. Mater. Interfaces 8 (2016) 15904-15910

[38] K. Wang, Y. Zhang, J. Wang, A. Yuan, M. Sun, J. Wu, Y. Hu, Self-assembled IR780-loaded transferrin nanoparticles as an imaging, targeting and PDT/PTT agent for cancer therapy, Sci Rep. 6 (2016) 27421

[39] W. Xing , G. Lalwani, I. Rusakova, B. Sitharaman, Degradation of Graphene by Hydrogen Peroxide, Part Part Syst Char, 31 (2014) 745-750

[40] Bay 2014

[41] L. Newman, N. Lozano, M. Zhang, S. Iijima, M. Yudasaka, C. Bussy & K. Kostarelos, Hypochlorite degrades 2D graphene oxide sheets faster than 1D oxidised carbon nanotubes and nanohorns, npj 2D Materials and Applications 1 (2017) 39

Chapter 3

Identification of the physical-chemical properties modulating nanoparticles aggregation potential in blood

This Chapter is part of the submitted article:

L. Soddu, D. N. Trinh, E. Dunne, D. Kenny, G. Bernardini, I. Kokalari, A. Marucco, M. P. Monopoli, I. Fenoglio, Beilstein Arch. 2019, 2019112

3.1 Introduction

Nanomedicine is probably one of the most exciting field of research in the branch of nanotechnology as it has the potential to offer practical and effective solutions on several diseases where traditional drugs currently fail. However, a tremendous gap exists between the number of formulations proposed and those approved for clinics [1]. Among the several factors that hampers the translation process, the most critical ones are the batch-to-batch variability and the poor knowledge of the properties modulating nanomaterial efficacy and safety [2].

Safe-by-design (SbD) approach has a great potential in accelerating the entrance of medicines into market [3], reducing pre-clinical research and costs. However, a deep knowledge of the processes leading to the adverse effects and of the physico-chemical properties governing such processes are mandatory to build structure-activity relationships (SARs) that in turn enable the SbD approaches. To the latter aspect, knowledge may only be derived by collecting a substantial amount of data from libraries of nanomaterials with definite synthetic properties. Therefore, understanding the processes that occur in the bloodstream are particularly relevant, not only for nanoformulations administered by intravenous injection, but also for any material introduced into the body.

Nanoparticles have been found to be able of promoting both haemorrhage or thrombosis [4,5], by interfering with the coagulation system through different pathways. Depletion of soluble coagulation factors (e.g fibrinogen, XII factor) may occur following adsorption of the factors at the surface of the nanoparticles. On the other hand, activation of some factors by surface-driven exposure of cryptic domains following adsorption was reported in some studies. Other studies reported the ability of nanoparticles to damage or activate platelets, endothelial cells or monocytes [5].

Physico-chemical properties were found to be critical in determining the ability of the materials to induce adverse effects. Several studies focused on the effect of surface charge and particle size. Albeit such properties were shown to clearly affect the pro-anticoagulant activity of nanoparticles, the direction of the effect varies, depending on the kind of material. For example, positive charged dendritic

nanoparticles were found to be more thrombogenic than negatively charged while for polystyrene nanoparticles both positive and negative charged surfaces were found to induce platelet activation [6,7]. These differences are likely due to the coexistence of different molecular processes, but also to the combined effect of different physico-chemical properties.

Due to their promising properties, carbon and silica nanoparticles are among the most studied inorganic materials for medical applications. Their ability to induce thrombus formation, along with their mechanisms of action, is still under debate. Both single-walled carbon nanotubes (SWCNTs) and multiwalled carbon nanotubes (MWCNTs) were found to induce platelet activation [8,9] by perturbing Ca2+ homeostasis, an effect that was hypothesized to be caused by the interaction of CNT with plasma and dense tubular system membranes likely related to the fibrous shape [10]. On the other hand, contrasting data have been reported on the potential of isometric carbon nanoparticles like carbon black, fullerenes and diesel exhaust to induce platelet activation and aggregation [8,9,11]. Systemic administration of carbon black in mice resulted in fibrinogen and platelet deposition in post capillary venules in the liver and heart [12,13], suggesting a role of this protein in nanoparticle mediated platelet aggregation.

Silica nanoparticles of different sizes were found to activate glycoprotein IIb/IIIa and to induce the expression of P-selectin [14] in platelets. On the other hand, silica nanoparticles are known to induce oxidative stress in several cell lines including endothelial cells [15] and leucocytes [16,17], a process that in vivo may indirectly induce platelet aggregation.

The interference with the coagulation system is not the only possible mechanism that may induce vascular occlusion. Nanoparticles have a strong tendency to agglomerate in water. The degree and kinetics of agglomeration are controlled by size, shape and surface chemistry of the particles. Strong repulsive electrostatic charges and steric hindrance may stabilize the nanoparticles and prevent agglomeration. In the bloodstream, agglomeration is related to the formation of a biocorona that modifies the electrostatic and steric repulsion among particles [18].

Finally, protein–protein interaction may lead to bridging among particles thus promoting agglomeration [19].

In the present study, a sample set of six silica and carbon nanoparticles with definite size and morphology was used to explore the effect of size and surface properties on the protein corona composition, agglomeration in plasma, platelet aggregation, activation and VWF-mediated adhesion.

3.2 Materials and methods

3.2.1 Synthesis of carbon nanoparticles.

Carbon nanoparticles (CNP) were produced starting from glucose using a one-step hydrothermal process as described in Kokalari et al. 2019 [20]. Briefly, glucose was dissolved in 50 ml of ultrapure
water followed by the addition of 15 mg of sodium polyacrilate. The solution was introduced in a pressure reactor system (Büchi AG) and heated at 190°C for 3 or 8 h. Synthesis parameters are described in details in table 3.1. CNP were then purified using ultrapure water by filtration for large carbon nanoparticles (CNP-L) or tangential flow ultrafiltration (Vivaflow 50R, MW 30 kDa) for the
medium and small carbon nanoparticles (CNP-M and CNP-S).

Table 3.1. Synthesis parameters used for CNP

	Glucose (g)	**Surfactant (mg)**	**Time (h)**	**Temperature, (°C)**
CNP-S	2	15	3	190
CNP-M	2	15	8	190
CNP-L	5	15	8	190

3.2.2 Synthesis of silica nanoparticles.

The silica nanoparticles (SNP) were prepared by hydrolysis and condensation of TEOS in the presence of ammonia as a catalyst, based on the Stöber process [21]. Briefly, a defined amount of TEOS was added dropwise, under magnetic stirring, at room temperature, to a solution of ethanol, ammonia (33%) and ultrapure water. The detailed protocols are summarized in table 3.2.

The suspensions were subjected to repeated centrifugation steps at 11.000 rpm, for 15 min, in ultrapure water and ethanol in order to isolate and wash the nanoparticles. The purified nanoparticles were suspended in ultrapure water and stored at 4°C.

Table 3.2. Synthesis parameters for silica nanoparticles

	TEOS (ml)	**Ethanol (ml)**	**NH_3 (ml)**	**H_2O (ml)**	**Time (min)**
SNP-S	0.756	20	0.852	0.831	40
SNP-M	0.756	20	1.704	1.067	40
SNP-L	0.330	44	18	-	30

3.2.3 Scanning Electron Microscopy (SEM).

Nanoparticle morphology was characterized using scanning electron microscopy, SEM Zeiss Evo 50XVP (Assing). Carbon and silica nanoparticles suspensions were diluted up to 0.05 mg/ml in ultrapure water. A volume of 20 μl of the diluted suspensions was mounted on aluminium stubs, using double-sided adhesive carbon tape and silicon wafers. Samples were dried overnight at room temperature. In the case of silica nanoparticles, the samples were sputter-coated with thick gold film (~ 17 nm) under argon atmosphere to improve secondary electron emission during SEM imaging. Nanoparticle morphology was observed at an acceleration voltage of 20 kV.

3.2.4 Dynamic Light scattering (DLS).

The mean diameter and polydispersity index (PDI) of nanoparticles were obtained using a Zetasizer (Nano ZS Malvern Instruments, UK) based on the dynamic light

scattering (DLS) technique. Measurements were performed on purified nanoparticles by analysing 0.5 ml of suspension in ultrapure water, placed in a square polystyrene cuvette, at 25 °C. PBS 0.01 M, pH 7.4, Sigma Aldrich, was used as a diluent in the case of the evaluation of the size after the protein corona formation.

3.2.5 Nanoparticle Tracking Analysis (NTA)

Analysis of the size distribution and concentration of CNP and SNP were performed by NTA using a Nanosight NS300 (Malvern, UK) equipped with a blue laser (488 nm) and a quartz chamber for sample injection, equipped with an O-ring top plate. For nanoparticles-hard protein corona complexes, the samples were diluted in PBS, 0.01 M, pH 7.4. Dilution factor was chosen in order to obtain 30 particles per frame, as suggested by the manufacturer's recommendations. The measurement duration was set at 60s.

3.2.6 ζ-potential

Zeta-potential measurements were performed based on the Electrophoretic Light Scattering (ELS) technique, using Zetasizer (Nano ZS Malvern Instruments, UK) as a function of the pH in the range from 2-9. The nanoparticles suspensions were diluted in ultrapure water at a final concentration of 0.5 mg/ml. The pH of the suspensions was adjusted by adding diluted NaOH or HCl solutions and the samples were introduced in a disposable folded capillary cuvettes (Malvern Panalytical).

3.2.7 Protein corona characterization

3.7.1 Procurement and preparation of plasma.

The human plasma was obtained from healthy donors kindly provided by the Irish Blood Transfusion Service (IBTS), St. James Hospital, Dublin. The plasma from eight different donors was mixed, aliquoted and stored -80°C until use. Before

using, the plasma was thawed and centrifuged at 16.000 rpm, 3 min, in order to discard any precipitated protein.

3.7.2 Methods

Carbon and silica nanoparticles were incubated with different concentrations of human plasma diluted in PBS 0.01M, pH 7.4 (Sigma Aldrich) at 37°C under agitation (150 rpm). The number of nanoparticles in all samples was optimized in order to ensure a total surface area of 1.0×10^{-2} m^2. After the incubation, in order to obtain nanoparticles-hard protein corona complexes, the samples were washed three times by centrifugation as previously described [22]. After the last washing step, the pelleted samples were suspended in PBS, 0.01 M, pH 7.4, and the denaturizing solution, prepared with dithiothreitol and 3x blue loading buffer that contained DTT in a ratio of 1:10 (New England biolabs) and following the manufacturer instructions. The samples were sonicated for 5 minutes in an ultrasonic bath and then incubated for 5 minutes at 95 °C to complete the protein denaturation. The samples were loaded in a 10-wells 12% stacking gel and the electrophoretic analysis was conducted at 130 V. After the electrophoretic separation, the gels were stained in Imperial Protein stain, (Thermo Scientific) for 1 h and distained overnight (in ultrapure water). The densitometry analysis was performed using the software ImageJ (NIH).

3.7.3 Mass spectrometry analysis

Samples were run on SDS-PAGE for 10 min before the protein bands were excised from the gel. The proteins in the gel pieces were reduced with dithiothreitol, alkylated with iodoacetamide and digested with trypsin (Promega Corporation) overnight at 37°C. The peptides were then extracted from the gel matrix and prepared for MS analysis by using Pierce C18 Tips (Thermo Fisher) following the manufacture procedure.

Peptide samples were analyzed on a quadrupole Orbitrap (Q-Exactive, Thermo Scientific) mass spectrometer equipped with a reversed-phase NanoLC UltiMate 3000 HPLC system (Thermo Scientific). Samples were loaded onto C18 reversed

phase columns (10cm length, 75µm inner diameter) and eluted with a linear gradient from 2 to 27% acetonitrile containing 0.5% acetic acid in 58 min at a flow rate of 250nL/min. The injection volume was 5µl. The mass spectrometer was operated in data dependent mode, automatically switching between MS and MS2 acquisition. Survey full scan MS spectra (m/z 300 – 1600) were acquired in the Orbitrap with a resolution of 70,000. MS2 spectra had a resolution of 17,500. The twelve most intense ions were sequentially isolated and fragmented by higher-energy C-trap dissociation.

MS raw files were processed with MaxQuant software (version 1.6.2). The peak lists were searched against the human FASTA database. The search included the modifications of cysteine carbamidomethylation, methionine oxidation and protein N-terminal acetylation. A maximum of two missed trypsin cleavages were allowed in the database search. The false discovery rate for both peptides and proteins was set at 1%. After that, the ProteinGroup file from Maxquant was processed, filtered and analysed with Perseus software to generate the top abundance table, hierarchical clustering graph and numeric Venn diagrams.

3.3 Results and discussion

The identification of the correlations existing among physico-chemical properties and biological effects is a laborious but necessary process allowing the design of more efficacious and safe substances for medical applications. In the case of nanobiomaterials (NBM) this process is more challenging than for molecular substances, due to the higher number of parameters to be controlled. A library of nanomaterials that differ by one single property at time and accurate testing strategies are necessary. This is not always straightforward due to the interdependence between the various chemical and physical properties.

In the present study, two sets of nanoparticles were prepared with the aim to specifically investigate the effect of the surface curvature and surface chemistry on platelet-dependent and independent aggregation, platelet activation and adhesion. Silica and carbon nanoparticles were chosen since both are highly studied for medical applications. Furthermore, being produced by wet methods, these nanoparticles have both hydrophilic surfaces and are negatively charged. Their comparison, therefore excludes surface charge and hydrophilicity as variables to be investigated. In Figure 3.1 the strategy used to unravel possible SARs is reported.

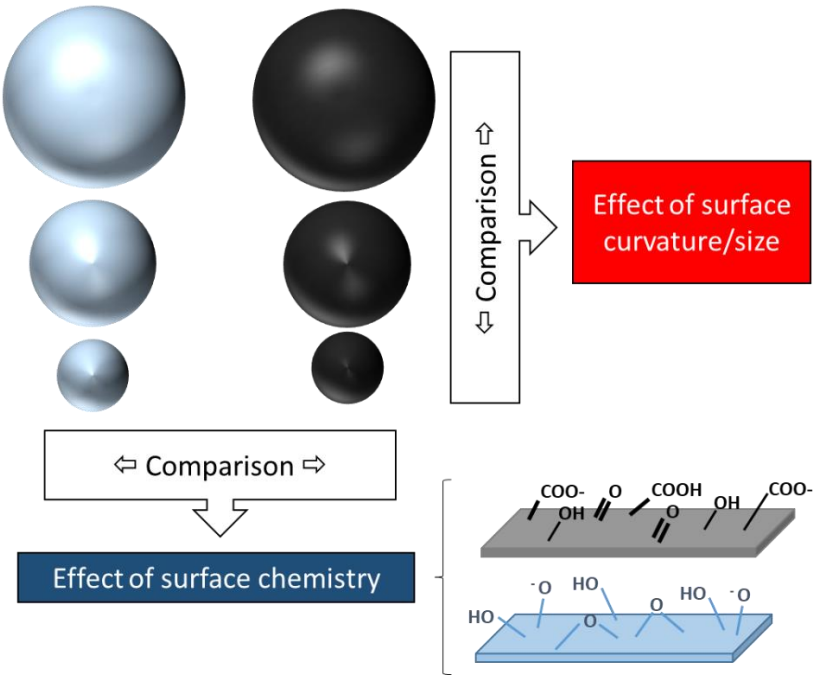

Figure 3.1. Strategy used to unravel possible structure-activity relationships.

This strategy allowed us to identify surface chemistry as key factor in the protein corona composition while both surface chemistry and size modulate a platelet-independent aggregation potential of particles in blood.

3.3.1 Physicochemical characterization of the samples

Data show that the matching set of nanoparticles had similar mean hydrodynamic diameters. DLS and NTA mean hydrodynamic diameters (Table 3.3) confirmed a similar size distribution across the two materials. The low polydispersity indexes indicate high colloidal stability and narrow size range distribution.

Table 3.3. Mean of hydrodynamic diameters, PDI and standard deviation of each sample measured after purification obtained with DLS (white background), compared with the mean of hydrodynamic diameters and standard deviation obtained using NTA (grey background).

	DLS			NTA	
	Hydrodynamic diameters (nm)	**Standard Dev.**	**PDI**	**Hydrodynamic diameters (nm)**	**Standard Dev.**
SNP-S	114.1	±0.351	0.081	115.0	±1.52
SNP-M	235.1	±4.754	0.012	217.3	±4.16
SNP-L	488.1	±5.387	0.031	333.3	±14.5
CNP-S	179.5	±3.482	0.074	128.3	±2.52
CNP-M	259.7	±2.193	0.010	232.0	±6.08
CNP-L	485.2	±2.452	0.123	349.0	±4.36

The hydrodynamic diameters measured by NTA were similar to those measured by DLS, except for the large samples, for which the NTA value was lower. In fact, NTA, but not DLS, detected four populations of particles having a different size that, in DLS contribute to the mean diameter observed (figure 3.2). This is in agreement with the PDI higher than the others.

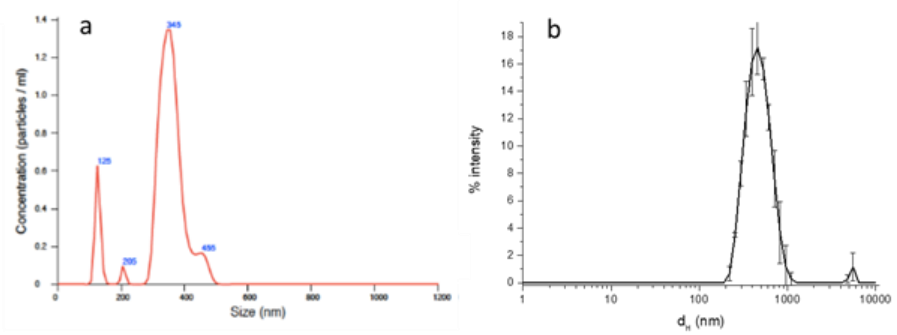

Figure 3.2. Representative size distribution measured by a) NTA and b) DLS of the sample SNP-L.

In figure 3.3 the representative SEM images of the samples are presented. All particles appear perfectly spherical with a uniform size, the latter confirming the DLS analysis.

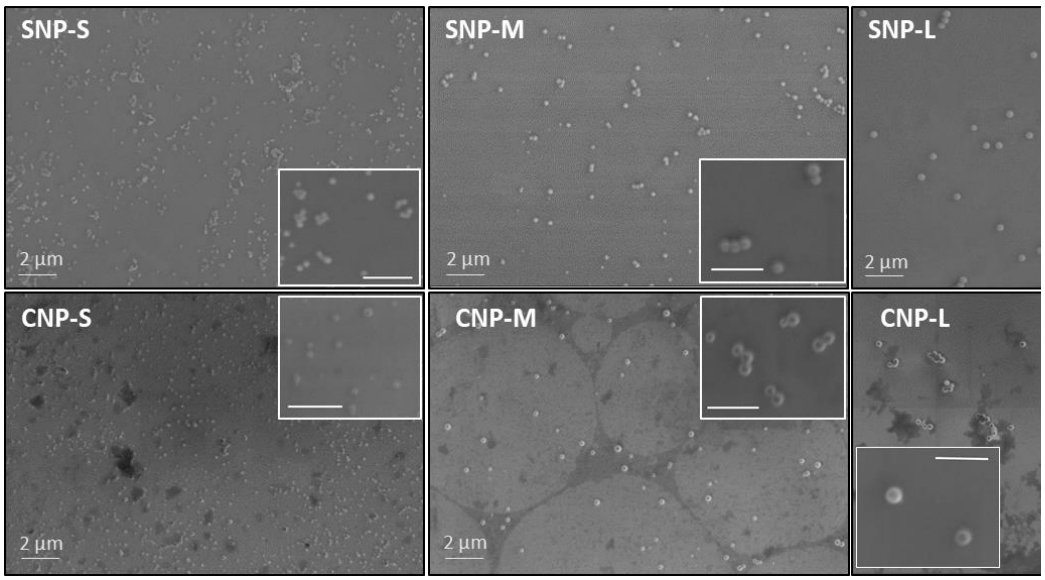

Figure 3.3. SEM micrograph of silica and carbon nanoparticles

The ζ- potential of the samples was measured by ELS in the pH range from 2 to 9 (Figure 3.4a)

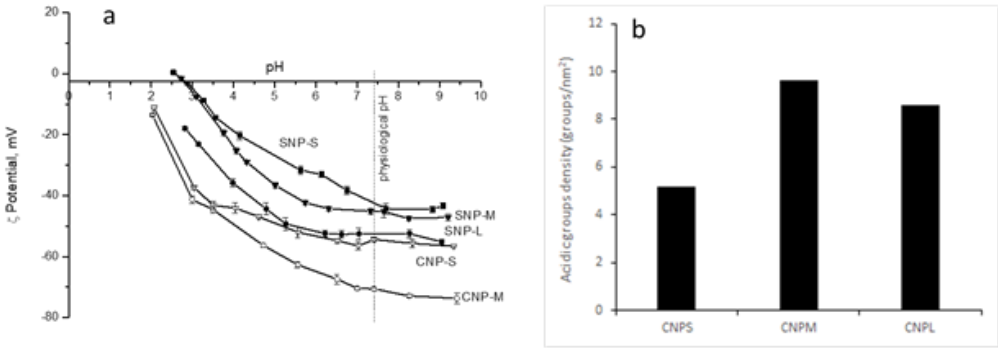

Figure 3.4. a) Zeta potential versus pH curves for carbon nanoparticles (CNP-M and CNP-S) and silica nanoparticles (SNP-L, SNP-M and SNP-S) suspended in water. b) Density of acid groups exposed at the surface of carbon nanoparticles.

As expected, both silica and carbon samples exhibited a negative zeta potential across the whole pH range. It gradually increased with increasing of the pH of the suspension never reaching positive values indicating the presence of weakly acidic groups. In the case of carbon nanoparticles, acidic carboxylic or phenolic groups formed during the synthesis are expected, while silica exposes at the surface hydroxyl groups. At physiological pH (7.4) all particles exhibit a high ζ-potential in the range of -40/-70 mV. Carbon nanoparticles exhibit a ζ- potential more negative than the correspondent silica nanoparticles. Note that the ζ-potential curve of CNP-L is not reported since this samples rapidly agglomerate by lowering the pH value, making unfeasible the measurement.

The presence of acidic groups at the surface of carbon nanoparticles was quantified by titration using the dye thionine acetate [23]. In Figure 3.4b the density of acidic groups for carbon nanoparticles is reported. The three samples differ slightly in terms of the density of acidic surface groups, with the small NPs having the lowest density, in agreement with the observed less negative ζ-potential value. The density of the acidic groups for silica was not determined since widely reported in literature [24], [25].

3.3.2 Physicochemical and proteomics characterisation of the NP-Hard corona

We then evaluated how the NP physicochemical properties would affect the biomolecular corona formation. For this purpose, we exposed the same surface area of three sized NP of silica and carbon to increasing concentrations of human plasma, 10% to 80%, to mimic the in vitro / in vivo conditions respectively. After 1 hour incubation at 37°C, the NP-corona complexes were separated from unbound proteins and washed three times by centrifugation. SDS-PAGE and MS were used to obtain information on the biomolecular corona composition in each sample. In Figure 3.5 the SDS-PAGE gels for the small silica and carbon nanoparticles are shown. The corona composition between the two materials has some similarities when incubated at 10% of plasma, however it became highly specific to the NP surface properties at higher concentration as we detected a

significantly difference in the corona composition. In particular, at 10% of plasma, both NPs preferentially adsorb three gel bands of 72, 60 and 50kDa, later identified as fibrinogen alpha, beta and gamma chain respectively, but significant differences were also observed at lower molecular weight where a gel band of 25kDa was detected in the silica corona while in the carbon NP corona was formed by 3 gel bands in the region of 36-30kDa and a less pronounced band of a MW lower than 28kDa. At higher plasma concentration, the corona composition of the SNP changed significantly where the fibrinogen gel bands were displaced by three predominant bands of 90kDa and a duplet of 50kDa, later identified with histidine rich glycoprotein. These findings were in agreement with a previous study where a similar effect was detected for 200nm silica NP as previously reported [22]. Notably, the bands of correspondent to fibrinogen become more attenuated at higher percentage of plasma in silica, but remain abundant in carbon nanocorona (Figure 3.7). Small molecular weight bands also became displaced at higher plasma concentration.

Little differences in the protein corona composition were found depending upon the size of the nanoparticles (Figure 3.6) suggesting that the surface curvature, in the range considered, plays a minor role.

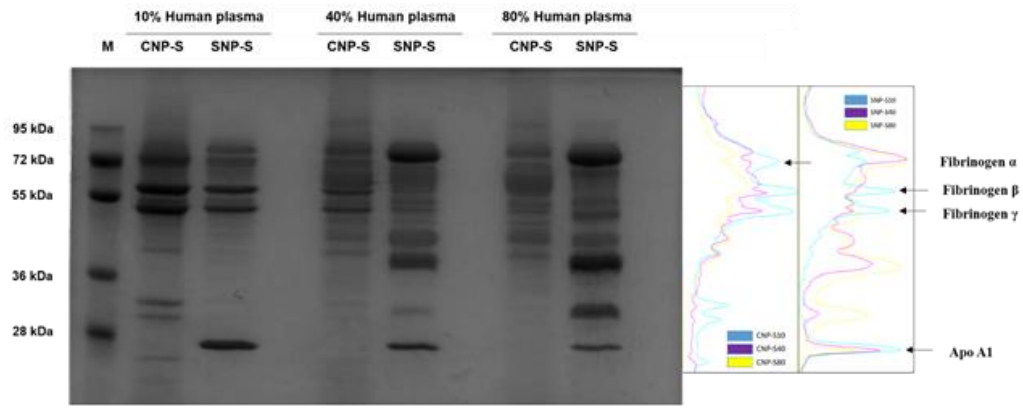

Figure 3.5. SDS-PAGE gel of hard protein corona formed after 1h of incubation in human plasma.

The gel bands correspondent to fibrinogen and apolipoprotein A1 are shown.

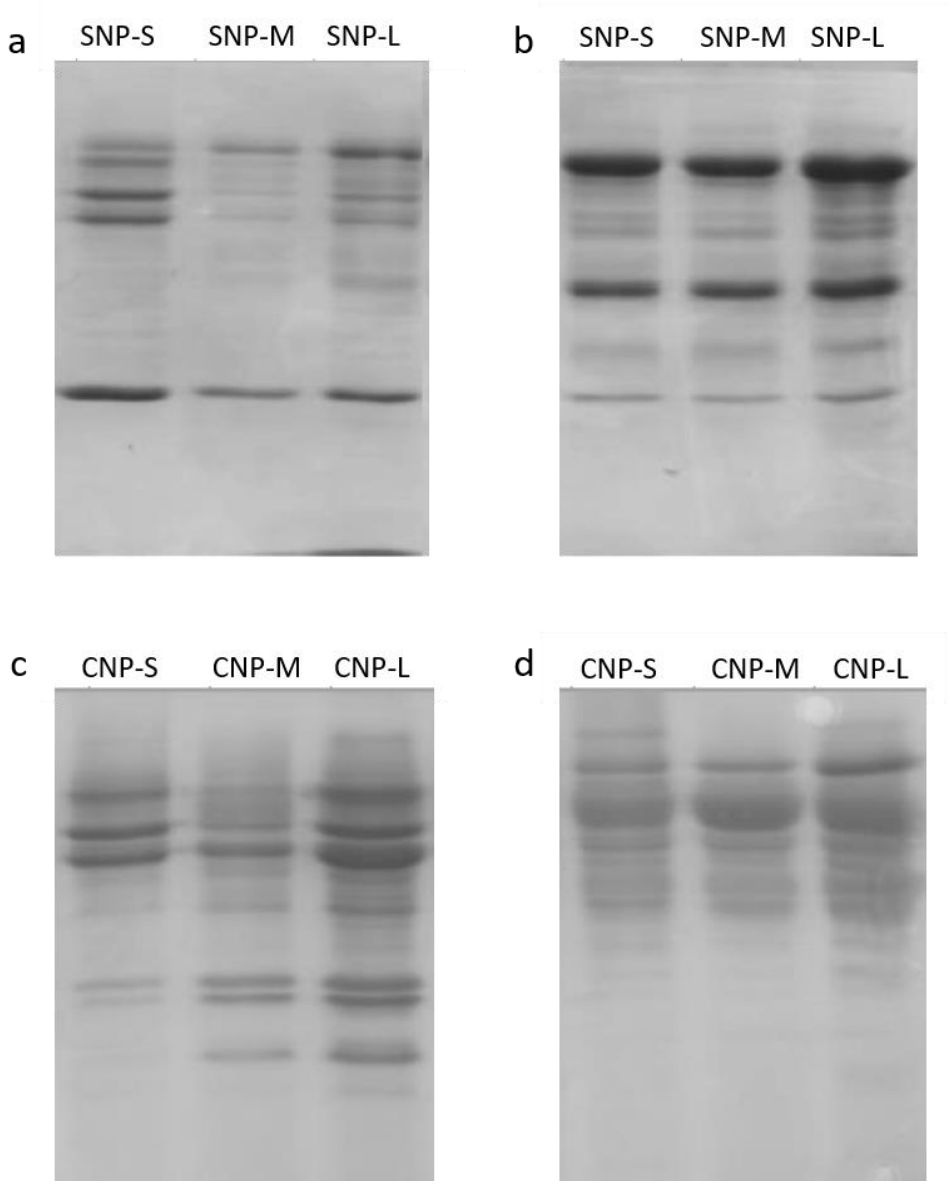

Figure 3.6. Effect of size on the composition of the protein corona. Panel a) and c) 10% human plasma, b) and d) 80% human plasma

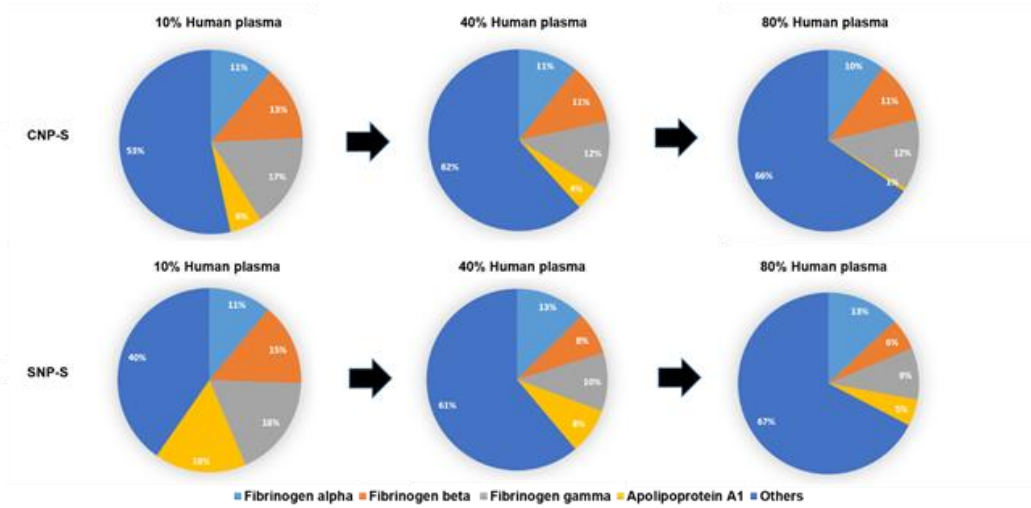

Figure 3.7. Abundance of fibrinogen and apolipoprotein A1 in silica and carbon corona at different plasma concentration.

Label-free mass spectrometry was used to obtain the semiquantitative protein abundance of the corona of small silica and carbon NP across three different plasma concentrations. A total of 118 proteins were found in the biomolecular corona of small carbon and silica NPs after incubation with human plasma 10, 40 and 80%. Table 3.4 contains the top 20 proteins detected in each condition by MS.

Table 3.4. Top 20 most abundant proteins in small silica (SNP-S) and carbon (CNP-S) hard corona samples at three different plasma concentration (10, 40, 80%) based on the LFQ intensity.

Order of abundance	SNP-S			CNP-S		
	10% Human plasma	40% Human plasma	80% Human plasma	10% Human plasma	40% Human plasma	80% Human plasma
1	Fibrinogen gamma chain	Kininogen-1	Kininogen-1	Fibrinogen beta chain	Fibrinogen beta chain	Kininogen-1
2	Fibrinogen alpha chain	Fibrinogen alpha chain	Histidine-rich glycoprotein	Fibrinogen alpha chain	Fibrinogen gamma chain	Fibrinogen alpha chain
3	Fibrinogen beta chain	Fibrinogen beta chain	Kallikrein B	Fibrinogen gamma chain	Fibrinogen alpha chain	ITIH4 protein
4	Apolipoprotein A-I	Fibrinogen gamma chain	Coagulation factor XI	Apolipoprotein B-100	Kininogen-1	Fibrinogen beta chain
5	Kininogen-1	Apolipoprotein A-I	Plasminogen	Histidine-rich glycoprotein	ITIH4 protein	Fibrinogen gamma chain
6	Apolipoprotein E	Histidine-rich glycoprotein	Apolipoprotein A-I	Kininogen-1	Vitronectin	Coagulation factor XI
7	Histidine-rich glycoprotein	Kallikrein B	Plasma protease C1 inhibitor	Vitronectin	Apolipoprotein B-100	Vitronectin
8	Apolipoprotein B-100	Coagulation factor XI	Fibrinogen alpha chain	Complement C1q	Plasma kallikrein	Kallikrein B
9	Kallikrein B	Apolipoprotein E	Apolipoprotein B-100	Complement component 4B	Apolipoprotein E	Histidine-rich glycoprotein
10	Plasma protease C1 inhibitor	Coagulation factor XII	Fibrinogen beta chain	Complement factor H	Complement component 4B	Apolipoprotein B-100
11	Selenoprotein P	Selenoprotein P	Fibrinogen gamma chain	Apolipoprotein E	Coagulation factor XI	Apolipoprotein E
12	Coagulation factor XII	Plasminogen	Serum albumin	ITIH4 protein	Serum albumin	Serum albumin
13	ITIH4 protein	Plasma protease C1 inhibitor	ITIH4 protein	Serum albumin	Complement factor H	Complement C3
14	Serum albumin	Serum albumin	Selenoprotein P	Complement component 1	Complement component 1	Ig gamma-3 chain C region
15	Complement C3	ITIH4 protein	Apolipoprotein E	Complement C3	Complement C3	Isoform C of Proteoglycan 4
16	Plasminogen	Ig gamma-3 chain C region	serine protease inhibitor	Kallikrein B	serine protease inhibitor	Ig mu chain C region
17	Coagulation factor XI	Complement C3	Ig kappa chain C region	Apolipoprotein A-I	Complement factor H-related protein 1	Selenoprotein P
18	Isoform C of Fibulin-1	Ig alpha-1 chain C region	Ig gamma-3 chain C region	Ig gamma-3 chain C region	protease C1 inhibitor	serine protease inhibitor
19	Apolipoprotein A-II	Apolipoprotein A-II	Ig alpha-1 chain C region	Ig mu chain C region	Complement C1q	Ig kappa chain C region
20	Apolipoprotein C-I	Vitronectin	Complement C3	Coagulation factor XI	Ig gamma-3 chain C region	Complement factor H-related protein 1

Figure 3.8. Venn diagrams showing the number of proteins shared by small silica (Black) and carbon NP (Grey) protein corona formed at different plasma concentrations.

Venn diagrams (Figure 3.8) highlighted that the majority of the proteins were detected both in the SNP and CNP at the higher plasma concentrations, while a minor overlap occurred at 10%. However, a pronounced difference was observed when we compared the protein abundance by means of the label free quantification (LFQ) across all conditions (Table 3.4 and Figure 3.9).

The presence of fibrinogen decreased firmly with increasing plasma concentration (80%) in silica nano-corona, and was is displaced by less abundant but with higher affinity proteins, like histidine rich glycoprotein, kallikrein B and plasminogen confirming the SDS-PAGE findings and the literature.

Apolipoprotein A1, a major protein that form the HDL, has shown to have a preferential affinity towards silica NP where it was detected across all conditions. The findings were also in agreement with the SDS-PAGE where a gel band of 28kDa was detected only for silica NP. Other HDL apolipopoproteins including apoA2 and A4 are also more abundant in silica corona than carbon one, which might be attributed to the surface chemistry.

Interestingly, fibrinogen was strongly bound to the CNP also at higher concentration of plasma, although with a less amount. Similarly ApoB100, ApoB100, a protein that forms the VLDL/LDL, and histidine rich glycoprotein were enriched at 10% of plasma but they become displaced by other proteins, such as vitronectin and ITIH4 at higher concentration of plasma in CNPs. Interestingly, albumin (66 kDa), the most abundant protein in human plasma, is outside the top 10 proteins identified with MS in all samples.

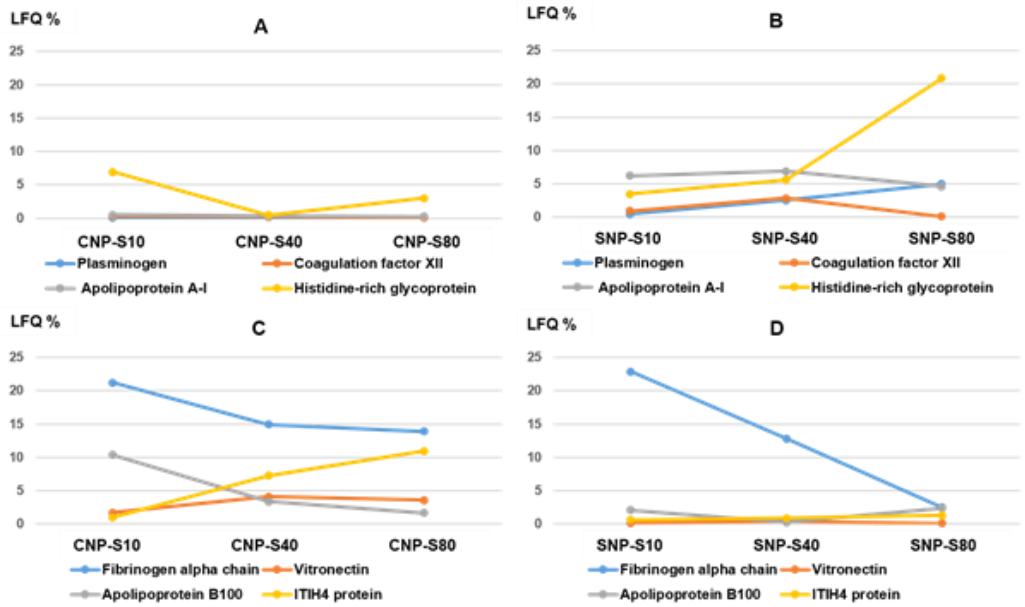

Figure 3.9. Relative concentration of relevant proteins on small silica (SNP) and carbon (CNP) coronas at plasma concentrations of 10, 40 and 80%. The percentages were calculated based on the total LFQ intensity in each sample.

Protein grouping (Figure 3.10) confirmed that the coagulation factors are highly enriched in the corona across all conditions although with different percentage (55-75%).

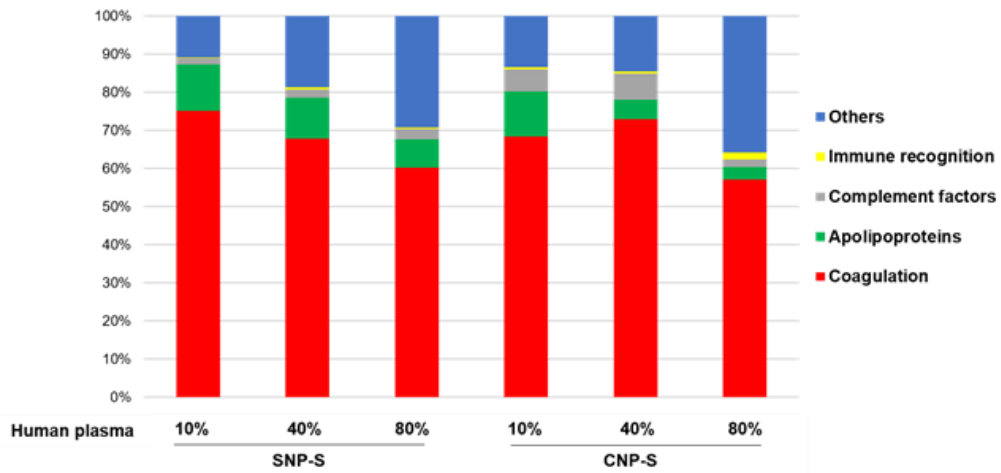

Figure 3.10. Classification of the human plasma corona proteins identified on small silica (SNP-S) and carbon (CNP-S) NPs according to their biological

functions. The LFQ intensity is used to calculate the percentages of protein groups.

In terms of molecular weights, most proteins found in the corona of both nanomaterials are between 20-60 kDa in weight, which accounts for about 70% of proteins (SI). Around 8% of the total corona proteins have high molecular weights (>150 kDa).

3.3.3 Effect of hard corona on agglomeration

The effect of the protein corona on the tendency of nanoparticles to agglomerate was evaluated by preparing the protein corona using the protocol described above, re-suspending the particles in PBS and measuring the size distribution by NTA. The mean hydrodynamic diameters of the particles with the protein corona generated at three different plasma concentration (10, 40 and 80%) are compared in Figure 3.11 with the hydrodynamic diameter of the pristine nanoparticles.

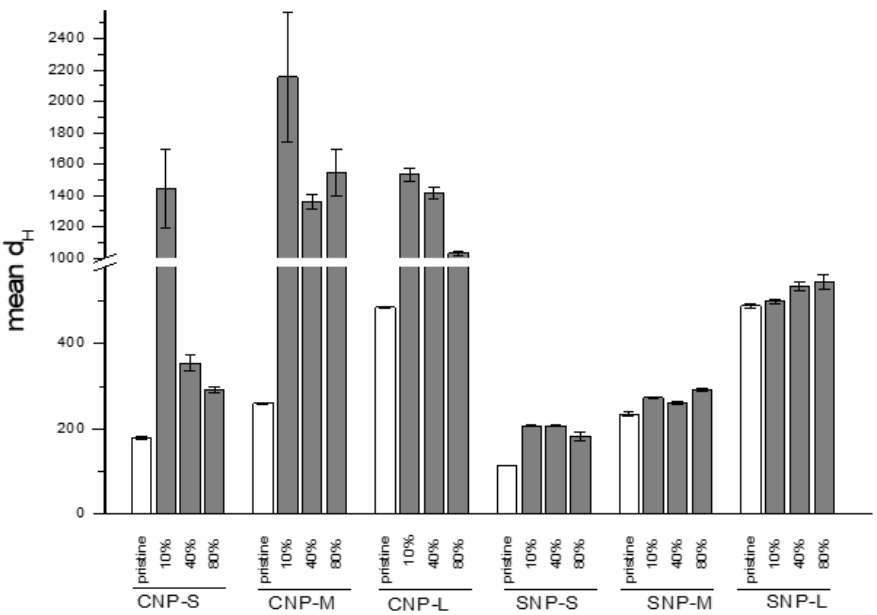

Figure 3.11. Effect of hard corona formed at different plasma concentrations on nanoparticles agglomeration in water.

The presence of the hard protein corona induced a substantial agglomeration in all carbon nanoparticles. This effect was evident for the protein corona formed in plasma at 10% concentration. By increasing the plasma concentration, the mean hydrodynamic size of the small carbon nanoparticles become similar to the nanoparticles without the protein corona. Conversely, large and mean size carbon nanoparticles remain highly agglomerated with a mean size higher than 1 μm. In the case of silica nanoparticles no agglomeration were observed at all concentrations of plasma tested.

3.3.4 Effect of the nanoparticles on platelet aggregation, platelet activation and platelet adhesion

Platelet aggregation is a complex process modulated by several chemical and physical parameters.

Ordinarily platelets circulate in blood in a quiescent state near the endothelial cells lining the blood vessels without forming stable adhesions. After infringement of the vasculature proteins like von Willebrand factor (VWF), collagen and fibronectin are exposed on the sub endothelial matrix and act as ligands for platelet surface receptors, glycoproteins like GPVI and GPIbα [26], [27], [28]. These receptor-ligand interactions initiate a cascade of intracellular responses resulting in amplification of platelet activation through the secretion of soluble agonists including thromboxane A2 (TXA2) and ADP. TXA2 and ADP act jointly with the engaged platelet receptors to mobilize intracellular Ca^{2+}, which instigates platelet shape change, degranulation, and up-regulation of the adhesive function of another platelet surface receptor, integrin αIIbβ3 [26]. The active conformation of αIIbβ3 integrin can then bind fibrinogen (FG), VWF and fibronectin with high affinity allowing haemostatic platelets to aggregate and thrombus formation [29]. FG plays a key role in platelet aggregation, forming bridges between platelets and acting as an aggregation glue. On the other hand, FG also has a key role in surface-driven aggregation. FG has a high affinity for surfaces [30] and it is commonly present in the protein layer/corona of several materials [22]. On hydrophilic

surfaces, this protein tends to be displaced by other proteins by a mechanism known as Vroman's effect [30]. However, in some cases adsorbed FG undergoes conformational changes thus exposing cryptic domains. Platelets may adhere to fibrinogen immobilized onto biomaterials through integrins, a mechanism that may lead to thrombotic events. Furthermore, in the case of NBM this protein may act as glue in a similar way to that observed with platelets [17], inducing nanoparticle aggregation. However, in this case, the effect is not due to the interaction with integrin, but it is a non-specific process due to the tendency of FG to form fibrils similar to fibrin. This tendency was a consequence of a different rearrangement of the FG molecule onto surfaces having different properties [19].
In this study, the effects of the nanoparticles on platelet aggregation, platelet activation and platelet adhesion were investigated and the experiments were performed by Ludovica Soddu, as part of her master thesis research activity, supported by the Programm Erasmus + and BIORIMA project.
It was found that when incubated in the presence of platelets, silica nanoparticles and small carbon nanoparticles induce only mild aggregation, in agreement with what previously found on silica nanoparticles [14]. Aggregation was observed for prolonged time of incubation with large carbon nanoparticles only. This process does not involve platelet activation and appears related to the ability of particles to act as bridges among platelets, similarly to that observed by other authors with other carbon nanomaterials [9], [11]. This was confirmed for large nanoparticles, while for medium size particles platelet activation cannot be excluded.
In light of these evidence, the observed reduction of VWF-mediated adhesion of platelets to endothelial wall induced by all NPs should be regarded as a consequence of the sequestration of platelets by particles. In fact, it was found that his effect is more evident for large particles.
The different aggregation potential of CNP depending upon their size may explain the contrasting data found in literature on isometric carbon nanoparticles. In fact, secretion of P-selectin in vitro was observed for carbon black [11] but not diesel exhaust particles [9], while platelet aggregation was observed for amorphous carbon nanoparticles but not for the small-sized fullerenes [8]. Note however that

limited information relating to the physico-chemical properties of these materials was given by these studies making it difficult to form a critical analysis of the results. Note moreover that while CNT was reported to induce platelet aggregation [8], [9] CNP did not. This support the hypothesis that an elongated shape is necessary for this process [10].

3.4 Conclusions

In conclusion, the present study suggest that NP-NP and NP-platelet aggregates may be generated in blood following administration of nanoparticles that are stable and monodisperse in water also without platelets activation. This process should be regarded as concern, since aggregates might induce vessels occlusion in vivo. CNPs have an aggregation potential higher than silica nanoparticles. However, the reduction of size to less than 100 nm appears to improve the stability these materials and, possibly, their biocompatibility. Further investigations will be necessary to confirm in vivo this hypothesis.

3.5 References

[1] J. B. Coty, C. Vauthier, Characterization of nanomedicines: A reflection on a field under construction needed for clinical translation success, J. Control. Release 275 (2018) 254–268

[2] A. A. Khorasani, J. L. Weaver, C. Salvador-Morales, Closing the gap: accelerating the translational process in nanomedicine by proposing standardized characterization techniques, Intern. J. Nanomed. 9 (2014) 5729–5751

[3] B. Fadeel, Nanosafety: towards safer design of nanomedicines, J. Internal Med. 274 (2013) 578-580

[4] A. N. Ilinskaya, M. A. Dobrovolskaia, Nanoparticles and the blood coagulation system. Part I: benefits of nanotechnology, Nanomedicine 8 (2013) 773-784

[5] A. N. Ilinskaya, M. A. Dobrovolskaia, Nanoparticles and the blood coagulation system. Part II: safety concerns, Nanomedicine 8 (2013) 969-981

[6] M. A. Dobrovolskaia, A. K. Patri, J. Simak, J. B. Hall, J. Semberova, S. H. De Paoli Lacerda, S. E. McNeil, Nanoparticle Size and Surface Charge Determine Effects of PAMAM Dendrimers on Human Platelets in Vitro, Mol. Pharmaceutics 9 (2012) 382–393

[7] C. F. Jones, R. A. Campbell, Z. Franks, C. C. Gibson , G. Thiagarajan, A. Vieira-de-Abreu, S. Sukavaneshvar, S. F. Mohammad, D. Y. Li, H. Ghandehari, A. S. Weyrich, B. D. Brooks, D. W. Grainger, Cationic PAMAM dendrimers disrupt key platelet functions, Mol Pharm. 9 (2012) 1599–1611

[8] J. Semberova, S. H. De Paoli Lacerda, O. Simakova, K. Holada, M. P. Gelderman, J. Simak, Carbon Nanotubes Activate Blood Platelets by Inducing Extracellular Ca2þ Influx Sensitive to Calcium Entry Inhibitors, Nano Lett. 9 (2009) 3312–3317

[9] P. Bihar, M. Holzer, M. Praetner, J. Fent, M. Lerchenberger, C. A. Reichel, M. Rehberg, S. Lakatos, F. Krombach, Single-walled carbon nanotubes activate platelets and accelerate thrombus formation in the microcirculation, Toxicology 10 (2010) 148-154

[10] S. H. De Paoli Lacerda, J. Semberova, K. Holada, O. Simakova, S. D. Hudson, J. Simak, Carbon Nanotubes Activate Store-Operated Calcium Entry in Human Blood Platelets, ACS Nano 5 (2011) 5808–5813

[11] M. Holzer, P. Bihari, M. Praetner, B. Uhl, C. Reichel, J. Fent, M. Vippola, S. Lakatos, F. Krombach, Carbon-based nanomaterials accelerate arteriolar thrombus formation in the murine microcirculation independently of their shape, J Appl. Toxicol. 34 (2014) 1167-1176

[12] A. Khandoga, T. Stoeger, A. G. Khandoga, P. Bihari, E. Karg, D. Ettehadieh, S. Lakatos, J. Fent, H. Schulz, F. J. Krombach, Platelet adhesion and fibrinogen deposition in murine microvessels upon inhalation of nanosized carbon particles, J Thrombosis Haemostasis 8 (2010) 1632–1640

[13] A. Khandoga, A. Stampfl, S. Takenaka, H. Schulz, R. Radykewicz, W. Kreyling, F. Krombach, ltrafine Particles Exert Prothrombotic but Not Inflammatory Effects on the Hepatic Microcirculation in Healthy Mice In Vivo, Circulation 109 (2004) 1320–1325

[14] J. J. Corbalan, C. Medina, A. Jacoby, T: Malinski, M. W. Radomski, Amorphous silica nanoparticles aggregate human platelets: potential implications for vascular homeostasis, Int. J. Nanomed. 7 (2012) 631–639

[15] D. Napierska, L. C. Thomassen, V. Rabolli, D. Lison, L. Gonzalez, M. Kirsch-Volders, J. A. Martens, P. H. Hoet, Size-Dependent Cytotoxicity of Monodisperse Silica Nanoparticles in Human Endothelial Cells, Small, 5 (2009) 846-853

[16] E. Gazzano, E. Ghiazza, M. Polimeni, V. Bolis, I. Fenoglio, A. Attanasio, G. Mazzucco, B.

Fubini, G. Ghigo, Physico-chemical determinants in the cellular responses to nanostructured amorphous silicas, Toxicol. Sci. 128 (2012) 158-170

[17] A. Marucco, E. Gazzano, D. Ghigo, E. Enrico, I. Fenoglio, Fibrinogen enhances the inflammatory response of alveolar macrophages to TiO2, SiO2 and carbon nanomaterials Nanotoxicology, Nanotoxicology 10 (2016) 1-9

[18] I. Fenoglio, B. Fubini, E. Ghibaudi, F. Turci, Multiple aspects of the interaction of biomacromolecules with inorganic surfaces, Adv. Drug Deliver. Rev. 63 (2011) 1186-1209

[19] A. Marucco, F. Turci F, L. O' Neill, H. J. Byrne, B. Fubini, I. Fenoglio, Hydroxyl density affects the interaction of fibrinogen with silica nanoparticles at physiological concentration, J. Coll. Interf. Sci. 419 (2014) 86-94

[20] I. Kokalari, R. Gassino, A.M. Giovannozzi, L Croin, E. Gazzano, E. Bergamaschi, A. M. Rossi, G. Perrone, C. Riganti , J. Ponti, I. Fenoglio, Pro- and anti-oxidant properties of near-infrared (NIR) light responsive carbon nanoparticles, Free Radic. Biol. Med. 134 (2019) 165-176

[21] W. Stöber, A. Fink, E. J. Bohn, Controlled growth of monodisperse silica spheres in the micron size range, Colloid Interf. Sci. 26 (1968) 62-69

[22] M. Monopoli, D. Walczyk, A. Campbell, G. Elia, I. Lynch, F. Baldelli, K. Dawson, Physical-Chemical Aspects of Protein Corona: Relevance to in Vitro and in Vivo Biological Impacts of Nanoparticles, J. Am. Chem. Soc. 133 (2011) 2525-2534

[23] A. Pietroiusti, M. Massimiani, I. Fenoglio, M. Colonna, F. Valentini, G. Palleschi, A. Camaioni, A. Magrini, G. Siracusa, A. Bergamaschi, A. Sgambato,

L. Campagnolo, Low doses of pristine and oxidized single-wall carbon nanotubes affect mammalian embryonic development, ACS Nano 5 (2011) 4624–4633

[24] R. K. Iler, The Chemistry of Silica, Wiley and Sons, New York, 1979

[25] A. Rimola, D. Costa, M. Sodupe, J. F. Lambert, P. Ugliengo, Silica Surface Features and Their Role in the Adsorption of Biomolecules: Computational Modeling and Experiments, Chem. Rev. 113 (2013) 4216−4313

[26] J. D. McFadyen, Z. S. Kaplan, Platelets are not just for clots, Transfusion Med. Rev. 29 (2015), 110-119

[27] Z. M. Ruggeri Z.M. Platelet adhesion under flow, Microcirculation 16 (2009) 58-83

[28] S. P. Jackson, The growing complexity of platelet aggregation, Blood J. 109 (2007) 5087-5095

[29] J. D. McFadyen, S. P. Jackson, Differentiating haemostasis from thrombosis for therapeutic benefit, Thromb Haemost. 110 (2013) 859-67

[30] L. Vroman, A. L. Adams, G. C. Fischer, P. C. Munoz, Interaction of high molecular weight kininogen, factor XII, and fibrinogen in plasma at interfaces, Blood 55 (1980) 56-159

Chapter 4

Carbon nanoparticles as model for the investigation of effect of metal ion component in the PM

4.1 Introduction

Over the last years the investigation of the exposure of human to airborne particulate matter (PM) have attracted great interest due to the deep correlation between the exposure to PM to several inflammatory diseases, involving lung or cardiovascular system. Exposure to PM air pollution is also associated with increased incidence of mortality, in particular lung cancer.[1]

Fine PM (PM2.5) is generally composed by particles in the micrometric or nanometric range, possessing a core mainly composed by elemental carbon composed by amorphous and/or graphitic structure. Similar to nanoparticles, due to their large surface area to volume, inorganic or organic contaminants, in particular Polycyclic Aromatic Hydrocarbons (PAH) and metal ions, could be detected as adsorbed species at the surface of PM.

The carbonaceous core may exhibit intrinsic properties. In fact, elemental carbon particles has been reported to have both antioxidant [2] or pro-oxidant [3] properties. The latter could be the cause of the stimulation of the inflammatory cells.

The mechanism of toxicity of PM is reported to be correlated with their ability to induce damage via various mechanisms after interaction with cells and tissues, especially related with the introduction of the adsorbed species. In particular, there are well-documented evidences that support the link between PAH and lung or skin cancer. PAH are reported to undergo biotrasformation after absorption via enzymes and certain intermediates are linked to DNA damage, mainly by the formation of adducts with lead to mutations.[4]

On the other hand, the metal distribution in airborne analysis showed that most of the toxic metals accumulate in the smallest particle (PM<2.5) [5]. Fine and ultrafine particulate matter can penetrate into the airways and reach the alveolar region, where particles come into contact with the lung tissue causing the release of metal ions into the body [6]. The delivery of redox active adsorbed metals into cells, due to the interaction of PM with living organisms, is linked to overstimulated oxidative response by generation of reactive oxygen species. Biomolecules can be strongly damaged by ROS, including proteins, lipids, and

nucleic acids.[7] A ROS-mediated mechanism can be linked with the probability of PM to enhances cardiovascular risk as: atherosclerosis, endothelial dysfunction, arrhythmias and myocardial injury.[8]

The Ambient Air Quality Directive (EU 2008) established for PM10 the annual limit of 40 μg/m3 and for PM2.5 the limit of 25 $\mu g/m^3$. Since several are the components of PM that may elicit adverse responses, EU requires Member States to make additional measurements on those components having known pathogenicity (Benzo(a)pyrene, Pb, As, Cd and Ni). Albeit other redox-active metals are believed to increase PM pathogenicity, no exposure limits for such metals exist for environmental exposure.

Transition metals such as Fe and Cu are redox active metals commonly present in the composition of the PM [9] but also present in the human body. However, in the case of prolonged exposure to PM, excessive concentration can be reached linked to toxicological effects. In particular, Cu^{+} and Fe^{2+} can catalyze the production of ROS, for examples by Fenton reaction:

$H_2O_2 + Fe^{2+} \rightarrow Fe^{3+} + \cdot OH + OH^-$

$H_2O_2 + Cu^{1+} \rightarrow Cu^{2+} + \cdot OH + OH^-$

Extensive research has been done to explore the toxicity of PM,[10], [11], [12], [13] but gabs are still present in the description of the in deep mechanism of the toxicity.

Recently, the toxicological effect of co-exposure to carbon black-metal ions, as a model material to mimic PM2.5, has been reported in vitro and in vivo.[14] Results evidenced a synergistic toxic effect the due to the co-exposure, which was higher than the effect due to exposure to carbon black and metals alone. This toxicological effect was accompanied with autophagy and lysosomal dysfunction. However, an accurate correlation of the toxicity of PM with the metal content cannot be achieved by using combustion derived nanoparticles like carbon black, since they are composed by aggregates of primary particles having a wide range of different size that in turn modulates the nanoparticles cellular uptake [15].

In this study well characterized and monodispersed carbon nanoparticles, produced following the synthesis protocol described in chapter 1 were loaded with

copper or iron in order to mimic the PM2.5 and specifically focus on the investigation of the toxicological effect to the presence of the metal ions.

4.2 Materials and methods

4.2.1 Synthesis of carbon nanoparticles

Carbon nanoparticles were obtain by hydrothermal carbonization following the protocol previously described in chapter 1 for CNP4, without modifications, named in this chapter as CNP.

4.2.2 Loading iron and copper ions on NPs surface

4.58 mL of $Fe(NO_3)_3$ solution ($8.27x10^{-3}$ M) or $CuSO_4$ solution ($3.10\ x10^{-2}$ M) were added to 49 ml of nanoparticle suspension (1.21 mg/mL) and stirred for 15 minutes.

In order to purify the NPs suspension from the metal ions not bonded to the particles, the suspension was centrifuged (11000 RPM) for 30 min (by ROTINA 380R, Hettich) and resuspended in Milli-Q water; the operation was repeated for three times. To avoid artefacts, 50 ml suspension of pristine CNP have been subjected too to the centrifuging/resuspending operations.

4.2.3 Quantification of loaded iron and copper ions

5 mL of each NPs suspension (CNP, CNP-Cu, CNP-Fe) were centrifuged (30 min, 11000 RPM) and the pellet was collected. To each pellet transferred in high-pressure Teflon bombs 1 ml H_2O_2 (30%) and 4 ml HNO_3 ultrapure (> 68 %) were added. The digestion was carried out using a microwave digestion system (Milestone microwave mls 1200 mega).

The concentration of metal ions adsorbed on NPs' surface was measured by inductively coupled plasma optical emission spectrometer (ICP-OES) (PerkinElmer Inc. Optima 2000 DV) as a courtesy of Prof. Ornella Abollino, Dept. of Chemistry, University of Torino. The amount of metal ions adsorbed on the CNPs were calculated by subtraction.

4.2.4 Hydrodynamic diameter and zeta-potential CNP

The hydrodynamic diameter (dH) distribution and the polydispersity index (PdI) of CNP in Milli-Q water was evaluated using the Dynamic Light Scattering (DLS) technique (Zetasizer Nano Z, Malvern Instruments). 0.1 ml of CNPs suspension was diluted 1:10 in ultrapure water and sonicated by probe sonication (2 min, 30%); the resulted suspension was transferred in a plastic cuvette and analysed.
In order to determine the zeta-potential of CNPs the Electrophoretic Light Scattering (ELS) technique was used (Zetasizer Nano-ZS, Malvern Instruments, Worcestershire, UK). A diluted nanoparticles suspension (0.2 mg/ml) in ultrapure water was sonicated by probe and analysed. The results are expressed as mean values of three independent experiments.

4.2.5 Preparation of the particle suspensions

All three stocks of synthetized nanoparticles suspensions (CNP 1.21 mg/ml; CNP-Fe, CNP-Cu 1.11 mg/ml) were conserved in fridge (4-8°C) for all the time. Immediately before cell treatment, particles suspensions were sonicated using an Ultrasonic water bath (Bandelin Sonorex, Berlin, Germany) for 10 min and CNP concentration was adjusted to 1.11 mg/ml.

4.2.6 Generation of Reactive Oxygen Species

The ability of nanoparticles (CNP, CNP-Fe, CNP-Cu) and of metal ions (Fe^{2+}, Fe^{3+}, Cu^{2+}) to generate hydroxyl radicals ($OH^{\cdot}$) was studied by EPR/spin trapping technique (Miniscope MS100, Magnettech, Berlin, Germany). 0.2 ml of nanoparticles suspension (1.11 mg/ml) were transferred in a glass vial with a volume of 5 ml and mixed by stirring. Then, a solution (0.25 ml; 0.176 M) of DMPO in Milli-Q water, 80 µl of ultrapure water (Milli-Q) and 0.1 ml of PBS (100 mM) were added. In the case of free metal ions experiments, 50 µl of metal solution (Fe^{3+} and Fe^{2+} 1.00 mM; Cu^{2+} 0.73 mM) were mixed with 0.1 ml of PBS (100 mM), 0.25 ml of DMPO in water (0.176 M) and 0.23 ml of Milli-Q water. The reaction time is calculated from the addiction moment of 0.1 ml of a H_2O_2

solution 0.2 M. All the samples were analysed by EPR after 5, 10, 30 and 60 minutes of continuous stirring: the synthesis solutions were transferred immediately to a 100 µl glass capillary and analysed using the EPR spectrometer. The reaction was carried out also in the absence of nanoparticles (negative control). All the experiments were repeated for three times; the obtained results are presented as means ± SDs of AUC calculated after double integration of the spectrum.

4.2.7 Scavenging activity toward hydroxyl radicals

The scavenging activity of the three nanoparticles suspensions towards hydroxyl radicals was quantified using EPR spectroscopy/spin trapping technique (Miniscope MS100, Magnettech, Berlin, Germany). Hydroxyl radicals were generated *via* Fenton reaction: Fe^{2+} was used as reducing agent of hydrogen peroxide as shown in the following equation.

$$Fe^{2+} + H_2O_2 \rightarrow Fe^{3+} + OH^- + OH^{\cdot}$$

For hydroxyl radical measurement, 0.2 ml of each particle suspension (1.11 mg/ml) were mixed with 0.1 ml of a 100 mM PBS solution and 0.25 ml of DMPO (0.176 M in H_2O). The mixture was shaken continuously al 37 °C after addition of 80 µl of a $FeSO_4$ solution (13 mM) and 0.1 ml H_2O_2 (0.2 M in H_2O). After 5, 10, 30 and 60 minutes of incubation the synthesis solutions were transferred to a 100 µl glass capillary and analysed using the EPR spectrometer. A reaction was carried out without nanoparticle suspension (only water) to be used as positive control. The results are presented as means ± SDs of three independent experiments of AUC calculated after double integration of the spectrum.

4.3 Results

4.3.1 Synthesis, purification and characterization of nanoparticles

Batches of carbonaceous nanoparticles of well-defined size and composition were prepared by a hydrothermal synthesis optimized during this studies with the goal to produce spherical nanoparticles having a diameter almost 100 nm and subsequently obtain the loading with cupper or ion ions.

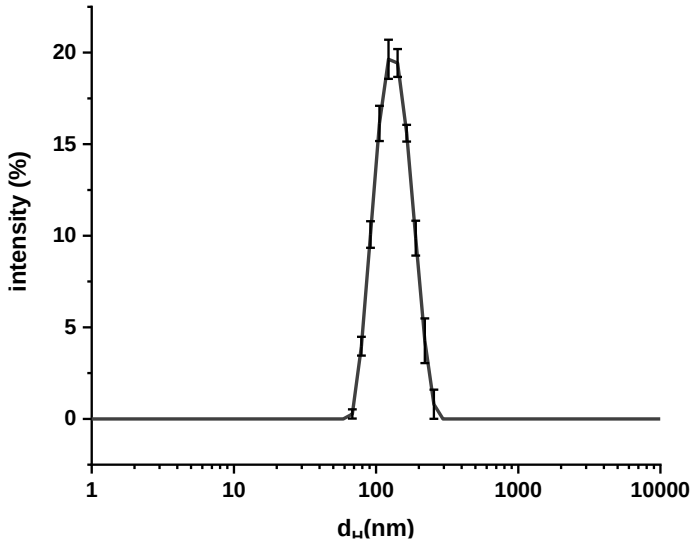

Figure 4.1. Size distribution of CNP evaluated by dynamic light scattering.

Four batches of CNP were produced for this study. The batches were mixed and the obtained suspension was firstly characterized in terms of hydrodynamic diameter, determined by Dynamic Light Scattering (DLS). In figure 4.1, the mean size distribution is reported. The mean hydrodynamic diameter resulted to be 127.2 ± 2.219 nm, with a narrow size distribution and very low Polydispersity Index (PdI) of 0.069 ± 0.009.

The synthesised nanoparticles were purified using tangential ultrafiltration, by Vivaflow® crossflow cassette. After the purification the suspension was divided in three parts: one was used as pristine nanoparticles (CNP), one was loaded with Fe^{3+} (CNP-Fe) and the last one was loaded with Cu^{2+} (CNP-Cu).

The loaded nanoparticles were characterized by Electrophoretic Light Scattering, in terms of the zeta potential, as that can be influenced by the presence of the absorbed species. As expected, the zeta potential of CNP-Fe and CNP-Cu resulted less negative compared to CNP, suggesting the absorption of positive ion, i.e. Fe and Cu ions, on the surface of the nanoparticles. Subsequently, inductively Coupled Plasma-Optical Emission (ICP-OES) technique was used for the quantification of the exact amount of metals bounded onto the nanoparticles. A summary of the characteristics of the samples is displayed in table 4.1.

Sample	Fe loaded (mg/l)	Cu loaded (mg/l)	µg metal/g NP (ppm)	Z-pot (mV)
CNP	0.186	0.102	-	-53.9 ± 0.651
CNP-Fe	13.992	0.096	$1.260x10^{-2}$	-43.7 ± 0.231
CNP-Cu	0.201	11.532	$1.039x10^{-2}$	-39.5 ± 0.608

Table 4.1. Summary of data from the characterization of loaded and non-loaded CNP.

The quantity of loaded metal expressed in mass per litre of suspension was comparable in both CNP-Fe (13.99 mg/L) and CNP-Cu (11.53 mg/L) suspensions. Both loaded quantities are relevant, considering the quantity of metal detected in the pristine CNP as impurity (Fe = 0.19 mg/L; Cu = 0.10 mg/L).
As previously reported in this thesis, each nanoparticle is decorated by $4x10^4$ acidic groups. Based on this data, the ratio between acidic groups and metal ions was calculated for CNP-Fe and CNP-Cu, respectively 7:1 for Fe ions and 10:1 for Cu ions.

4.3.2 Redox properties

The ability of the samples to generate and scavenge hydroxyl radical was investigated by EPR spectroscopy coupled with spin trapping technique, using DMPO as spin trap. As DMPO was introduced in excess in the reaction, the

intensity of the EPR spectra of the DMPO/OH· adduct is related to the amount of hydroxyl radicals present in solution.

Hydroxyl radical generation

In order to test the capacity of the nanoparticles to generate hydroxyl radicals, the suspensions were incubated with H_2O_2 and DMPO. EPR spectra of all the samples were recorded during the incubation. All samples exhibit the typical 1:2:2:1 signal of hydroxyl radical, figure 4.2. However, while CNP-Fe showed a signal only slightly more intense than the pristine CNP, an intense signal was observed in the presence of CNP-Cu, indicating the generation of large amount of HO· radicals, figure 4.3.

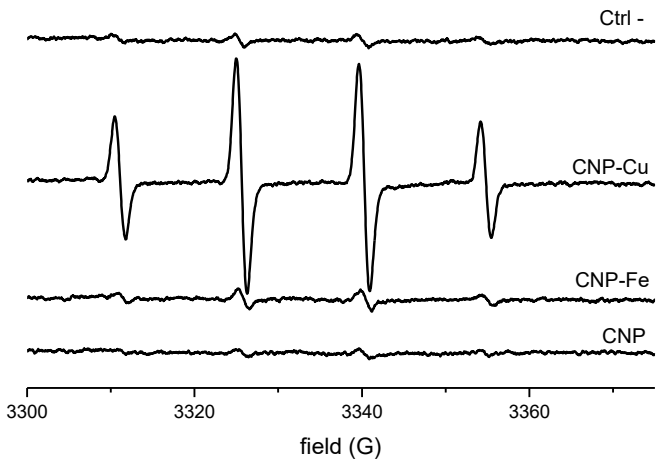

Figure 4.2. EPR spectra derived by the generation of hydroxyl radical by CNP, CNP-Cu and CNP-Fe in the presence of H2O2.

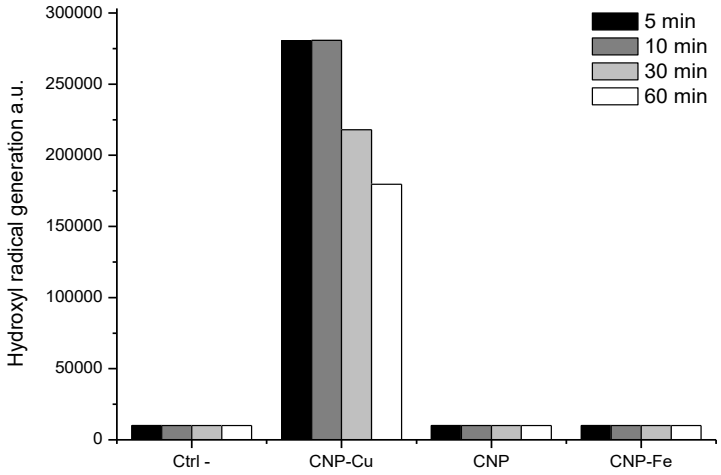

Figure 4.3. Hydroxyl radicals generation in CNP, CNP-Cu and CNP-Fe samples after 5, 10, 30 and 60 min of incubation in the presence of H_2O_2

The reaction for generation of hydroxyl radical was also performed in the presence of $CuSO_4$, having an equal copper concentration ($4.97x10^{-2}$ mM) as for the copper loaded onto nanoparticles (CNP-Cu). CNP-Cu showed a capability to generate hydroxyl radicals lower than soluble ions, figure 4.4.

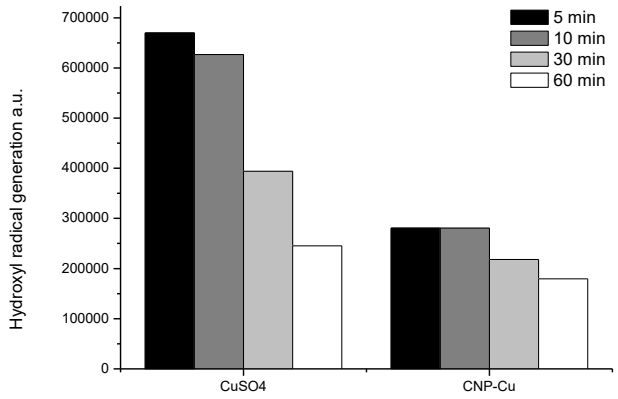

Figure 4.4. Hydroxyl radicals generation in CNP-Cu or Cu^{2+} after 5, 10, 30 and 60 min of incubation in the presence of H_2O_2

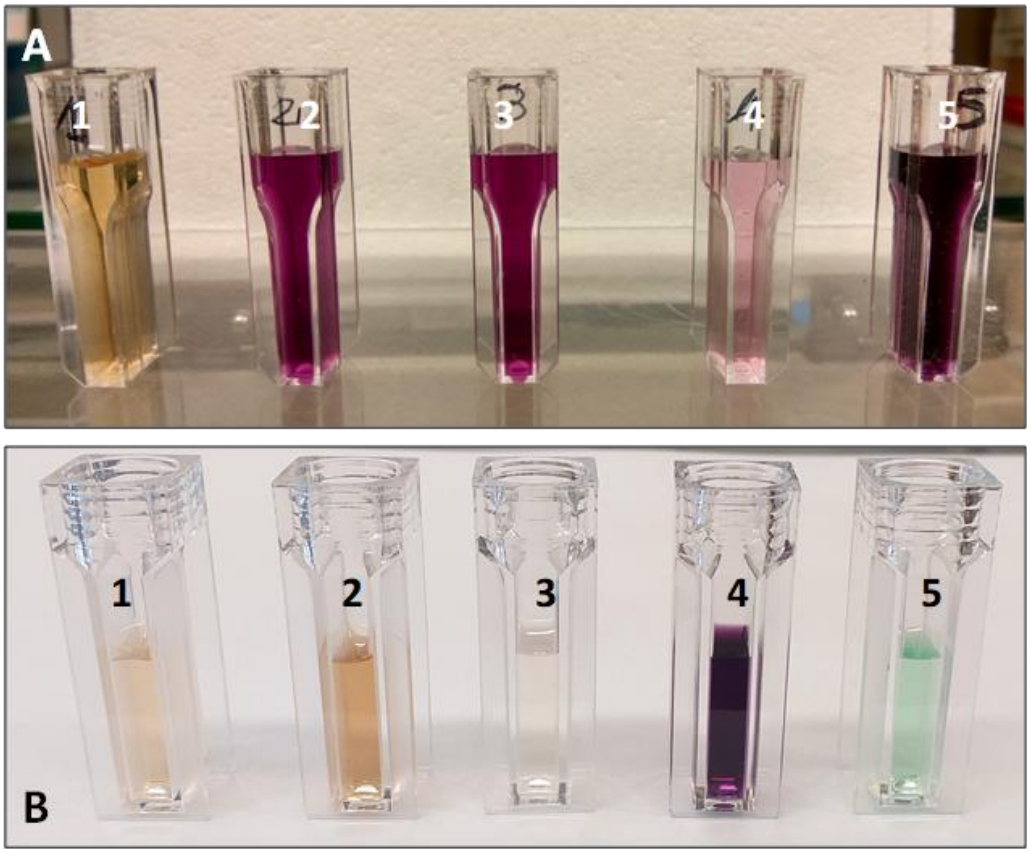

Figure 4.5. Effect of CNP on the oxidative state of iron and copper. Panel A) 1) Supernatant of pristine CNP in the presence of ferrozine; 2) Supernatant of CNP incubated with $Fe(NO_3)_3$ in the presence of ferrozine; 3) Supernatant of CNP incubated with $Fe(NO_3)_3$ in the presence of ferrozine and ascorbic acid; 4) $Fe(NO_3)_3$ in the presence of ferrozine; 5) $Fe(NO_3)_3$ in the presence of ferrozine and ascorbic acid. Panel B) 1) Supernatant of pristine CNP in PBS; 2. Supernatant of CNP + PBS + bicinconinic acid; 3. Supernatant of CNP + PBS + $CuSO_4$; 4. Supernatant of CNP + PBS + bicinconinic acid + $CuSO_4$; 5. Bicinconinic acid + $CuSO_4$.

To monitor the loading of the ions on CNP, two spectrophotometric assays here conducted, figure 4.5. In the case of iron, ferrozine was used, which is known to give a purple coordination complex when incubated with Fe^{2+}. Note that for the preparation of the loaded-CNP we used Fe^{3+} (from $Fe(NO_3)_3$), consequently a reductive agent should be necessary to reduce the iron ion from Fe^{3+} to Fe^{2+}, for

example ascorbic acid. Surprisingly, in the supernatant of the CNP after incubation with Fe^{3+} we were able to detect the purple colored complex formed between Ferrozine and Fe^{2+}, even without the presence of ascorbic acid, suggesting that CNP are able to reduce iron ions.

A similar behavior was observed for copper: when bicinconinic acid was incubated with the supernatant of the CNP after incubation with Cu^{2+} the typical purple color of the complex of bicinconinic acid with Cu^{+} was observed, confirming that CNP are able to reduce also Cu^{2+} ions.

Scavenging activity

The scavenging activity of the particles toward $HO^{\cdot}$ was also evaluated using an EPR/spin trapping technique, generating hydroxyl radicals in the presence or absence of nanoparticles.

Figure 4.6 reports the intensity of the signal during time, while in figure 4.7 are reported the EPR spectra after 60 min of incubation. After 5 min of incubation and in the presence all particles decreased the concentration of hydroxyl radicals with an effect less pronounced for CNP-Cu. However, while for pristine and loaded particles the signal decreased similarly to control suggesting a significant scavenging activity, in the presence of CNP-Cu the signal remained constant during time, suggesting the occurrence of the competitive generation of hydroxyl radicals by copper ions.

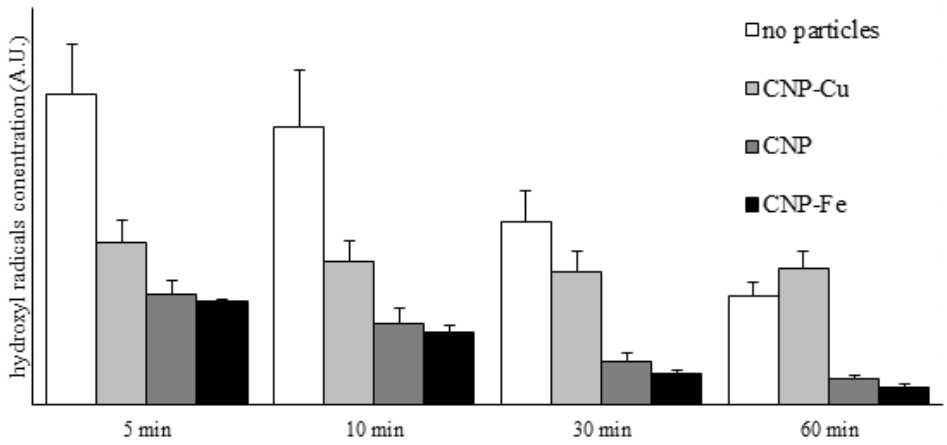

Figure 4.6. Evaluation of the scavenging activity.

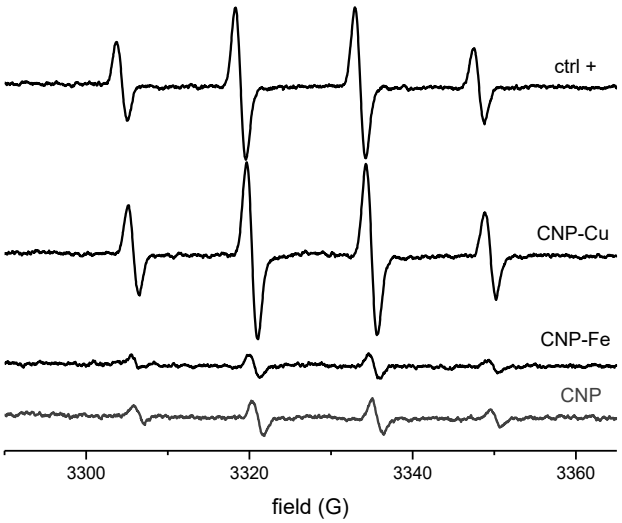

Figure 4.7. Scavenging activity of loaded and unloaded CNP after 60 min of incubation with OH radicals. EPR spectra of DMPO-OH adduct. Hydroxyl radical were generated from the Fenton reaction in absence (ctrl+) or presence (CNP-Cu, CNP-Fe, CNP) of nanoparticles.

Overall the results indicate that both metals and the carbonaceous core contribute to the surface reactivity of PM. Cu appears more pro-oxidant than iron.

The pristine and loaded nanoparticles were tested for their toxicity toward RLE-6TN epithelial cells and NR8383 alveolar macrophages in the laboratory of Dr. Roel Schins, Leibniz Institut für Umweltmedizinische Forschung (IUF), Düsseldorf, Germany by Dr. Ion Tacu during the project for his Master degree thesis. Data reveal that Cu-loaded CNP were more potent than CNP or Fe loaded CNP in inducing oxidative stress and cell death. These results well correlate with the higher surface reactivity of Cu-CNP and confirm the role of copper as determinant factor of toxicity of PM. Cu-loaded CNP were also more toxic than free ions, suggesting that CNP act as carrier of ions inside the cells.

4.4 Conclusion

The presence of copper and, at a minor extent iron, should be regarded as determinant of toxicity of PM. In the case of copper, the effect appears related to an increase of the oxidative potential of the nanoparticles in term of generation of hydroxyl radicals by Fenton-like reaction measured by EPR/spin trapping technique. The oxidative potential of the particles appears to be the resultant of the pro oxidant activity of metals and of the antioxidant activity of carbon. The overall oxidative potential appears therefore related to the content of ions, and might contribute to the variability observed among PM derived by different sources.

4.5 References

[1] S. Billet, I. Abbas, J. Le Goff, A. Verdin, V. André, P. Lafargue, A. Hachimi, F. Cazier, F. Sichel, P. Shirali, G. Garçon, Genotoxic potential of Polycyclic Aromatic Hydrocarbons-coated onto airborne Particulate Matter (PM2.5) in human lung epithelial A549 cells, Cancer Letters 270 (2008) 144-155

[2] I. Fenoglio, M. Tomatis, D. Lison, J. Muller, A. Fonseca, J.B. Nagy, B. Fubini, Reactivity of carbon nanotubes: free radical generation or scavenging activity? Free Radic. Biol. Med. 40 (2006) 1227–1233

[3] X. Liu, S. Sen, J. Liu, I. Kulaots, D. Geohegan, A. Kane, Alex A. Puretzky, C.M. Rouleau, K.L. More, G.T.R. Palmore, R.H. Hurt, Antioxidant deactivation on graphenic nanocarbon surfaces, Small 7 (2011) 2775–2785

[4] K. Straif, R. Baan, Y. Grosse, B. Secretan, F. El Ghissassi, V. Cogliano, Carcinogenicity of polycyclic aromatic hydrocarbons, Lancet Oncol. 6 (2005) 931-932

[5] K. Ravindra, R. Sokhi, R. Van Grieken, Atmospheric polycyclic aromatic hydrocarbons: Source attribution, emission factors and regulation, Atmospheric Environment 42 (2008) 2895-2921

[6] K. Midander, J. Pan, I. O. Wallinder, K. Heim, C. Leygraf, Nickel release from nickel particles in artificial sweat, Contact Dermatitis 56 (2007) 325-330

[7] R. Li, Z. Jia, M. Trush, Defining ROS in Biology and Medicine, React Oxyg Species (Apex) 1 (2016) 9-21

[8] S. A Gurgueira, J. Lawrence, B. Coull, G. G. K. Murthy, B. González-Flecha, Rapid increases in the steady-state concentration of reactive oxygen species in the lungs and heart after particulate air pollution inhalation. Environmental Health Perspectives 110 (2012) 749-755

[9] M. R. Riley, D. E. Boesewetter, A. M. Kim, F. P. Sirvent, Effects of metals Cu, Fe, Ni, V, and Zn on rat lung epithelial cells, Toxicology 190 (2003) 171-184.

[10] W.J. Gauderman, E. Avol, F. Gilliland, H. Vora, D. Thomas, K. Berhane, et al., The effect of air pollution on lung development from 10 to 18 years of age, N. Engl. J. Med. 351 (2004) 1057-1067

[11] N.L. Mills, K. Donaldson, P.W. Hadoke, N.A. Boon, W. MacNee, F.R. Cassee, et al., Adverse cardiovascular effects of air pollution, Nat. Clin. Pract. Card. 6 (2009) 36-44

[12] C.M. Somers, B.E. McCarry, F. Malek, J.S. QuinnReduction of particulate air pollution lowers the risk of heritable mutations in mice, Science 304 (2004) 1008-1010

[13] J.A. Araujo, A.E. Nel, Particulate matter and atherosclerosis: role of particle size, composition and oxidative stress, Part Fibre Toxicol., 6 (2009) 24

[14] H. Kong, K. Xia, L. Pan, J. Zhang, Y. Luo, Y. Zhang, Z. Cui, N. N. El-Sayed, A. Aldalbahi, N. Chen, A. Li, R. Tai, C. Fan, Y. Zhu, Autophagy and lysosomal dysfunction: A new insight into mechanism of synergistic pulmonary toxicity of carbon black-metal ions co-exposure, Carbon 111 (2017) 322-333

[15] A. Marucco, E. Gazzano, D. Ghigo, E. Enrico, I. Fenoglio, Fibrinogen enhances the inflammatory response of alveolar macrophages to TiO2, SiO2 and carbon nanomaterials. Nanotoxicology 10 (2016) 1-9

Chapter 5

Formulation and characterization of a novel antimicrobial nanosystem

5.1 Introduction

Infectious disease, caused by microorganisms like bacteria, viruses, parasites or fungi, remain an important cause of morbidity and mortality worldwide, especially in low-income countries. Lower respiratory infections, diarrheal diseases and tuberculosis were ranked in the top ten causes of death in the world, as reported by WHO.[1] It is estimated that around 10 million people died every year as a consequence of these diseases, amounting to 17.8% of the world-wide deaths.

Pathogenic bacteria are unicellular prokaryotic organisms that have located in their cell wall toxic molecules like peptidoglycan, (lipo)teichoic acid and lipopolysaccharide (LPS), known as endotoxins. In addition, bacteria may also secrete soluble toxic proteins, known as exotoxins. These toxins have harmful effects on the infected host, as they may destruct host cells or structures and may disturb host homeostasis. The effects of toxins on host organism may lead to disseminated intravascular coagulation, severe inflammatory response syndrome and ultimately septic shock and multiple organ failure by distorting the balance between proinflammatory and anti-inflammatory stimuli.

One way to prevent the development of infection diseases may be the inhibition of bacterial contamination and colonization, using sterilization, disinfection, or isolation. Once the bacteria have invaded the host, the aspecific and specific immunity system is activated to control the infection.

For prevention or treatment of bacterial infections, antimicrobial agents may be used. Antimicrobial agents are molecules that are (relatively) selectively toxic to bacteria, by interfering with essential bacterial metabolic processes. The discovery of antibiotics, early in the 20th century, has had a great impact on morbidity and mortality caused by bacterial infections. Penicillin was the first antibiotic discovered in 1928, but it was not until 1942 that the first patient was successfully cured from infection with penicillin. Since then, different classes of antibiotics with different modes of action were discovered or synthetized.

Since their discovery, the antibiotics have represented one of the most important therapies of modern medicine. However, despite their huge positive impact and

the advances on research over the years, the control and eradication of the infection diseases is still challenging. In particular, the antibiotic overuse and misuse have promoted the onset of antibiotic resistance with potentially devastating consequences for human health. As reported by the "*The Review on Antimicrobial Resistance",* 700000 patients died in 2014 due to antibiotic resistance. Unfortunately, the number of new antibiotic treatment is not increasing with the same rate of the problems facing old treatment alternatives. In their absence the number of new antibiotic treatments the number of death is estimated to reach 10 million by 2050.[2] The outcome of drug therapy in fighting bacterial infections is also affected by a variety of factors, including biofilms, pharmacokinetic challenges and infection site. Thus, novel antibiotic treatments are urgently needed.

Recent studies bring the attention to the development of peptide-based drugs possessing the ability of killing bacteria resistant to common antibiotics.[3] Cationic antimicrobial peptides (AMP) have been discovered more than four decades ago. They are constituted by a low number of aminoacids and are characterized by a net positive charge, generally from +2 to +9.[4] Because of their high efficacy, rapid and synergic mode of action, low susceptibility to induce drug resistance due to their multiple sites of action, AMP are less likely to promote resistance and have been proposed as valid alternative to conventional antibiotics molecules. It was shown that AMPs display a broad-spectrum action toward bacteria, fungi and viruses.[5] The ability to eradicate biofilms remain one of the most important properties of AMPs.[5] In addition, they could be used in combination with other classical drugs to increase the efficiency of the therapy.[6] However, these peptides may suffer from environmental degradation, reduced in vivo antimicrobial action, degradation by proteolytic action of different enzymes or in low pH, i.e. stomach. The loading of AMPs into nanosystems could overcome these challenges. In fact, they may provide enhanced antimicrobial efficacy and selectivity, lower cytotoxicity, extended biostability.[7] Furthermore, other possible advantages of nanoparticles as drug delivery systems also include sustained drug release, better bioavailability and biodistribution. For

example, particles larger than approximately 10 nm evade renal clearance, so that circulation half-life can be greatly increased over small molecules that are cleared by kidneys within minutes.[8] This results in improved bioavailability and tissue exposure for nanoparticle payload, along with increased accumulation at target sites. Nanoparticles can be administered via a variety of routes, such as topical, oral, ocular, parenteral (intravenous or intramuscular) and inhalation etc. Oral administration is one of the most commonly used routes for drug administration because of its non-invasive nature and the fact that it avoids the pain and discomfort associated with injections, as well as eliminating contamination.[9] Nanoparticles have the facility to cross the biological barriers and are able to deliver the active compound to the site of action. Therefore, they can be used to enhance gastrointestinal absorption of oral administrated peptides. Moreover, nanoparticles might increase the bioavailability of peptides by protecting them by the action of peptidases.

Carbon based nanomaterials (CNM) are a class of materials attracting interest as multifunctional drug delivery systems.[10], [11] In addition, many carbon nanostructures appear to be degraded in vitro, suggesting a possible rapid degradation in vivo.[12], [13] CNM comprise carbon nanotubes (CNTs), fullerene, graphene and more recently, carbon nanoparticles (CNP). The latter possesses several advantages as they are easy to prepare with a defined size and can be broadly functionalized by covalent loading or physically adsorption due to various functional groups present at the surface. Hydrothermal carbonization is an easy green chemistry method to obtain CNP. These nanoparticles form highly stable suspensions and are negatively charged, as reported in chapter 1. This make them suitable as carriers of cationic peptides that might be bonded to the nanoparticle surface by electrostatic interactions.

The aim of this study was the preparation of a nanosystem based on the conjugation of CNP with an antimicrobial peptides (AMPs) and the evaluation of its antibacterial activity. The research activity was performed at the Department of Pharmaceutical & Medicinal Chemistry at the Royal College of Surgeons in Ireland (RCSI), Dublin, in which the synthesis of the peptide was conducted under

the supervision of Prof. Marc Devocelle and Marco Monopoli. The in vitro study of the nanosystem was conducted at the Istituto Nazionale di Ricerca Metrologica (INRiM) in collaboration with Giulia Barzan and Dr. Andrea Giovannozzi.

The cationic peptide Bac8c$^{2,5\ Leu}$ has been chosen for this study, due to the low cost of production and interesting antibacterial properties. This antimicrobial peptide has been synthesized for the first time in 2014 [14] starting from the sequence of Bac2A[15], a modified variant of the natural peptide Bactenecin, a decapeptide discovered in bovine neutrophils.[16] It exhibits a low minimal inhibitory concentrations against *Staphylococcus aureus* (8 μg/mL, 6.75 μM) and other medically important bacteria as shown in table 5.1. In addition, as recently reported, Bac8c$^{2,5\ Leu}$ is highly effective in eradicating *S. aureus* biofilm infection in vitro.[3]

Bac8c - MIC (μg/mL)						
P. aerug.	*E. coli*	*S. typhim*	*S. aureus*	*S. epi.*	*E. faecalis*	*C. albicans*
8	*2*	*8*	*2*	*2*	*2*	*8*

Table 5.1. Antimicrobial characteristics of Bac8c toward important pathogens.[3]

5.2 Materials and methods

5.2.1 Synthesis, purification and characterization of the antimicrobial peptide

Isolating natural AMPs remains challenging due to low yield, high cost and undesired impurities. As an alternative, the chemical synthesis of peptides is becoming more popular in scientific reports.[17]

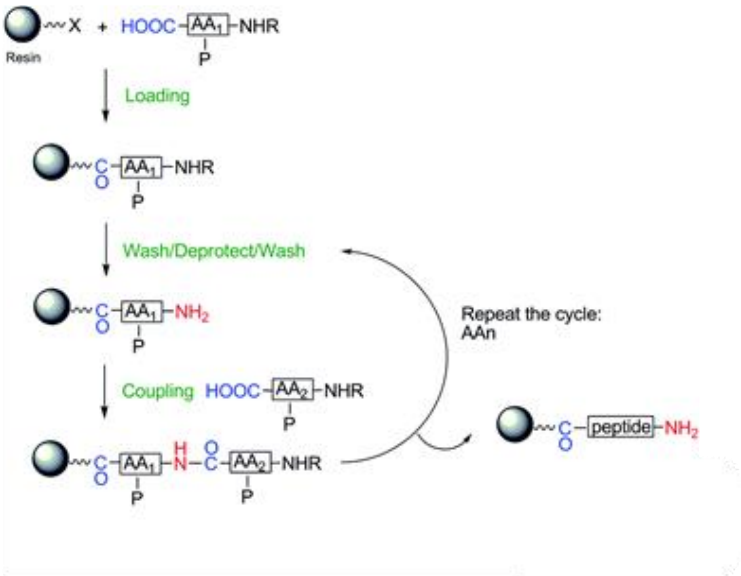

Figure 5.1. Schematic representation of the solid phase peptide method and the instrument used for this study.

In this study, the antimicrobial peptide sequence (RLWVLWRR-$CONH_2$) was synthesized at a 0.1 mmol scale, following the protocol developed by the group of Prof. Marc Devocelle.

The synthesis is based on the classical 9-Fluorenylmethoxycarbonyl (Fmoc) solid phase peptide method, using a high efficiency solid phase peptide synthesis process (HE-SPPS), with a The Liberty Blue™ Automated Microwave Peptide Synthesizer (CEM Corp., Matthews, NC, USA). A rink amide MBHA (4-methylbenzhydrylamine) resin (Novabiochem®, Germany) and L-aminoacids (Fmoc-L-Arg(Pbf)-OH, Fmoc-L-Leu-OH, Fmoc-L-Val-OH, Fmoc-L-Trp(Boc)-OH, CEM Corp., Matthews, NC, USA) were used. The couplings of amino acids

were performed in DMF using DIC/OxymaPure® activation. Fmoc removal was done using a solution of 20% piperidine in DMF. The cleavage used to deprotect and remove the peptide for the synthesis resin was performed manually at room temperature for 4 h, using a cleavage cocktail composed by 80% trifluoroacetic acid, 5% thioanisole, 5% H_2O, 5% ethanedithiol and 5% triisopropylsilan.[14]
Following cleavage, the crude peptide was precipitated and washed twice with dyethilether, dried, dissolved in H_2O, and freeze-dried. The lyophilized powder was stored at -20°C. The peptide was then purified by high-performance liquid chromatography (HPLC) (ion exchange chromatography, reversed phase (RP), equipped with PDA detector.
Buffers used were mobile-phase A (0.1% trifluoroacetic acid [TFA] in water) and mobile-phase B (0.1% TFA in acetonitrile) with a gradient of 5% to 65% buffer B in 18 column volumes (analytical) or 5 column volumes (semipreparative) with a flow rate of ml/min (analytical) or 5 ml/min (semipreparative) and single-wavelength detection at 214 nm.
The purified peptide was characterized by analytical HPLC, Shimazu CBM-20A, equipped with a Photodiode Array Detector SPD-M20A and mass spectroscopy (ESI^+-MS, Advion CMS).
In order to determine an easy and low-cost method for the quantification of Bac8c$^{2,5\ Leu}$ in aqueous solution, the peptide was tested for its possible fluoresce. It was found that the peptide is fluorescent probably due to the presence of tryptophan in its structure. The calibration curve in aqueous media was build based on the fluorescence spectra registered at different concentrations using Varian Cary Eclipse fluorescence Spectrophotometer. Fluorescence was tested in ultrapure water and PBS and in both cases it well correlate with the concentration, figure 5.2.

5.2.2 Formulation of Bac8c$^{2,5\ Leu}$@CNP

The nanosystem was prepared incubating 60 µg of Bac8c$^{2,5\ Leu}$ with 200 µg of carbon nanoparticles in 2 ml of PBS pH 7.4, 10 mM, under shaking at 400 rpm,

for 1 h (Eppendorf, Thermomixer compact). Then, the suspension was subjected to centrifugation, 18.000 rpm for 30 min, in order to prove the successful loading of Bac8c$^{2,5\ Leu}$ onto the nanoparticles surface. For this purpose, the concentration of the non-loaded peptide present in the supernatant was quantified by fluorescence spectroscopy. A solution of Bac8c$^{2,5\ Leu}$ is PBS, having the same concentration, was subjected to the identical treatment (incubation and centrifugation) and used as control.

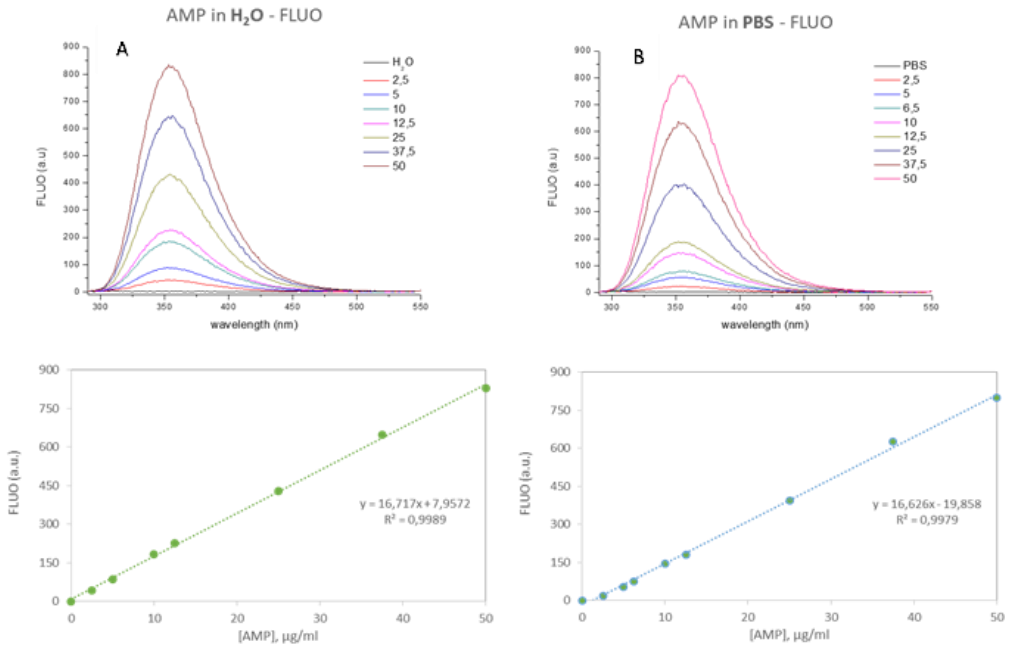

Figure 5.2. Fluorescence spectra at different concentrations and calibration curves in A. water and B. PBS pH 7.4 of the peptide.

The hydrodynamic diameter of the novel nanoformulation was characterized using dynamic light scattering technique (DLS, ZetaSizer Nano, Malvern, UK), while the zeta potential was determined using elettrophoretic light scattering (ELS, ZetaSizer Nano, Malvern, UK

5.2.3 In vitro testing of the antimicrobial activity of Bac8c^{2,5Leu}@CNP

To assess the bactericidal potential of the novel nanosystem Bac8c^{2,5Leu}@CNP over time, a time-kill kinetic assay has been performed. The assay is based on a

protocol developed by the Clinical and Laboratory Standards Institute (CLSI), USA, to evaluate the lethal activity of antimicrobial compounds [18]. Three different concentration of the nanosystem was tested, in order to have a final concentration of the Bac8c$^{2,5\ Leu}$ in the samples of 16 µg/ml, 8 µg/ml and 4 µg/ml. As shown in table 5.1, the minimum inhibitory concentration of Bac8c$^{2,5\ Leu}$ toward *Staphylococcus aureus* is 8 µg/ml.[3]

An inoculum size of 1.0 x 10^5 CFU/ml of the selected strain, *Staphylococcus aureus* SH1000, was added to 2 ml of Bac8c^{2,5Leu}@CNP suspension in PBS and incubated at 37°C, under orbital shaking at 150 rpm. Aliquots of 100 ul of the suspensions were taken at time intervals of 2, 5 and 24 h, diluted 1:10, 1:100 and 1:1000 with PBS, spreaded aseptically on nutrient Muller Hinton agar plates (Sigma Aldrich) and finally incubated for 24 h, T 37°C. A solution of Bac8c^{2,5Leu}, having the same concentration of the peptide in the nanosystem and unloaded CNP were used as controls. The colony forming unit (CFU) was determined. The graph of log CFU/ml was plotted against time.

5.3 Results and discussion

5.3.1 Synthesis and characterization of Bac8c^{2,5Leu}

Bac8c^{2,5Leu} was synthesized using microwave assisted-solid phase peptide synthesis. The peptide is composed by eight amino acids with the following sequence: R L W V L W R R - $CONH_2$.

The product of the synthesis was characterized by analytical RP-HPLC and mass spectroscopy (ESI^+-MS). Representative chromatogram is shown in figure 5.3. As noted, the peptide exhibit a retention time on 21 min, in accordance with the standard (data not shown).

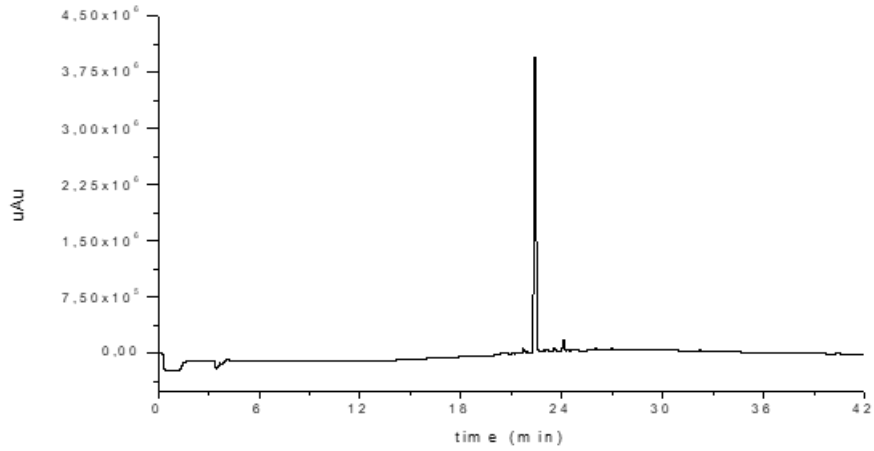

Figure 5.3. Chromatogram of purified Bac8c^{2,5Leu}, obtain by RP-HPLC, PDA detector with a wavelength of 214 nm.

Mass spectrometry confirm the synthesis of the desired peptide as displayed in figure 5.4. Given the molecular weight of the Bac8c$^{2,5\ Leu}$ equal to 1184.5 Da, in the mass spectrum of the sample the peak at 395 corresponds to the [Bac8c^{2,5Leu} +3H+]$^{3+}$, while the peak at 592 is due to the presence of [Bac8c$^{2,5\ Leu}$ +2H+]$^{2+}$ ion. The absence of other peaks in the MS spectra further indicate the successful cleavage and purification of the peptide.

Ion	m/z
[Bac8c$^{2,5\ Leu}$ +H+]1+	1184.5
[Bac8c^{2,5Leu} +2H+]2+	592
[Bac8c$^{2,5\ Leu}$ +3H+]3+	395

Table 5.2. Mass / charge ratios (m / z) of the different ions generated by Bac8c^{2,5Leu}.

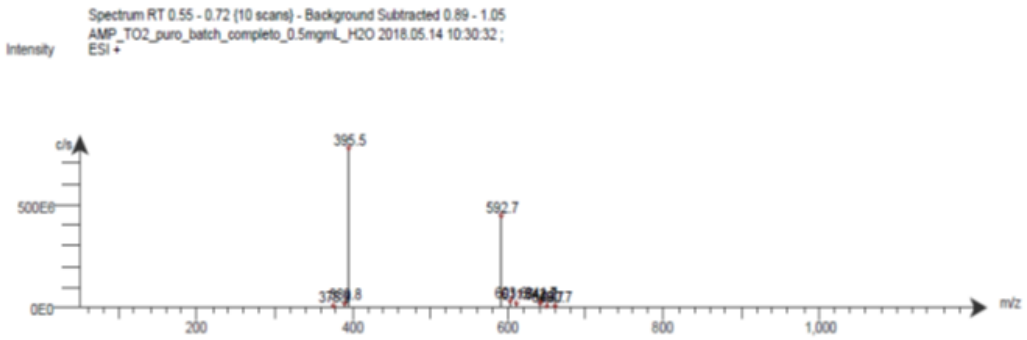

Figure 5.4. MS spectra of the purified Bac8c^{2,5Leu}.

5.3.2 Formulation of Bac8c^{2,5Leu} @CNP

The synthesized AMPs was loaded onto CNP by electrostatic interaction between the cationic peptide and the negatively charged surface. Conjugation by physical adsorption was preferred for the simpler methodology, higher yield and, possibly, higher bioavailability by respect covalent bonding. The peptide was incubated with the CNP at different concentrations in order to achieve a nanosystem stable in aqueous media and with the maximum loading capacity. In fact, loading induce a decrease of the z-potential that in turn induce the agglomeration of the nanosystem (data not shown). The optimized Bac8c^{2,5Leu} @CNP system was characterized by monodisperse particles (PDI = 0,110 ± 0,023) in the nanosize range (203,8 ± 3,537 nm) (Figure 5.5).

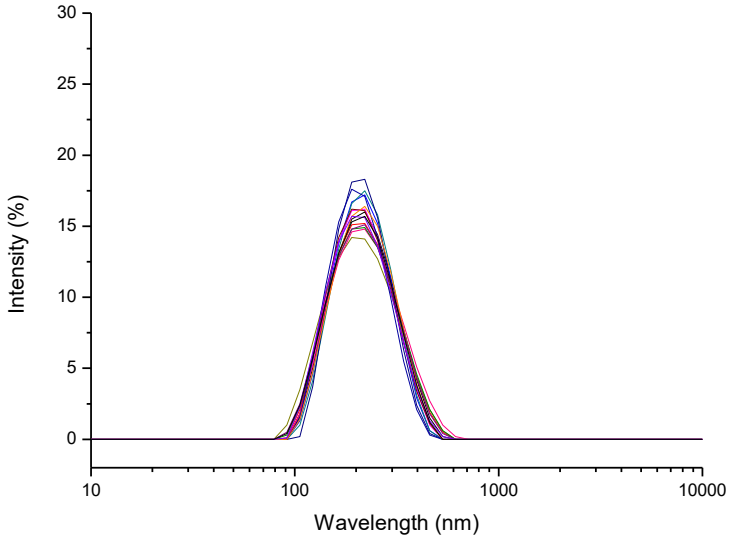

Figure 5.5. DLS intensity-weighted hydrodynamic diameter distribution of five samples (measured in triplicate) of Bac8c$^{2,5\ Leu}$@CNP following incubation.

The quantification of the loaded peptide onto CNP was performed using an indirect method. After incubation, the suspension was centrifuged in order to sediment the nanosystem. The non-bounded peptide was quantified in the supernatant by means of fluorescence. As noted in figure 5.6 the peptide is almost totally absorbed onto the nanoparticles giving a nanosystem with a final concentration of 0.3 mg Bac8c$^{2,5\ Leu}$ /mg CNP.

The strong affinity of the peptide for the CNP surface was further demonstrated by *Electron Paramagnetic Resonance* (EPR) measurements, performed by Giacomo Gariglio e Dr. Elena Ghibaudi, Department of Chemistry, University of Torino. By performing a *site-directed spin labeling* of the Bac8c$^{2,5\ Leu}$ peptide they were able to determine that Bac8c$^{2,5\ Leu}$ adsorbs strongly to the surface by electrostatic interactions at neutral pH. However, they observed a slow pH-dependent release of the peptide over time (160 h). This behavior was more pronounced at pH 4.

5.3.3 In vitro antibacterial efficacy of Bac8c$^{2,5\ Leu}$@CNP

The antibacterial activity was evaluated by using the Gram positive bacteria, S.aureus. which is responsible for a wide range of clinical infections: from superficial skin lesions to endocarditis. In addition, its antibiotic resistance is becoming increasingly common.[19] As shown in Figure 5.7, the bactericidal effects were produced in the presence of Bac8c$^{2,5\ Leu}$ alone, after 24, at concentrations of 8 μg/ml, in agreement with the MIC reported in table 5.1. When S.aureus was treated with CNP only, a higher bacterial proliferation than the control was unexpectedly observed.

This effect is peculiar of CNP since carbon based materials generally have antimicrobial properties. In fact, several studies have revealed that non isometric carbon nanomaterial as CNTs [20] or graphene/graphene oxide [21] exhibit antibacterial activity. On the other hand, some studies demonstrate that graphene and GO antimicrobial activity is due to the ability of these material to extract phospholipids from the bacterial membranes, a property that is strictly related to their needle/sheet like shape [22]. Our results support this hypothesis. Moreover, numerous studies prove the strong inhibitory effects of carbon nanotube toward bacteria [23]. Several mechanism have been proposed, in particular, the antimicrobial properties of highly purified carbon nanotubes (containing extremely low residual metal catalysts) is reported to be related with their capacity to interact with bacterial cell membrane mainly due to the characteristic cylindrical shape.[24]

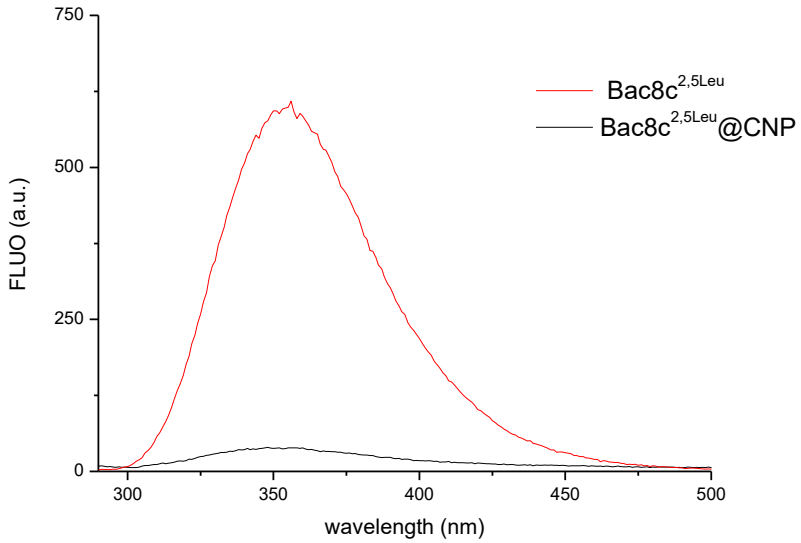

Figure 5.6. Fluorescence spectra of the supernatant of Bac8c$^{2,5\ Leu}$@CNP (black line) in comparison with the spectra of the loading solution (red line).

Note that the bacteria were grown in PBS instead of cell culture that explain also the decrease of viable cells in the control sample especially after 24h, mainly due to lack of nutrients. Likely, the CNP have been used by the bacteria as a carbon and energy source, which could explain the enhanced cellular growth. Even though no data are present in literature on the possible degradation by S.aureus of carbon nanoparticles, few studies report the capability of some bacteria community to degrade other carbon nanomaterials.[25], [26], [27]

A significant reduction of colony forming units was observed with Bac8c$^{2,5\ Leu}$@CNP after 24h of incubation at the highest concentration ($p<0.01$) , although the concentration of Bac8c$^{2,5\ Leu}$ was 2x MIC, which could be related with the effect of CNP toward bacteria.

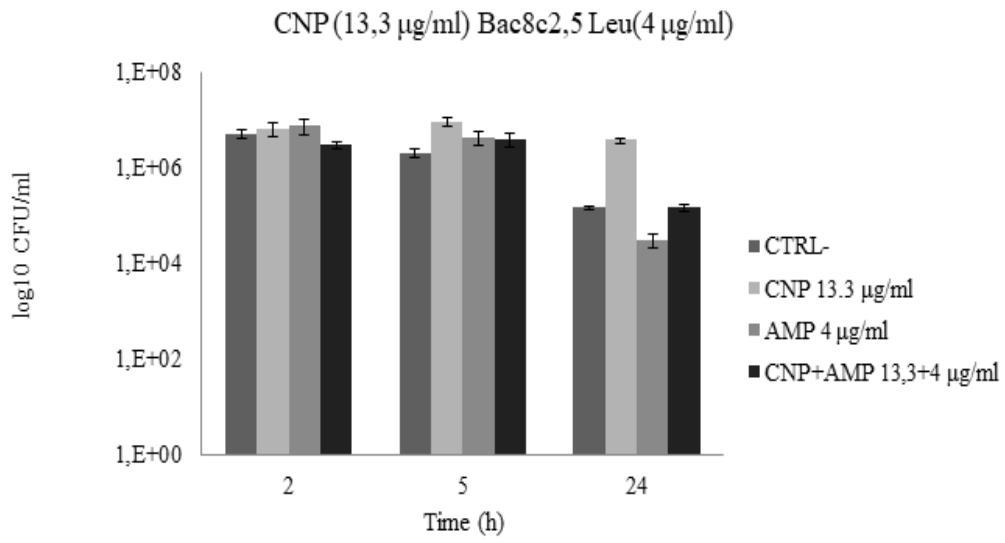
CNP (13,3 µg/ml) Bac8c2,5 Leu(4 µg/ml)
log10 CFU/ml
1,E+08
1,E+06
1,E+04
1,E+02
1,E+00
2
5
24
Time (h)
CTRL-
CNP 13.3 µg/ml
AMP 4 µg/ml
CNP+AMP 13,3+4 µg/ml

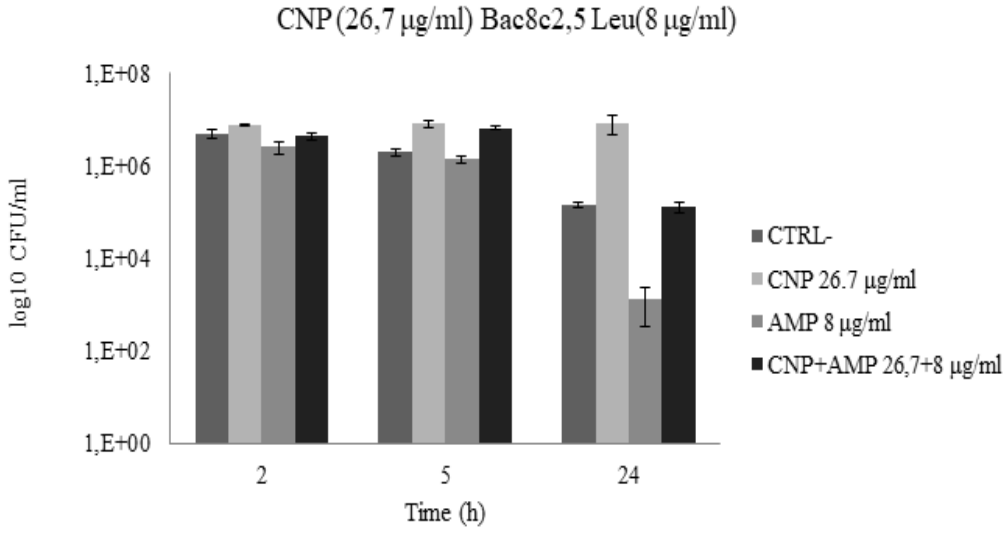
CNP (26,7 µg/ml) Bac8c2,5 Leu(8 µg/ml)
log10 CFU/ml
1,E+08
1,E+06
1,E+04
1,E+02
1,E+00
2
5
24
Time (h)
CTRL-
CNP 26.7 µg/ml
AMP 8 µg/ml
CNP+AMP 26,7+8 µg/ml

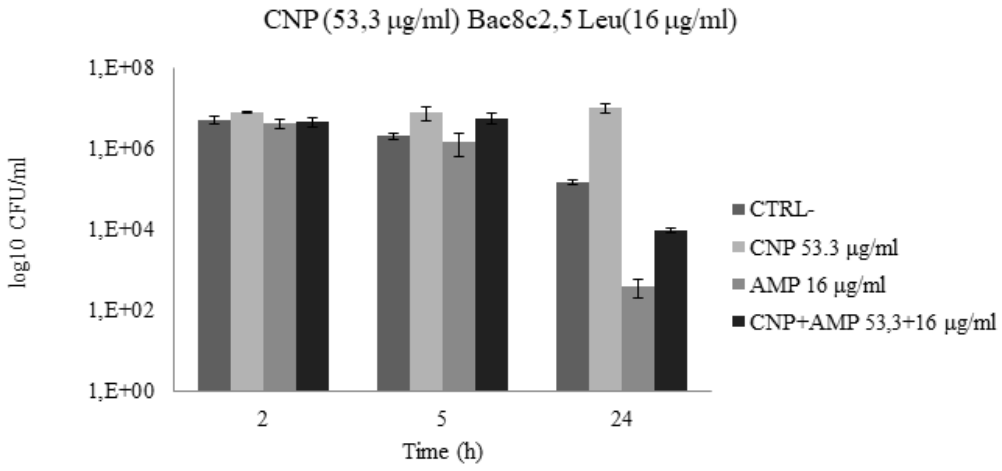

Figure 5.7. Effect of Bac8c$^{2,5\ Leu}$ @CNP on S.aureus SH1000. Bac8c$^{2,5\ Leu}$@CNP was tested at three different concentration (13.3, 26.7 and 53.3 µg/ml) correspondent to 4, 8 and 16 µg/ml of peptide concentration. Bac8c$^{2,5\ Leu}$ and CNP were used control. Efficacy of the nanosystem was observed at the highest concentration after 24 h of incubation ($p<0.01$).

Further studies are indispensable to unveil the mechanism of action of the nanosystem and in particular whether Bac8c$^{2,5\ Leu}$ @CNP is internalized by the cell. In fact, the main mechanism of action of the peptide is reported to be linked with the prokaryotic membrane depolarisation and cytoplamic permeabilization by the free peptide [28]. In the present case, the peptide is poorly released by the nanosystem at pH 7.4, as inferred by fluorescence and SDSL-EPR data, suggesting a possible mechanism involving the uptake of the nanosystem.

5.4 Conclusion

The physical conjugation of Bac8c$^{2,5\ Leu}$, a promising antimicrobial agent with potent effect toward a wide range of important pathogenic bacteria, with CNP generates a novel nanosystem that exhibited good antibacterial activity against S.aureus. On the other hand, loading of the Bac8c$^{2,5\ Leu}$ on the nanocarrier could increase stability to degradation toward proteases, suggesting a better bioavailability of Bac8c^{2,5Leu} in vivo. In perspective, the combination of the antimicrobial action of the peptide with the PT and PD properties of CNP described in the chapter 1 could probably enhance the therapeutic outcome of the Bac8c$^{2,5\ Leu}$@CNP.

5.5 References

[1] The World health report 2016: health systems: improving performance. World Health Organization, Geneva.

[2] Wellcome Trust and UK Department of Health, 2016, Review on Antimicrobial Resistance

[3] M. Zapotoczna, É. Forde, S. Hogan, H. Humphreys, J. P O'Gara, D. Fitzgerald-Hughes, M. Devocelle, Eoghan O'Neill, Eradication of Staphylococcus aureus Biofilm Infections Using Synthetic Antimicrobial Peptides, J Infect Dis. 215 (2017) 975-983

[4] L. Lombardi, G. Maisetta, G. Batoni, A. Tavanti, Insights into the antimicrobial properties of hepcidins: advantages and drawbacks as potential therapeutic agents, Molecules, 20 (2015), 6319-6341

[5] R. E. Hancock, H. G. Sahl HG, Antimicrobial and host-defense peptides as new anti-infective therapeutic strategies, Nat Biotechnol. 24 (2006) 1551-1557

[6] P. Y. Chung, R. Khanum, Antimicrobial peptides as potential anti-biofilm agents against multidrug-resistant bacteria, J Microbiol Immunol Infect, 50 (2017) 405-410

[7] Marc Devocelle, Targeted antimicrobial peptides, Front. Immunol 3 (2012) 309

[8] A. Nancy, C. Monteiro-Riviere, L. Tran, Nanotoxicology: Progress toward Nanomedicine, Second Edition. New York: CRC Press, 2016

[9] L. Kagan, A. Hoffman, Systems for region selective drug delivery in the gastrointestinal tract: biopharmaceutical considerations, 5 (2008) 681-692

[10] G. Xu, S. Liu, H. Niu, W. Lva, R. Wu, Functionalized mesoporous carbon nanoparticles for targeted chemo-photothermal therapy of cancer cells under near-infrared irradiation, RSC Adv. 4 (2014) 33986-33997

[11] G. Liu, H. Shen, J. Mao, L. Zhang, Zhen Jiang, Tao Sun, Q. Lan, Z. Zhang, Transferrin Modified Graphene Oxide for Glioma-Targeted Drug Delivery: In Vitro and in Vivo Evaluations, ACS Appl. Mater. Interfaces 5 (2013) 6909-6914

[12] V. E. Kagan, N. V. Konduru, W. Feng, B. L. Allen, J. Conroy, Y. Volkov, I. I. Vlasova, N. A. Belikova, N. Yanamala, A. Kapralov, Y. Y. Tyurina, J. Shi, E. R. Kisin, A. R. Murray, J. Franks, D. Stolz, P. Gou, J. Klein-Seetharaman, B. Fadeel, A. Star, A. A. Shvedova, Carbon nanotubes degraded by neutrophil myeloperoxidase induce less pulmonary inflammation, Nat Nano 5 (2010) 354–359

[13] M. Zhang, M. Yan, C. Bussy, S. Iijima, K. Kostarelos, Masako Yudasaka, Biodegradation of carbon nanohorns in macrophage cells, Nanoscale 7 (2015) 2834-2840

[14] É. Forde, H. Humphreys, C. M. Greene, D. Fitzgerald-Hughes, M. Devocelle, Potential of Host Defense Peptide Prodrugs as Neutrophil Elastase-Dependent Anti-Infective Agents for Cystic Fibrosis, Antimicrob Agents Chemother. 58 (2014) 978-85

[15] Kai Hilpert, Rudolf Volkmer-Engert, Tess Walter & Robert E W Hancock, High-throughput generation of small antibacterial peptides with improved activity, Nature Biotechnology 23 (2005) 1008–1012

[16] D Romeo, B Skerlavaj, M Bolognesi, R Gennaro, Structure and bactericidal activity of an antibiotic dodecapeptide purified from bovine neutrophils, 263 (1988) 9573-9575

[17] C. W. Diehnelt, Peptide array based discovery of synthetic antimicrobial peptides. Front. Microbiol. 4 (2013) 402

[18] A. L. Barry, W. A Craig, H. Nadler, L. B. Reller, C. C Sanders, M. Jana, NCCLS document M26-A Swenson. 1999. 'Methods for determining bactericidal activity of antimicrobial agents; approved guideline', 19.

[19] S. Y. Tong, J. S. Davis, E. Eichenberger, T. L. Holland, V. G. Fowler, Staphylococcus aureus infections: epidemiology, pathophysiology, clinical manifestations, and management, Clin Microbiol Rev. 28 (2015) 603-661

[20] S. Kang, M. Pinault, L. D. Pfefferle, M. Elimelech, Single-Walled Carbon Nanotubes Exhibit Strong Antimicrobial Activity, Langmuir 23 (2007) 8670-8673

[21] Zhao C., Deng B., Chen G., Lei B., Hua H., Peng H., Yan Z. Large-area chemical vapor deposition-grown monolayer graphene-wrapped silver nanowires for broad-spectrum and robust antimicrobial coating. Nano Res. 9 (2016) 963–973

[22] Y. Tu, M. Lv, P. Xiu, T. Huynh, M. Zhang, M. Castelli, Z. Liu, Q. Huang, C. Fan, H. Fang, R. Zhou, Destructive extraction of phospholipids from Escherichia coli membranes by graphene nanosheets, Nature Nanotechnology 8 (2013) 594–601

[23] A. Al-Jumaili, S. Alancherry, K. Bazaka, M. V. Jacob, Review on the Antimicrobial Properties of Carbon Nanostructures, Materials (Basel) 10 (2017), E1066

[24] S. Kang, M. Pinault, L. D. Pfefferle, M. Elimelech, Single-Walled Carbon Nanotubes Exhibit Strong Antimicrobial Activity, Langmuir 23 (2007) 8670-8673

[25] Y. You, K. K. Das, H. Guo, C. W. Chang, M. Navas-Moreno, W. Chan, P. Verburg, S. R. Poulson, X. Wang, B. Xing, Y. Yang, Microbial Transformation of Multiwalled Carbon Nanotubes by Mycobacterium vanbaalenii PYR-1, Environ Sci Technol. 21 (2017) 2068-2076

[26] L. Zhang, E. J. Petersen, M. Y. Habteselassie, L. Mao L, Q. Huang, Degradation of multiwall carbon nanotubes by bacteria, Environ Pollut. 181 (2013) 335-359

[27] M. Chen, X. Qin, G. Zeng, Biodegradation of Carbon Nanotubes, Graphene, and Their Derivatives, Trends Biotechnol 35 (2017) 836-846

[28] E. C. Spindler, J. D. Hale, T. H. Giddings, R. E. Hancock, R. T. Gill, Deciphering the mode of action of the synthetic antimicrobial peptide Bac8c, Antimicrob Agents Chemother. 55 (2011) 1706-1716

Chapter 6

Synthesis and characterization of iron oxide-carbon core-shell nanohybrids

6.1 Introduction

In last years, increasing developments were observed in the field of nanosized magnetic particles, as they offer exciting new opportunities in the biomedical field including magnetic resonance imaging (MRI), hyperthermic treatment for malignant cells, site-specific drug delivery, cells labelling and magnetic separation.[1]

This quickly expanding number of applications involved in many cases a very interesting property of magnetic nanoparticles called superparamagnetism. When a magnetic material is in the form of particles smaller then a certain size (nanosize range) can exhibit this behavior. As shown in Figure 6.1, these nanoparticles are single-domain particles, in fact their total magnetic moment can be regarded as one giant magnetic moment, composed of all the individual magnetic moments of the atoms which form the nanoparticle. In absence of a magnetic field, domains are randomly oriented, while in a magnetic field they tend to align. In small-sized single-domain magnetic nanoparticles, heat generation comes from magnetic spin relaxation: once NPs are located in an alternating magnetic field (AMF), the magnetization reversal process occurs by overcoming an energy barrier. Since the magnetic nanoparticles prefer to align in a specific direction, energy is required to rotate the magnetization from that direction. Through the repeated alignments and relaxations of magnetic spins, energy dissipates through heat.[2]

This property may be exploited for tumor ablation: once the magnetic nanoparticles are administrated, usually injected intratumorally or intravenously, and preferentially accumulated at the tumor site [3]. The concurrent external magnetic field application can possibly ablate the tumor in a remote and noninvasive manner.

Pure metals (Fe, Co, Ni) possess the highest saturation magnetization, however, they are not attractive as they possess high toxicity and they are very sensitive to oxidation.[4] On the contrary, small iron oxide nanoparticles have been applied in biomedical applications for about 50 years, as they are a good

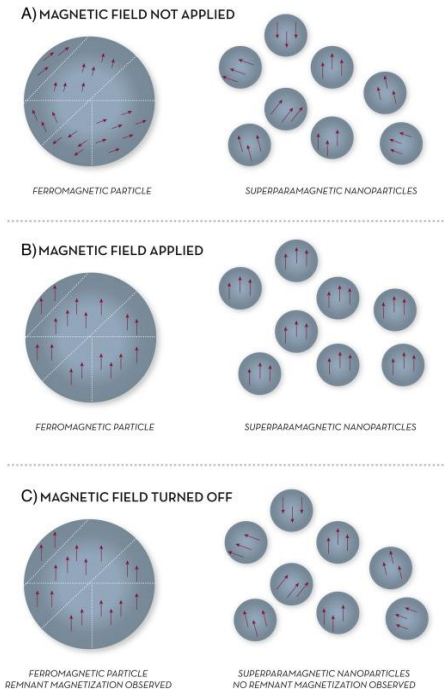

Figure 6.1. Differences between superparamagnetic and ferromagnetic particles in absence or presence of magnetic field. Modified from [5]

compromise between magnetic susceptibility, chance of functionalization, biodegradability and biocompatibility. [6], [7], [8]

Besides superparamagnetism, tailoring of the physicochemical properties such as size shape and surface properties, is crucial for the successful biomedical application of magnetic nanoparticles. Different synthetic strategies can be used for the production of magnetic nanoparticles. Co-precipitaion is almost the easiest and most economic water based route of synthesis performed in mild reaction conditions, which consists in the coprecipitation of ferrous (Fe^{2+}) and ferric (Fe^{3+}) ions in basic pH. However, the major limitations include polydispersity and aggregation of nanoparticles. Thermal decomposition of organometallic compounds offers the possibility to produce monodisperse magnetic NP and precisely control their size and morphology. One other hand, the major restriction involved the use of non-biocompatible precursors and toxic organic solvents. Hydro/solvothermal synthesis is a facile way of synthesis performed in high

temperatures in aqueous solution (generally in the range from 180 to 250 °C) and usually self-generating pressure. Hydrothermal derived nanoparticles have good crystallinity and generally a fine size distribution.

NPs can be classified based on single or multiple materials into simple and core/shell or composite nanoparticles. In general, simple nanoparticles are made from a single material, while composite and core/shell particles are composed of two or more materials. The core/shell NPs are a type of biphasic materials which have an inner core (inner material) structure and a shell (outer layer material). (figure 6.2) They can be included different combinations in close interaction, consisting inorganic/inorganic, inorganic/organic, organic/inorganic and organic/organic materials. Depend on the required application, can be chosen the shell material of the core/shell nanoparticle. The most common type of core/shell nanoparticles are concentric spherical which a spherical core particle is coated entirely by a shell of a different material.

A particularly interesting kind of core-shell NPs are those composed by carbon and a magnetic material (magnetic carbon nanostructure MCNs). They can be classified in two families, carbon encapsulated magnetic nanoparticles and carbon nanostructures decorated with MNPs

These structures may find several applications in biomedicine. Though carbon-coating will cause the reduction of saturation magnetization, carbon functionalized iron oxide NPs have many advantages compared with the uncoated iron oxide NP, like higher chemical stability, as the coating prevents the NPs agglomeration caused by van der Waals attraction, thermal stability, capability of anchoring drug molecules through covalent bonding [9].

Coating also affect the biocompatibility of magnetic CNP (9). In fact, iron oxide nanoparticles are expected to be degraded in endosomes, releasing iron ions that enter in the cellular iron homeostasis system, being incorporated by ferritin [10]. However, depending by the amount and kinetic of release iron ions can induce release of reactive oxygen species (ROS) that in turn induce oxidative stress to cells[11].

Several coating methods have been developed, including in situ coating (carried out during synthesis) and post-synthesis coating, which is known as core-shell NPs[12], the first one has several advantages over the second, primarily reduces aggregation and improves the size distribution of the products, due to immediate coating of the particles and fewer processing procedures.

Wang and collaborators described a novel method to synthetize magnetic FeOx@C nanohybrids. The synthesis consisted in the hydrothermal carbonization of ferrocene and leads superparamagnetic magnetite nanoparticles (mean diameter around 5-10 nm) embedded in a porous carbonaceous matrix [13], [14]. In two more recent studies, the same Authors produced doxorubicin loaded nanohybrids in which the drug release may be induced by exploiting the photothermal effect in response to NIR light or by decreasing the pH [15]. The Authors tested the efficacy of these drug delivery systems on two different models, a mouse melanoma cell line (B16F10) [13] and a human prostate cancer cell line (DU145) [15]. They observed an effective drug release induced by the two kinds of stimuli, accompanied by a cytotoxic effect. These magnetic nanoparticles appear then to be promising platforms that may improve the efficacy of several therapeutic agents.

However, Wang and co-authors did not provide data on the safety of this kind of material, on the long-term fate of C@FeOx into the body and on their possible biodegradation.

The aim of this study was to investigate the safety and biodegradation of C@FeOx in a view of a possible medical use. In fact, the carbon shell of C@FeOx share with CNP described in the previous chapter a similar composition and, possibly, bulk and surface structure. Therefore, we were interested to investigate if such materials were similarly degraded by endogenous oxidants and exhibit similar redox properties. This study was performed in collaboration with the Centre for BioNano Interactions (CBNI), University College of Dublin, Prof. Kenneth Dawson group.

Firstly, we synthesized C@FeOx_1 as described in the following paragraph. The sample was characterized in terms of size and zeta potential and then sent to the

collaborators for analysis where the morphology and bulk structure was revealed by TEM and *in vitro* evaluation of the safety in dark toward A549 cells was assessed. In a subsequent attempt to synthesized smaller nanohybrides, we succeed to obtain C@FeOx_2. The sample was characterized in terms of size, Z-potential, scavenging capability toward ROS and degradation. At CBNI, TEM imaging and in vitro toxicity profile of C@FeOx_2 were performed.

6.2 Materials and methods

6.2.1 Synthesis of C@FeOx nanohybrids

Solvothermal synthesis was used for the synthesis of C@FeOx as previously reported [16], with modification. Two different protocols were developed. C@FeOx_1 was synthesized as following:

100 mg of ferrocene were dissolved in 30 ml of acetone and sonicated with a probe sonicator (Bandelin Sonopuls HD 3100) for 30 minutes in an ice bath. The ferrocene solution must be prepared in the dark, as it is very sensitive to the light. Then 2.5 ml of hydrogen peroxide 30% w/v were slowly dropped in the ferrocene solution, under magnetic stirring at room temperature, and then kept under vigorous stirring for 30 minutes. The so obtained solution was transferred in a 50 ml stainless steel Teflon lined autoclave (Figure 10) and kept in oven at 200° C for 24 hours. The final product was magnetized for 10 min in a magnetic field of 0.50 T generated by Electron Paramagnetic Resonance (EPR).

Nanoparticles were then purified in order to remove the ferrocene in excess: the suspension was centrifuged at 6000 rpm for 30 min and the supernatant was discarded; the compact pellet consisting in nanoparticles was re-suspended in acetone. The washing process was repeated three times, until the supernatant appeared colorless instead of yellow.

The synthesis of the second type of C@FeOx (C@FeOx_2) was similar to what previously described for C@FeOx_1. In that case, the amount of hydrogen peroxide was reduce to 0.25 ml with the target to reduce the size of the nanoparticles.

6.2.2 C@FeOx physicochemical characterization

Hydrodynamic diameter of C@FeOx_1 and C@FeOx_2 was evaluated by dynamic light scattering (Nano ZS Malvern Instruments, UK). The measurement was performed immediately after the purification process on samples diluted 1:2

with ultrapure water, sonicated in an ice bath for 2 mins at 30% of amplitude with a probe sonicator.

Zeta-potential value was determined by Electrophoretic Light Scattering (Nano ZS Malvern Instruments, UK). The ζ-potential was determined in a pH range 10-2. The samples were suspended in ultrapure water at the concentration of 0.8 mg/ml and the pH of the nanoparticle suspensions adjusted with 0,1M NaOH, 0,01M HCl and 0,001M HCl (purchased from Sigma-Aldrich).

6.2.3 Scavenging capability toward OH radicals

The scavenging activity of C@FeOx_2 towards hydroxyl radicals was evaluated using electronic paramagnetic resonance (EPR)/spin trapping technique (Miniscope MS100, Magnettech, Berlin, Germany). The following parameters were applied: B0 fields = 3344,14 G; sweep = 119,19 G; sweep time = 80 sec; smooth = 0,00 sec; steps = 4096; n°pass. = 2; modulation = 1000 mG; MW atten. = 7 dB; gain = 2E 2 / 9E 2.

A volume of 0.3 ml of suspension of C@FeOx_2 (3.33 mg/ml in phosphate buffer 0.01 M, pH 7.4) was transferred in a cuvette and stirred in the dark. 0.25 ml of a solution 0.15 M of 5,5-dimethyl-1-pyrroline N-oxide (DMPO) in water and 0.08 ml of a solution 13 mM of $FeSO_4$ were added. The reaction was started by adding 0.1 ml of a solution 0.2 M of H_2O_2. The reaction was also repeated in absence of C@FeOx_2 as control. The reference sample consisted in glucose-derived nanoparticles synthesized as described in chapter 1. EPR spectra were measured on the suspension after 10 min of incubation in the dark. In the case of C@FeOx_2, the suspension was filtered after the incubation and the spectrum was immediately recorded.

6.2.4 Degradability of C@FeOx_2

Degradability of C@FeOx_2 was investigated *in vitro* by employing a solution of hypochlorite and/or hydrogen peroxide, the two main oxidants present in the phagosome. The final concentration of H_2O_2 or NaClO were

200μM or 2000 μM. Samples consisted of 1 mg of C@FeOx_2 dispersed in PBS, 10 mM. The final volume of the sample tubes (10 mL) was kept constant for all solutions. The pH of the solution was set at 4.5. The samples were incubated for 14 days, at 37°C and NaClO or H_2O_2 were added daily to keep a constant concentration of the oxidants.

The degradation was evaluated by visual observation and UV-Vis spectroscopy.

6.3 Results and discussion

6.3.1 Synthesis and physicochemical characterization

Solvothermal synthesis route has been employed for the synthesis of the C@FeOx using ferrocene as precursor and hydrogen peroxide [16]. Starting from the protocol described by Wang et al.[16] different synthetic parameters were attempted to optimize the synthesis. When the volume of hydrogen peroxide was reduced, the diameter of the nanohybrides approaches the desired size.

In both case monodispersed particles in a nanosize range was obtained as shown by the dH distribution derived from three independent batches of C@FeOx_1 and C@FeOx_2 (Figure 6.3). C@FeOx_2 nanohybrids had a lower diameter, better size distribution and reproducibility.

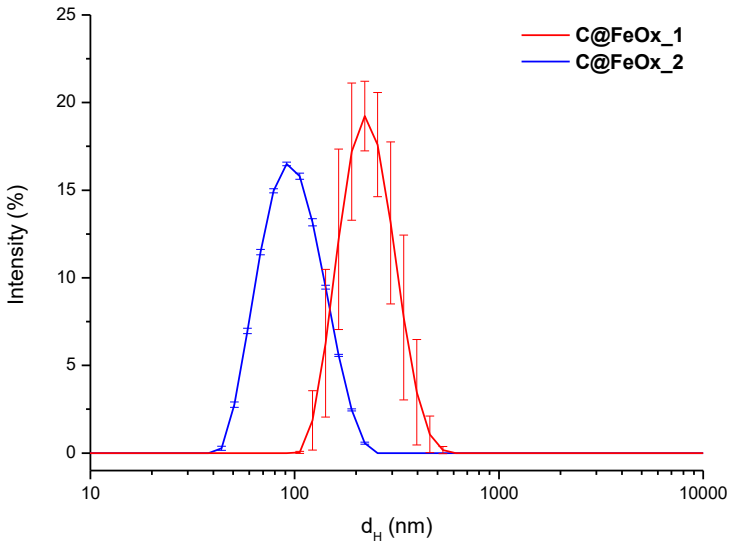

Figure 6.3. Intensity-based size distribution of purified C@FeOx samples.

The morphology and structure of the nanohybrids was investigated with TEM. In both cases spherical nanoparticles with a carbon core and iron oxide shell were obtain. Beside the geometric diameter in accordance with DLS data, differences

were observed also in the thickness of carbon shell, which appears thicker in the case of C@FeOx_2, as shown in figure 6.4.

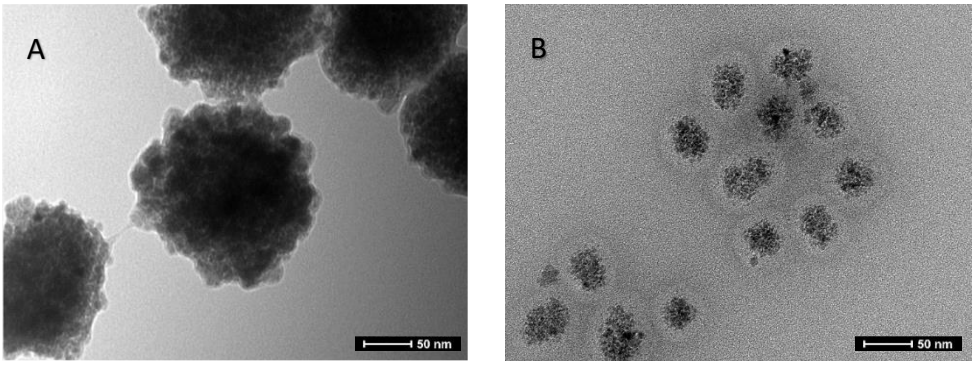

Figure 6.4. TEM micrograph of nanohybrids at the same magnification provided by CBNI group. A) C@FeOx_1, B) C@FeOx_2.

Figure 6.5 reports the ζ-potential values as a function of pH range from 2-10. At physiological pH has a Zeta potential lower than -40 mV, suggesting a good stability of the suspension. Indeed, colloids having zeta potential from ±30 to ±60 mV possess good stability due to high electrostatic repulsion between particles, which prevent agglomeration. Both samples exhibit a negative zeta potential, which increased with increasing of the pH, suggesting the presence of acidic groups on the surface due to the characteristics of the carbon shell. The absence of positive values at low pH indicate that iron oxide NPs are completely embedded by the carbon shell.

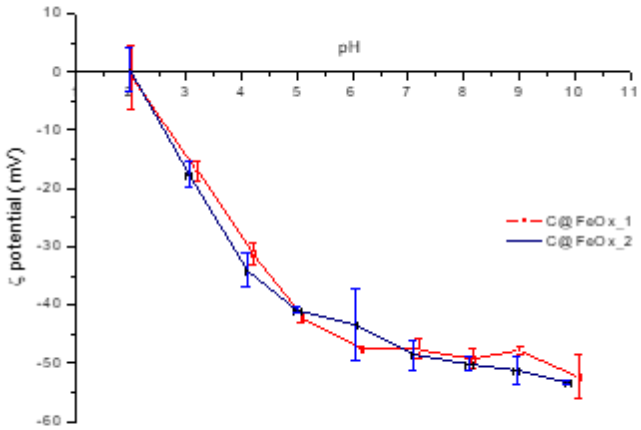

Figure 6.5. Zeta potential versus pH curves for C@FeOx suspended in water.

6.3.2 Scavenging capability toward hydroxyl radicals

As previously reported, some carbon nanostructures demonstrate antioxidant activity due to their ability to scavenge ROS.[17], [18], [19] In addition, in chapter 1, the scavenging activity of CNP, a relatively new class of saccharide-derived carbon nanoparticles, toward the most aggressive ROS, hydroxyl radicals (HO·), was described in details. Given the structure of C@FeOx_2, in which a continuous and thick shell of carbon covers the magnetic core, we investigate the possibility to scavenge hydroxyl radicals in dark conditions. EPR spectroscopy coupled with spin trapping technique was employed for detection and quantification of HO·, generated by the Fenton reaction as described in the method section. The high amount of radicals generated in this conditions is proved by the intense (1:2:2:1) four-line EPR signal recorded, correspondent to the DMPO/HO· adduct (aN=aH= 14.6 G) (Figure 6.6). CNP was used as reference sample. EPR signal decreased in the case of CNP. However, when the reaction was performed in the presence of the C@FeOx_2, the signal was completely suppressed suggesting a higher scavenging capability compared to the reference samples. The higher activity observed could be related to the

higher crystallinity of the nanohybrids compared to CNP and due to addition of the radical to the backbone or electron transfer. The process related to hydrogen donation from the functional groups exposed to the surface to the hydroxyl radicals could be excluded since the two samples exhibit similar abundance of surface functionalities as suggested by the similar z-potential values at pH 7.4, as reported in figure 6.7.

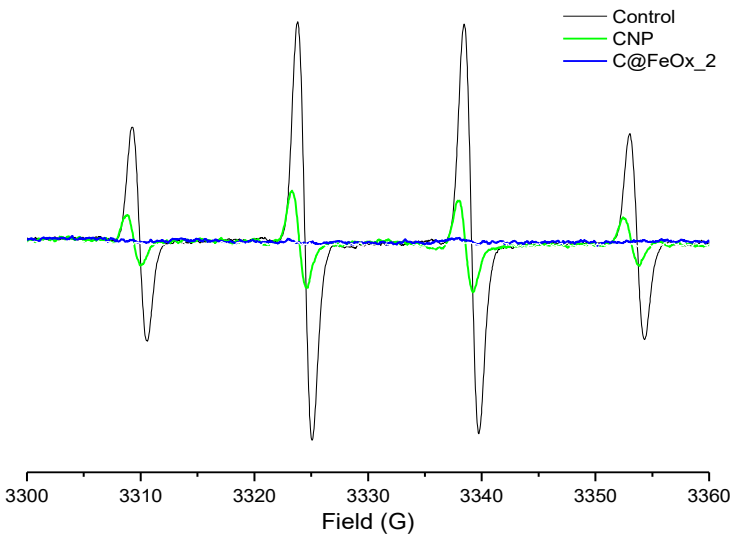

Figure 6.6. Scavenging activity of C@FeOx toward hydroxyl radicals. EPR spectra recorded following the generation of hydroxyl radicals by Fenton reaction in the absence (blackline) or in the presence of CNP(green line) or C@FeOx (blue line).

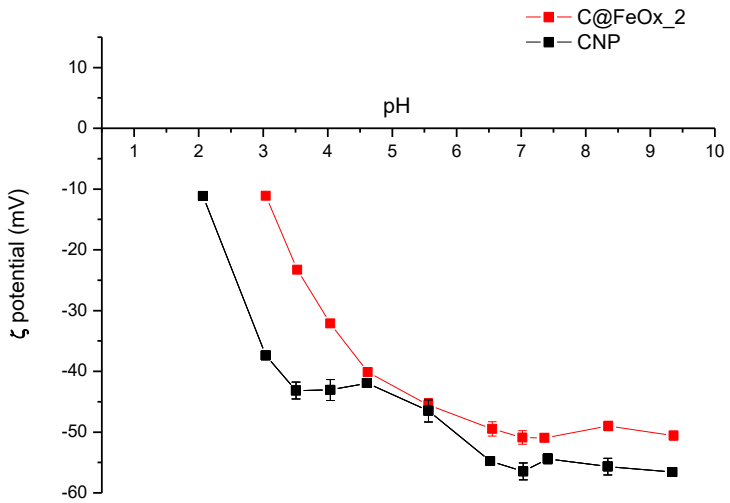

Figure 6.7. Zeta potential versus pH curves for C@FeOx_2 in comparison with CNP suspended in water.

6.3.3 Degradability of C@FeOx_2

Nanomaterials have a wide potential for diagnostic and therapeutic applications in medicine. However, besides efficacy, their safety profile has to be fully characterized for the translation into clinics. In fact, materials which are non-biodegradable can accumulate in tissues and cause noxious side-effects.[20]

In addition, several oxidants were found able to degrade carbon nanomaterials at different extent.[21], [22], [23] Here we investigate the degradability of C@FeOX using the endogenous oxidants, NaClO and hydrogen peroxide, as no information on their biodegradability are available so far. Visual observation and UV-Vis spectroscopy were used. As shown in figure 6.8.

C@FeOx_2 are efficiently degraded by hypochlorite, similarly to CNP. Moreover, oppositely to CNP (as mentioned in chapter 2), in this case the degradation was observed also with hydrogen peroxide, albeit at the higher concentration.

Note that the absorbance was still present at the end of the treatment due to the presence of the iron oxide core that resist to oxidants. This is visible in Figure

6.9, where the color of the suspension turned from black to red and sedimentation was observed, indicating that degradation of carbon shell occurred and iron oxide core was exposed to the surface. These findings suggest that C@FeOx_2 might be degraded by myeloperoxidase [29] the enzyme expressed mainly in neutrophils and able to generate the strong oxidant hypochlorous acid and in macrophages by hydrogen peroxide in vivo.

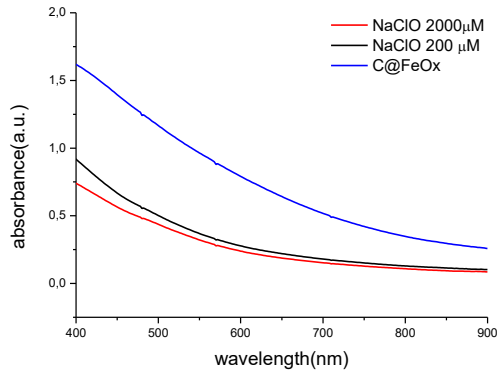

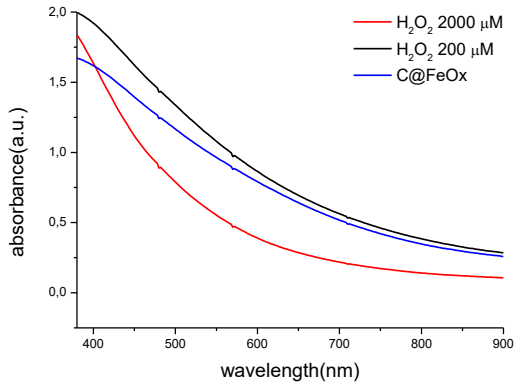

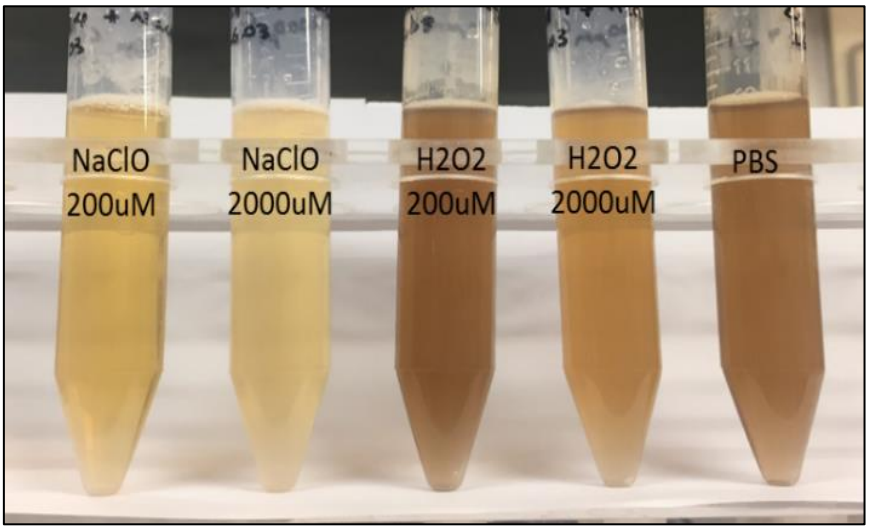

Figure 6.8. The comparison of UV–Vis spectra measurements performed for C@FeOx_2 in 200μM & 2000μM of $NaClO/H_2O_2$. Images of the suspensions at day 14.

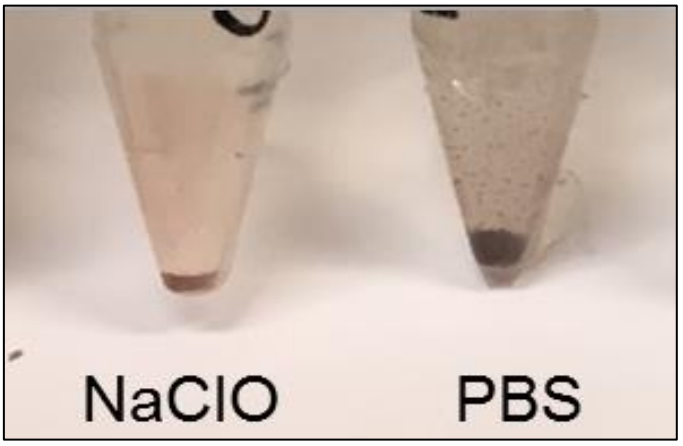

Figure 6.9. Optical changes of the suspension due to degradation: pelleted nanohybrides appear in red color due to the degradation of carbon shell (black) and exposure of FeOx (red).

6.3.4 Biocompatibility toward lung epithelial cells

Nanohybrides were finally tested for biocompatibility at CBNI, Dublin, by Silvia Vercellino and Mayra Cantoral, as part of their master thesis research activity financed by the Erasmus+ program. In vitro tests demonstrate that both samples are internalized by tumor lung epithelial cells (A549) without inducing any acute toxicity the highest concentration of 200 μg/ml. Confocal analysis confirm the integrity of cell and nucleus membrane following exposure to nanohybrids. By high content analysis, they assess that nanohybrids are internalized in lysosome and accumulate in this compartment, without giving rise to cytotoxicity and decrease in cell viability.

6.4 Conclusion

Magnetic nanohybrids with the desired dimensions were synthesized. We found that C@FeOx_2 were degraded by both hypoclorous acid and hydrogen peroxide suggesting a possible biodegradation of the material in vivo. On the other hand, the carbon shell appears to protect cells that do not express myeloperoxidase by the toxic effect of iron ions. In addition, the presence of the carbon coating improves the stability and provide interesting properties such as antioxidant capability. Due to the biocompatibility toward lung tumor cells, C@FeOX_2 could be a promising multifunctional therapeutic agent owing to the combination of carbon shell and iron oxide properties.

6.5 References

[1] Berry, C. C.; Curtis, A. S. G., Functionalisation of magnetic nanoparticles for applications in biomedicine. Journal of physics D: Applied physics 2003, 36 (13), R198

[2] Lee, N.; Yoo, D.; Ling, D.; Cho, M. H.; Hyeon, T.; Cheon, J., Iron Oxide Based Nanoparticles for Multimodal Imaging and Magnetoresponsive Therapy. Chemical Reviews 2015, 115 (19), 10637-10689.

[3] Laurent, S.; Dutz, S.; Häfeli, U. O.; Mahmoudi, M., Magnetic fluid hyperthermia: focus on superparamagnetic iron oxide nanoparticles. Advances in colloid and interface science 2011, 166 (1), 8-23.

[4] Alcantara D.; Lopez S.; García-Martin ML.; Pozo D.; Iron oxide nanoparticles as magnetic relaxation switching (MRSw) sensors: Current applications in nanomedicine. Nanomedicine. **2016**, 12(5), 1253-62.

[5] Ma, Z.; Liu, H., Synthesis and surface modification of magnetic particles for application in biotechnology and biomedicine. China Particuology 2007, 5 (1), 1-10.

[6] Tural, B.; Özkan, N.; Volkan, M., Preparation and characterization of polymer coated superparamagnetic magnetite nanoparticle agglomerates. Journal of Physics and Chemistry of Solids 2009, 70 (5), 860-866.

[7] Fang, C.; Bhattarai, N.; Sun, C.; Zhang, M., Functionalized Nanoparticles with Long-Term Stability in Biological Media. Small 2009, 5 (14), 1637-1641.

[8] Sun, C.; Lee, J. S. H.; Zhang, M., Magnetic nanoparticles in MR imaging and drug delivery. Advanced Drug Delivery Reviews 2008, 60 (11), 1252-1265.

[9] Karimi, Z.; Karimi, L.; Shokrollahi, H., Nano-magnetic particles used in biomedicine: core and coating materials. Materials science & engineering. C, Materials for biological applications 2013, 33 (5), 2465-75.

[10] Volatron J.; Carn F.; Kolosnjaj-Tabi J.; Javed Y.; Vuong Q.; Gossuin Y.; Ménager C.; Luciani N.; Charron G.; Hémadi M.; Alloyeau D.; Gazeau F.; Ferritin Protein Regulates the Degradation of Iron Oxide Nanoparticles. Small 2017,13(2)

[11] Lee N.; Yoo D.; Ling D.; Cho M.; Hyeon T.; Cheon J.; Iron Oxide Based Nanoparticles for Multimodal Imaging and Magnetoresponsive Therapy. Chem Rev. 2015, 115(19), 10637-89

[12] Oh, J. K.; Park, J. M., Iron oxide-based superparamagnetic polymeric nanomaterials: Design, preparation, and biomedical application. Progress in Polymer Science 2011, 36 (1), 168-189

[13] Wang, H.; Shen, J.; Li, Y.; Wei, Z.; Cao, G.; Gai, Z.; Hong, K.; Banerjee, P.; Zhou, S., Magnetic iron oxide–fluorescent carbon dots integrated nanoparticles for dual-modal imaging, near-infrared light-responsive drug carrier and photothermal therapy. Biomater. Sci. 2014, 2 (6), 915-923.

[14] Wang, H.; Chen, Q.-W.; Yu, Y.-F.; Cheng, K.; Sun, Y.-B., Size- and Solvent-Dependent Magnetically Responsive Optical Diffraction of Carbon-Encapsulated Superparamagnetic Colloidal Photonic Crystals. The Journal of Physical Chemistry C 2011, 115 (23), 11427-11434.

[15] Wang, H.; Sun, Y.; Yi, J.; Fu, J.; Di, J.; del Carmen Alonso, A.; Zhou, S., Fluorescent porous carbon nanocapsules for two-photon imaging, NIR/pH dual-responsive drug carrier, and photothermal therapy. Biomaterials 2015, 53, 117-26.

[16] Wang, H.; Shen, J.; Li, Y.; Wei, Z.; Cao, G.; Gai, Z.; Hong, K.; Banerjee, P.; Zhou, S., Magnetic iron oxide–fluorescent carbon dots integrated

nanoparticles for dual-modal imaging, near-infrared light-responsive drug carrier and photothermal therapy. Biomater. Sci. 2014, 2 (6), 915-923.Wang et al., Dalton Trans., 2010, 39, 9565–9569.

[17] E. Carella, M. Ghiazza, M. Alfè, E. Gazzano, D. Ghigo, V. Gargiulo, A. Ciajolo, B. Fubini, I. Fenoglio, Graphenic Nanoparticles from Combustion Sources Scavenge Hydroxyl Radicals Depending Upon Their Structure, BioNanoSci., 2013, 3, 112.

[18] L. L. Dugan, D. M. Turetsky, C. Du, D. Lobner, M. Wheeler,C. R. Almli, C. K. F. Shen, T. Luh, D. W. Choi and T. Lin, Carboxyfullerenes as neuroprotective agents, Proc. Natl. Acad. Sci. U S A, 1997, 94, 9434.

[19] S. Tsuruoka, H. Matsumoto, K. Koyama, E. Akiba, T. Yanagisawa, F. R. Cassee, N. Saito, Y. Usui, S. Kobayashi, D. W. Porter, V. Castranova, M. Endo, Radical scavenging reaction kinetics with multiwalled carbon nanotubes, Carbon, 2015, 83, 232.

[20] Medina C., Santos-Martinez MJ., Radomski A., Corrigan OI., Radomski MW. Nanoparticles: pharmacological and toxicological significance. Br J Pharmacol, 2007, 150, 552-8

[21] Bai et al., 2014

[22] V. E. Kagan, A. A. Kapralov, C. M. St. Croix, S. C. Watkins, E. R. Kisin, G. P. Kotchey, K. Balasubramanian, I. I. Vlasova, J. Yu, K. Kim, W. Seo, R. K. Mallampalli, A. Star, A. A. Shvedova, Lung Macrophages “Digest” Carbon Nanotubes Using a Superoxide/Peroxynitrite Oxidative Pathway, ACS Nano 8 (2014) 5610-5621

[23] L. Newman, N. Lozano, M. Zhang, S. Iijima, M. Yudasaka, C. Bussy & K. Kostarelos, Hypochlorite degrades 2D graphene oxide sheets faster than 1D

oxidised carbon nanotubes and nanohorns, npj 2D Materials and Applications 1 (2017) 39

Acknowledgments

This thesis would not have been possible without the effort of so many people, to whom I would like to express my sincere gratitude.

First and foremost, I feel deeply grateful to my supervisor, Prof. Ivana Fenoglio, for her exceptional scientific guidance throughout these years and for being such a great and inspiring group leader; for her endless support, infinite patience and her unique human qualities.

To Prof. Chiara Riganti and Dr. Elena Gazzano and their group, Department of Oncology, University of Turin, for their outstanding help and for the priceless contribution in the in vitro cellular studies included in chapters 1 and 2.

I would like to thank the other research groups in Turin with whom I have had the opportunity and privilege of working with. To Prof. Guido Perrone, Dr. Riccardo Gassino and Jennifer Pogliano, Department of Electronics and Telecommunications, Politecnico of Turin, for their indispensable contribution in the investigation of the photoactivity of CNP. To Dr. Andrea Mario Rossi, Dr. Andrea Mario Giovannozzi, Giulia Barzan and Dr. Luca Croin, INRIM, for their scientific inputs during these years and their contribution with Raman spectroscopic investigations, SEM imaging and in vitro cellular tests described in chapters 1, 2 and 5. To Dr. Elena Ghibaudi, Prof. Ornella Abollino e Sandro Buoso, Department of Chemistry, for their help in the characterization of CNP as nanocarrier, reported in chapters 4 and 5.

To Prof. Marco Monopoli, Royal College of Surgeons in Ireland and to Prof. Bengt Fadeel, Karolinska Institutet, Sweden, for giving me the opportunity to perform research in their laboratories, for the hospitality, professionalism, the continuous motivation and the scientific contribution included in chapters 2, 3 and 4 of this thesis. I am very grateful to Dr. Sandeep Keshavan, Karolinska Institute,

for his great help and valuable guidance and for his scientific contribution included in the chapter 2.

To Dr. Jessica Ponti, Joint Research Centre, Ispra, for her valuable contribution with imaging experiments included in chapters 1 and 2.

To Prof. Kenneth Dawson and his research group, University College Dublin, for their contribution in the characterization of the core-shell nanohybrids, included in chapter 6.

To Dr. Roel Schins and Dr. Catrin Albrecht for their contribution in the *in vitro* toxicological investigation regarding metal loaded CNP, included in chapter 4.

I acknowledge the financial support for my research studies of the Ministero dell' Istruzione dell' Università e della Ricerca (MIUR), Erasmus+ Traineeship Programme, the European Union's Horizon 2020 research and innovation programme under grant agreement No 760928 and Joint Research Centre, JRC, Ispra, project title CeTECaN.

Special thanks go to the members of the TBM group and to all the labmates during these years at the Department of Chemistry. In particular, to Dr. Arianna Maria Marucco e Dr. Riccardo Leinardi: for their help, encouragements, support, discussions and their never give up attitude.

I would also like to include in these thanks all the master students that contributed to this research project: Davide Isaia, Gabriele Castrignanò, Giacomo Gariglio, Giorgia Bernardini, Giulia Antonello, Ion Tacu, Ludovica Soddu, Mayra Cantoral, Sanaz Keshtkari, Silvia Vercellino.

Finally, I cannot thank my closest friends and my dear family enough for their infinite love, support and encouragement throughout this journey.